2018-01-01

An Adaptive Creep Modeling Approach Using Metamodeling

Mohammad Shafinul Haque
University of Texas at El Paso, toshafin@gmail.com

AN ADAPTIVE CREEP MODELING APPROACH USING METAMODELING

MOHAMMAD SHAFINUL HAQUE

Doctoral Program in Mechanical Engineering

APPROVED:

Calvin M Stewart, Ph.D., Chair

Jack Chessa, Ph.D., Co-Chair

Cesar Carrasco, Ph.D.

Soheil Nazarian, Ph.D.

Charles Ambler, Ph.D.
Dean of the Graduate School

Dedication

Dedicated to my parents and my wife.

Mohammad Israrul Haque and ***Shahnaz Haque***

Zakia Al Kadri

"God bless our family"

AN ADAPTIVE CREEP MODEING APPROACH USING METAMODELING

by

MOHAMMAD SHAFINUL HAQUE, MS in Mechanical Engineering

DISSERTATION

Presented to the Faculty of the Graduate School of

The University of Texas at El Paso

in Partial Fulfillment

of the Requirements

for the Degree of

DOCTOR OF PHILOSOPHY

Department of Mechanical Engineering

THE UNIVERSITY OF TEXAS AT EL PASO

May 2018

Acknowledgements

This research was performed with the support of the U.S. Department of Energy Office of Fossil Energy at National Energy Technology Laboratory (NETL) under the HBCU/MI program with grant number of DE-FE0027581.

I would like to thank my advisor Dr. Calvin M Stewart for his teaching, training, guidance, thoughtful suggestions, and support throughout my graduate education. My thanks go to the member of my dissertation committee for their support, suggestions and teaching, who are: Dr. Jack Chessa, Dr. Cesar Carrasco, and Dr. Soheil Nazarian.

I would like to thank all my colleagues, all the people who have provided technical, emotional, or spiritual support during my studies including Graduate School, ME Front-Desk and OIP (Office of International Program).

Abstract

Recent drives to increase the efficiency of existing fossil energy power plants and the development of Advanced Ultrasupercritical power plants, have led to designs with steam pressures above 4000 psi and temperatures exceeding 1400°F. The complexity of the applied thermo-mechano chemical boundary conditions makes it critically important to consider creep and creep related failures. One primary concern to FE practitioners is a determination of which constitutive models are the "best", capable of reproducing the mechanisms expected in an intended design accurately; as well as what experimental datasets are proper or "best" to use for fitting the constitutive parameters needed for the model(s) of interest. In this dissertation the work completed towards these questions are presented.

Various forms of creep data are collected and statistical analysis are performed. It is observed that data pre-processing and inclusion of disparate datasets into the calibration process can significantly improve the prediction accuracy. Realistic extrapolation and interpolation is possible for wide range of service condition leading to the development of Creep Design Maps. Towards the development of an approach for determining the "best" model; it is hypothesized that, "a general model (metamodel) derived by combining and exploiting creep models where the submodels (existing and new models that are exploited to develop the metamodel) are special case can facilitate instantaneous and efficient evaluation of the submodels leading to the selection of "best" model". Successful metamodeling examples for stress-rupture, creep deformation, and CDM based models are provided. A guideline for metamodeling and multiaxiality function by combing the international standards (e. g. ASME PVP III, ASTM, ECCC, RCC-MR, R5) is presented.

Table of Contents

List of Tables

List of Figures

Chapter 1: Introduction

1.1 Motivation

Drives to extend the service life of existing fossil energy power plants will lead to structural components with lives beyond 10^6 hours. In addition, the ongoing development of Advanced-Ultrasupercritical (A-USC) power plants has created a materials challenge where new material is needed to withstand operating pressures above 4000 psi and temperatures exceeding 1400°F. These conditions make it critically important to consider creep deformation and damage in the design process of FE power plant components and systems. Creep is gradual deformation, distortion or elongation of the components, that can lead to failure. It is stated that, an increment of as small as 15°C operating temperature, cuts the components creep life by 50% [1].

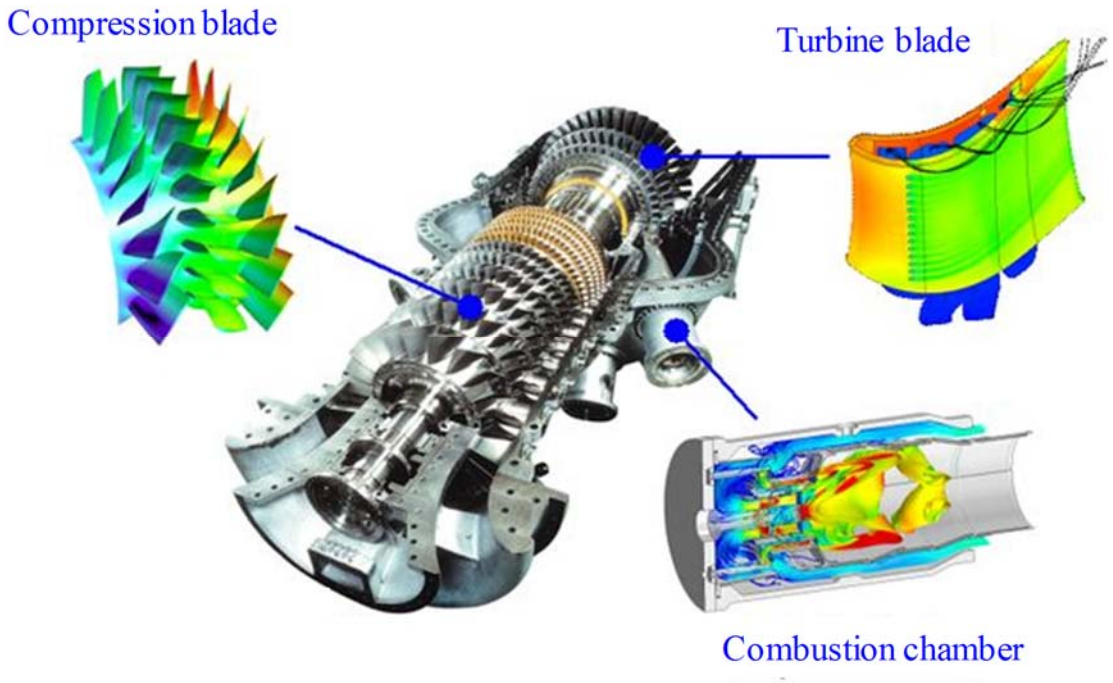

Figure 1.1 – Kawasaki Heavy Industrial Gas Turbine (L20A)

Dundas indicated a statistic saying that 62% of the total damage cost of gas turbines are consists of cycle cooling, fatigue, creep and surge related failure [2]. 19% of the heavy-duty gas turbine damage costs are due to creep damage. Though rotating parts are more susceptible to creep damage, real life statistics shows that stationary components are also susceptible to creep damage. Bloch stated that rotor and blades are consists 28% of primary cause of gas turbine failure [3]. Stationary components and nozzles consists 18% of the failure cause. Turbine components [Figure 1.1] are primarily made of superalloys. Iron based superalloys got replaced by nickel based and cobalt based superalloys. Iron based superalloy made components can be found in some old turbines or in cold section components. These are called "super" because they contain so many alloying elements and due to their good mechanical properties at high as well as low temperature. Most of the hot components are made of nickel based super alloy because of its comparatively greater strength.

Figure 1.2 – Creep failure of industrial gas turbine. The residual mold material (appears as pink) causes overheating leading to creep [6].

Figure 1.3 – Creep damage on a gas turbine. (a) rotor (b) stator, and (c) Turbine blade [7]

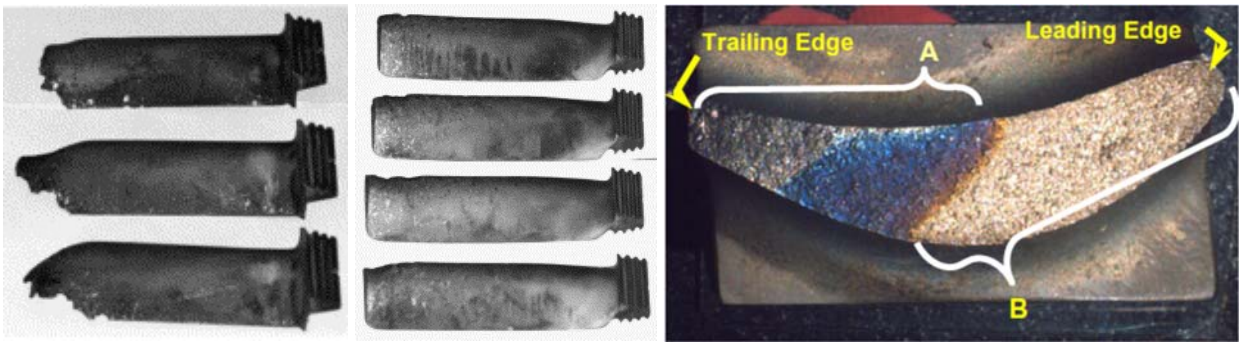

Figure 1.4 – Damaged turbine blade due to creep [8,9]

Cobalt based super alloys are used for vanes due to their good weldability and resistance to hot corrosion [3]. In spite of good mechanical properties of these super alloys, (with or without protective coating) they are still susceptible to creep damage as shown in Figure 1.2. During creep, material elongates due to tensile stress. This creep deformation may lead to tip rub as shown in Figure 1.3-3. On cooling blade, tip rub may block the cooling air flow, resulting over heating of the blades [1-3]. Excessive creep deformation may lead to contact of blade tip with the turbine body causing collateral damage [5].

Knowledge concerning the long-term creep behavior of existing and new materials is needed to make fail-safe design decisions; however, often only limited creep data is available. The average time-to-implementation of new creep resistant alloys is between 10 to 20 years [4]. This

development time is consumed by computational materials design, thermomechanical processing optimization, and the physical experiments needed to qualify the long-term creep resistance of a material [5]. Effective and economic maintenance requires accurate creep deformation, damage evolution and rupture life prediction information. Creep prediction models are used to determine the state of the turbine components and to schedule the inspection, maintenance and replacement time periods. Over the years, an immense number of models have been developed to predict the deformation, damage evolution, and rupture of structural alloys subjected to creep. Each model has been proved to be accurate for at least one material over a specific range of stress and temperature; however, no single model can perform accurately for the wide variety of engineering alloys available nor meet the analysts' expectations for every service conditions. In addition, another primary concern to FE practitioners is a determination of which constitutive models are the "best", capable of reproducing the mechanisms excepted in an intended design accurately; as well as what experimental datasets are proper or "best" to use for fitting the constitutive parameters needed for the model(s) of interest.

1.2 RESEARCH OBJECTIVES

The objectives of this research are to develop an adaptive creep modeling approach using metamodeling. A "metamodel" can be described as a combinational model, derived from rearranging, modifying, and/or expanding the functional relationships between different models. A metamodel can exhibit unique attributes that could potentially make them superior to the originals such that most suitable model can be determined for a given material. The major objective is subdivided into following four sub-tasks:

(1) Metamodeling for Time-Temperature-Parameter model

Eight time-temperature parameter models are collected and studied. An additional four new

models are derived by exploiting the similarities between the existing models. The twelve models are paired into twos; grouped together as “mirror models” by the mirror like similarities of their isostress lines. Thus, six groups of “mirror models” is formed that simplifies model characteristic analysis. These TTP models tend to follow the same general framework, rules, and constraints such that they can be mathematically exploited towards metamodeling. A metamodel incorporating the twelve models is proposed.

(2) Metamodeling for Creep deformation model

Three creep deformation model named Omega, Theta-projection, and Sine-Hyperbolic model are exploited to develop combinational models that exist between them. Metamodeling is applied to the problem of creep deformation, damage, and rupture. Model transformations between the Theta projection, MPC Omega, and Sin-hyperbolic constitutive models are derived to (a) facilitate the efficient conversion of one models’ material constants to the constants of the others and (b) enable the derivation of six combinational models.

(3) Disparate data problem and Design-maps

It is hypothesized that cross-calibrating a constitutive model to any and every form of available creep data (across test type, stress and temperature range) will lead to more reliable extrapolations. This is demonstrated by integrating minimum-creep-strain-rate, stress-rupture, and short-/intermediate-term creep deformation data into the calibration process of a constitutive model. In addition, the approach facilitates the development of creep design maps that can be used for determining design boundary condition, material selection, and to compare the interpolation and extrapolation ability of the models.

(4) Multiaxiality representative function

seven representative stress and eight representative strain functions are evaluated. The skeletal point approach to calibrating these functions is discussed. The incompressibility of the representative stress functions is analyzed. Rupture surfaces of the representative stress functions under biaxial stress conditions are generated to compare the advantages and limitations of the functions. Several functions are found to exhibit divide by zero errors and/or imaginary number errors leading to unstable and discontinuous rupture surfaces. It is observed that the selection of an appropriate representative function is dependent on loading condition, geometry, and material properties. The Hayhurst and Huddleston representative stress functions are found as the most suitable functions to predict multiaxial rupture for a general multiaxial stress states. Finally, a guideline to the selection of the appropriate representative stress function and the associated incompressibility condition is presented.

1.3 ORGANIZATION

This work is organized is eight chapters. Chapter 2 introduces the various types of creep models (minimum-creep-strain-rate, creep-rupture, creep deformation and damage) used in this study and literature review. Chapter 3 introduce the materials and various form of data used in this study. In Chapter 4, adaptive creep modeling for classic creep-rupture models (time-temperature parameter models, TTP's) is presented. A "mirror pair" metamodel is introduced that incorporates twelve time-temperature parameter submodels (eight existing and four new) into a single equation. As a result, the metamodel can be used to efficiently evaluate the twelve submodels. In Chapter 5, adaptive creep modeling for creep deformation is presented. Two most popular creep deformation model (Omega, and Theta projection) and a Sine-hyperbolic model are used to develop six additional inter-functional models that facilitates instant transformation of martial constants of one model into another, and determination of suitable model for a subject material. Chapter 7, address

the disparate data problem and the development of various design maps. Finally, Chapter 8, contain the concluding remarks and future works. Experimental data, MATALB code are presented in Appendix section.

Chapter 2: Background

2.1 Introduction

Towards the development of adaptive creep modeling, a literature review of creep and popular creep models is conducted that will provide the basic idea of a typical model. Background study provides the information about current stage of this field. Problems and limitations can be understanding from background study that makes the way for possible improvement. This section includes the early stage creep rupture life prediction models.

2.2 Constitutive Models for Creep

The constitutive models for creep is the mathematical description of how materials respond to various service condition (stress, and temperature) under creep. There are various forms of constitutive model available. The most commonly used forms are the minimum-creep-strain-rate, creep deformation, creep-rupture, and creep damage models. The creep constitutive models for these forms used in this study are described here.

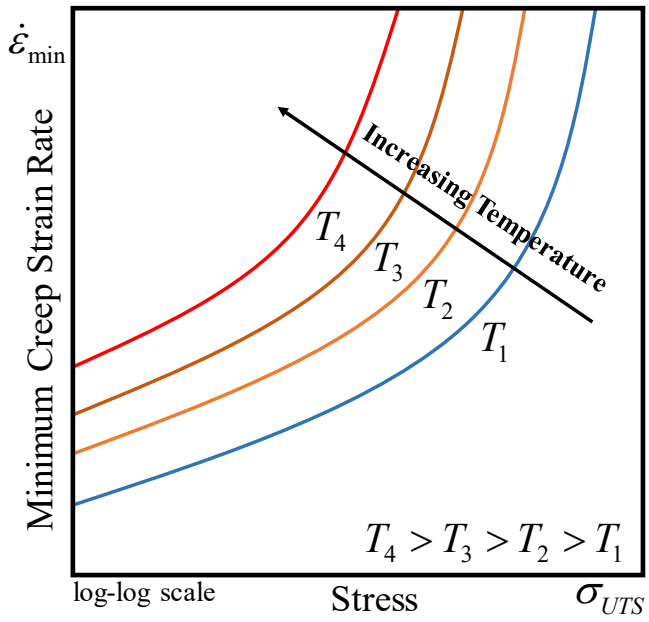

Figure 2.1 – Ideal minimum-creep-stain-rate curve. Increasing temperature leads to a higher minimum-creep-strain-rate at a given stress vice-versa.

2.2.1 Minimum-Creep-Strain-Rate

The minimum-creep-strain-rate is also known as steady state creep or secondary creep constitutive models. In this study it will be denoted as minimum-creep-strain-rate model. The most commonly used minimum-creep-strain-rate model is the Norton Power law (year 1929) based on the Arrhenius rate equation as follows [10]

$$\dot{\varepsilon}_{\min} = B'\sigma^n \exp[-Q_c / RT] \tag{1}$$

where, $\dot{\varepsilon}_{\min}$ is the minimum-creep-strain-rate, B is a material constant, σ is the applied stress, n is the power law exponent, Q_c is the activation energy, R is the universal gas constant, and T is the applied temperature. For a constant temperature, T the Arrhenius rate [Eq. (1)] is reduced to

$$\begin{aligned} &\dot{\varepsilon}_{\min} = A\sigma^n; \\ &A = B'\exp[-Q_c / RT] \end{aligned} \tag{2}$$

Another minimum-creep-strain-ate model used in this study is the McVetty law (year 1943)

$$\dot{\varepsilon}_{\min} = B\,\mathrm{Sinh}(\sigma / \sigma_S) \tag{3}$$

The constants B (1/s) and σ_s (MPa) are the creep coefficient and secondary creep mechanism-transition stress respectively. A list of additional four minimum-creep-strain-rate model are listed in Table 1.

Table 1 – Minimum-creep-strain-rate equations

Source	Minimum-creep-strain-rate model
Soderberg, 1936	$\dot{\varepsilon}_{\min} = A\{\exp(\sigma / \sigma_0) - 1\}$
Dorn, 1955	$\dot{\varepsilon}_{\min} = A\exp(\sigma / \sigma_0)$
Johnson, Henderson, and Khan, 1963	$\dot{\varepsilon} = A_1(\sigma / \sigma_0)^{n_1} + A_2(\sigma / \sigma_0)^{n_2}$

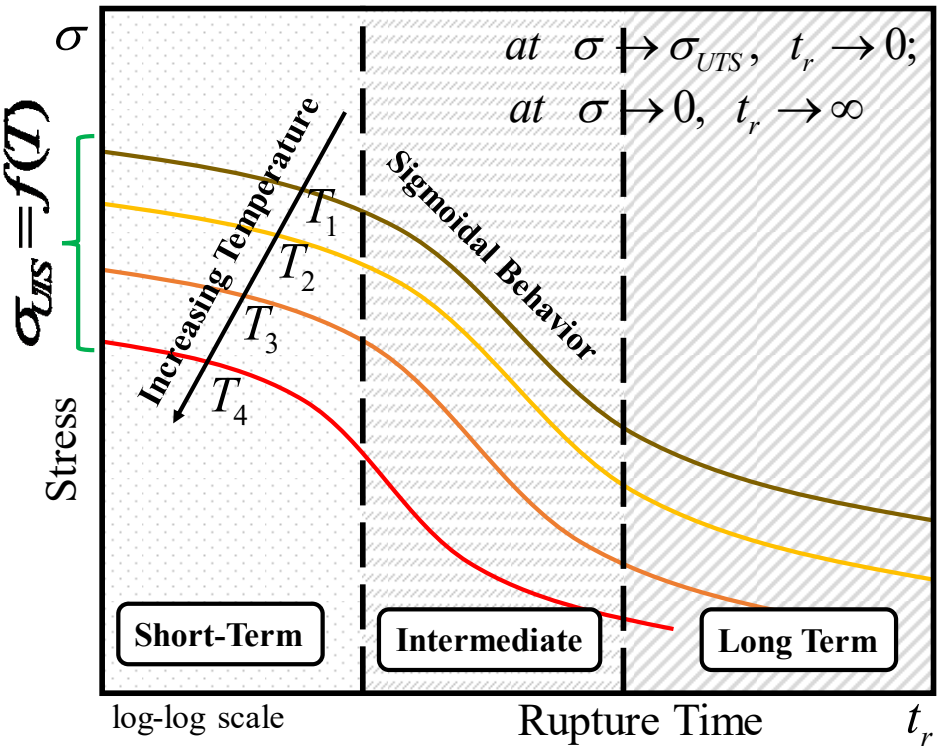

Figure 2.2 – Ideal creep-rupture curve. The creep life is zero at UTS and infinite at very low stress level, creating an expected sigmoidal bend in the creep-rupture curve.

2.1.3 Creep Rupture

Life prediction models for creep can be mathematically described as time-temperature-stress functions; calibrated for a given material. In 1952 Larson and Miller first introduced a time-temperature parameter model to predict creep life by expanding the work of Hollomon and Jaffe [15, 16]. These investigators observed the effect of time during tempering treatment on metal hardness and proposed a mathematical relation to obtain a given hardness to treatment time and temperature. Larson and Miller replace the treatment time with creep life, and hardness with stress to relate with temperature. It is assumed that the isostress line on a plot of $\log t_r$ versus 1/T converge to a point on $\log t_r$ axis. Simplicity of Larson-Miller (LM) model made it a favorite choice among creep-rupture analysts till date. In 1953 Manson and Haferd conducted a detailed study on LM model and reported limitations of LM model while extrapolating using short term creep data [17]. It is proposed that the isostress line converge to a point ($\log t_a$, Ta) on a plot of $\log t_r$ versus T rather than $\log(t_r)$ axis. In the following year in 1954, while studying pure material rather than engineering alloys, Orr-Sherby-Dorn (OSD) proposed that the isostress lines does not converge to a point but parallel on a plot of $\log t_r$ versus 1/T and introduced a new parameter. Later many more parameter models were introduced by conducting tests on different materials at various creep conditions, and exercising various interpolation/extrapolation analysis. Most of these models are a modification, expansion and/or collective representation of the earlier LM, MH, and OSD parameter models. Some common parameter models are Manson-Succop (MS), Manson-Brown (MB), Goldhoff-Sherby (GS), and Mendelson-Robert-Manson etc.

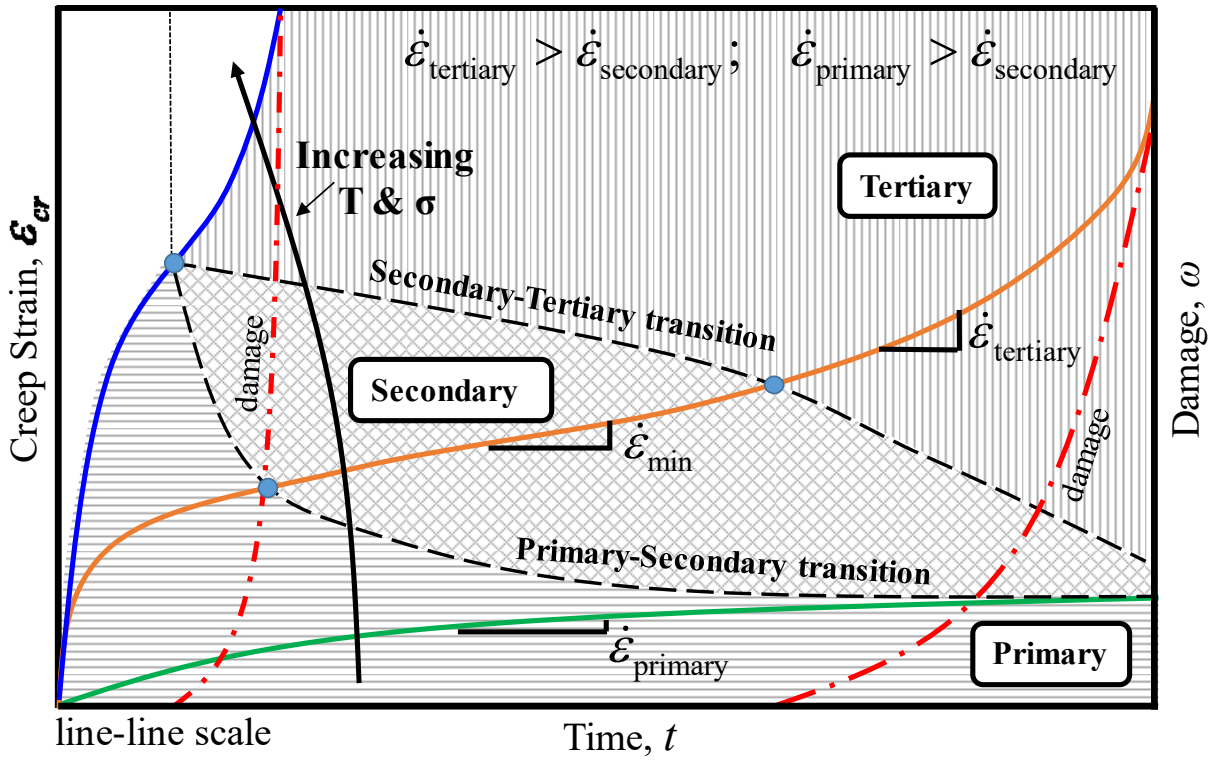

Figure 2.3 – Creep deformation and damage evolution: The green, yellow, and red zones represent the primary, secondary, and tertiary stages respectively where the dash lines represent the transition between stages. The red dash-dot lines represent the irreversible meso-scale damage that accumulates at the onset of tertiary creep.

2.2.2 Creep Deformation

Creep deformation can be separated in three successive stages: primary, secondary, and tertiary as depicted in Figure 2.3. The primary creep regime dominants at low temperature and low stress. In high-temperature alloys, negligible primary creep strain will accumulate and it is often not observed in experiments. The secondary creep regime dominants at low-to-intermediate stress and temperature. This regime is the most stable where a balance of strain-hardening and recovery mechanics make the prediction of creep deformation simple. At intermediate-to-high temperature and stress, the tertiary creep regime dominants. This regime is characterized by the non-linear

accumulation of creep-damage that contributes to gross creep deformation and rupture [11]. In extreme environments, such as Advanced Super-Critical Carbon Dioxide power cycles, the secondary and tertiary creep regime will be dominant.

MPC Omega Model

The MPC Omega model was first proposed by Prager in 1995 [12]. It was developed by the Materials Properties Council. In the Omega model, the life fraction used (damage) is defined as

$$\omega = \frac{t}{t_r} = \frac{\dot{\varepsilon}\Omega t}{1 + \dot{\varepsilon}\Omega t} \tag{4}$$

where, t is the current time, t_r is the rupture life, and $\dot{\varepsilon}$ is the current creep strain rate, and Ω is defined as the material creep damage susceptibility constant. When the current time approaches rupture $(t \to t_r) \,\&\, (t / t_r \to 1)$, equation [Eq. (4)] collapses. Thus the life fraction evolves from zero to near unity $(0 \le t / t_r < 1)$. Prager [12] proposed that creep strain has the following relation

$$1 - \dot{\varepsilon}_0 \Omega t = 1 / e^{\varepsilon\Omega} \tag{5}$$

where ε is the creep strain and $\dot{\varepsilon}_0$ is the initial creep strain rate constant. Taking the natural logarithm on both sides and rearranging gives

$$\varepsilon = \frac{-1}{\Omega} \ln(1 - \dot{\varepsilon}_0 \Omega \, t) \tag{6}$$

Equation [Eq. (6)] can be further simplified by taking the derivative with respect to time and replacing $1 - \dot{\varepsilon}_0 \Omega t$ from [Eq. (5)] as follows

$$\dot{\varepsilon} = \dot{\varepsilon}_0 e^{\varepsilon\Omega} \tag{7}$$

Thus the Omega model assumes that the creep strain rate is proportional to the exponent of the accumulated creep strain and does not model the primary creep stage. The Omega model is easy

to apply as it only requires two constants $\dot{\varepsilon}_0$ and Ω. Taking the natural logarithm on both sides of equation [Eq. (7)] gives

$$\ln \dot{\varepsilon} = \ln \dot{\varepsilon}_0 + \varepsilon\Omega \tag{8}$$

The constant Ω can be obtained from experimental data using [Eq. (8)]. The slope of the $\ln \dot{\varepsilon}$ vs ε plot is the value of Ω. A large value of Ω (>30) indicates that most of the life is spent at very low creep strain followed by a rapid increase in creep strain rate before failure. A low value of Ω indicates that most of life is spent in the tertiary creep regime. The $\ln(\dot{\varepsilon})$ vs ε can also determine if the plot does not produce a straight line, then Omega should not be used [13].

Theta Projection Model

The Theta projection model was proposed by Evans and Wilshire to predict multistage creep deformation (primary-secondary-tertiary) [14]. The Theta creep strain, ε is written as follows

$$\varepsilon = \theta_1[1 - \exp(-\theta_2 t)] + \theta_3[\exp(\theta_4 t) - 1] \tag{9}$$

where the material constants θ_1 and θ_2 control the scale and the curvature of the primary creep strain respectively and the material constants θ_3 and θ_4 control the scale and the curvature of the tertiary creep strain respectively. The material constants $\theta_1, \theta_2, \theta_3$ and θ_4 are functions of both temperature and pressure $\theta_i = f_i(\sigma, T)$. The functions are determined by calculating the θ_i for each creep test in a database of creep tests and performing regression analysis to determine the optimal function. The primary creep strain term can be neglected if no/negligible primary creep strain is observed. The tertiary creep strain rate can be obtained by taking derivatives with respect to time, *t* of the second term giving

$$\dot{\varepsilon}_t = \theta_3\theta_4 \exp(\theta_4 t) \tag{10}$$

Taking the natural logarithm of both sides of the tertiary creep strain rate [Eq. (10)] gives

$$\ln(\dot{\varepsilon}_t) = \ln(\theta_3\theta_4) + \theta_4 t \tag{11}$$

When [Eq. (11)] is plotted as $\ln(\dot{\varepsilon}_t)$ vs *t,* the constant θ_4 is the slope and $\ln(\theta_3\theta_4)$ is the intercept. A large value of θ_4 indicates that the creep strain rate accelerates near the end of life. A low value of θ_4 indicates that the creep strain rate remains relatively constant throughout life. Assuming negligible primary creep strain, the time, *t* at a value of strain, ε can be obtained by rearranging equation [Eq. (9)]

$$t = \frac{1}{\theta_4}\ln(\frac{\varepsilon}{\theta_3} + 1) \tag{12}$$

When $\varepsilon = \varepsilon_r$, the Theta life prediction and life fraction/damage can be obtained

$$t_r = \frac{1}{\theta_4}\ln(\frac{\varepsilon_r}{\theta_3} + 1) \tag{13}$$

$$\omega = \frac{t}{t_r} = \frac{\ln(\frac{\varepsilon}{\theta_3} + 1)}{\ln(\frac{\varepsilon_r}{\theta_3} + 1)} \tag{14}$$

where t_r is rupture life, ω is damage, and ε_r is the creep ductility. The damage evolves from zero to unity $(0 \le \omega < 1)$. Hyde and colleagues stated that for a given temperature and stress, the creep ductility exhibits more uncertainty than rupture life [16]. As a result, uncertainty analysis of the creep ductility should be performed prior to application of the Theta life prediction [Eq. (13)] [87].

2.2.4 Creep Damage

Creep-damage is the irreversible accumulation of defects that contribute to rupture as depicted in Figure 2.3. Cauvin and Testa characterized damage in three scales micro-, meso- and macro-scales. Atomic voids and dislocations appear on the micro-scale while visually or near-visually observable damage is on the macro-scale [18]. The mesoscale consists of a representative volume element that averages the effects of micro-scale cracks, voids, and other distributed deteriorations. It is the mesoscale that should be accounted for when using continuum damage mechanics (CDM). Marigo stated that damage takes place when atomic bonds break at the microstructural level and damage represents surface discontinuities in the form of micro-cracks and volume discontinuities in the form of cavities [19]. Lindborg explained that (a) localized stress concentrations mount up due to micro-cracks; (b) rapid plastic and/or viscoplastic flow can occur at the crack tips; and (c) sharp cracks are more critical for damage than round voids [20]. Ibijola classified damage as brittle when the crack initiates at the mesoscale without plastic strain and damage is ductile when damage occurs simultaneously with plastic deformation [21]. Lemaitre added that cracks and voids inside materials are oriented randomly [22]. It is common to consider these orientations as an intrinsic variable of damage [23,24]. Ibijola proposed a model assuming that cracks and voids are equally distributed in all directions inside the material and do not depend on orientation [21]. Later it was proposed that there are two complementary approaches to damage, one that focuses on actual damage manifestations at mesoscale (the micromechanics approach) and the one that assumes homogeneous relation with damage (the phenomenological approach) which has been coined as "continuum damage mechanics" [18,25]. Hill and Hashin have done significant work on the micromechanics approach and solved the boundary value problem of a representative volume element (RVE) with distributed microstructural features [26,27]. Kachanov originated the idea of

a scalar phenomenological damage quantity for damage modeling based on CDM. Rabotnov derived damage as the "area of cavities" in the cross-sectional area of a uniaxially stressed specimen. Rabotnov developed a damage evolution equation that when coupled to a power-law creep strain rate is known as the Kachanov-Rabotnov (KR) creep-damage model [28,29]. The KR model was extended by Penny to extrapolate long-term creep-rupture behavior using short-term creep-rupture data [30-32]. Le May and Furtado studied the relationship between the KR damage equation and physical void formation [33]. Analytical tools have been developed to rapidly determine the material constants for the KR model given creep data [11].

Overall, the Kachanov-Rabotnov (KR) model has been found to accurately predict creep deformation; however, there are deficiencies in the functional form of the equations that contribute to poor minimum creep strain rate, damage evolution, and rupture predictions. The KR approach is a local CDM approach where rupture is reached when the damage variable within a representative volume element becomes unity. This is consistent with the idea that at rupture the "area of cavities" is equal to the cross-sectional area of a specimen. When the KR model is applied, it is reported that the analytical damage at rupture is well below unity, a result that is inconsistent with CDM [31,34]. Several investigators have observed the stress sensitivity and mesh dependency when implementing the KR model [35-37]. In finite element (FE) simulations of notched geometry, damage increases the stress concentration faster than the plasticity driven stress-relaxation. The damage rate becomes near infinite contributing to mesh dependence and numerical instability. Brittle-type, localized damage develops at the notch tip. Upon mesh refinement, FE simulations do not converge to a unique solution [38-40]. Stewart hypothesized that these issues and others could be overcome by introduce a set of coupled creep-damage equations that incorporate the Sine-hyperbolic (Sinh) function [41]. Stewart developed a multistage Sinh creep-

damage model that can model primary, secondary, and tertiary creep. The Sinh model mitigates stress sensitivity and the damage rate remains finite even on the verge of rupture [38, 39]. When the Sinh model is applied, rupture only occurs when damage equals unity.

Continuum Damage Mechanics

The initiation and growth of microstructural defects lead to gradual loss of material strength. The main purpose of Continuum Damage Mechanics is to model and incorporate this process in the constitutive equations for a given material. Continuum Damage Mechanics (CDM) based damage rate equations can provide accumulated damage, residual life, and rupture prediction given the applied stress and temperature. It is assumed that damage happens in a continua (a homogeneous representative volume) thereby the expression continuum damage mechanics is coined.

Generally, creep-damage can be classified in two forms: trans-granular damage and inter-granular damage. Trans-granular damage arises when dislocations inside the crystal grains form under high stress and low temperature. Inter-granular damage arises when micro-cracking and cavitation takes place at grain boundaries and triple points under high temperature and low stress [42].

The growth and accumulation of cavities under creep conditions lead to a reduction in the effective cross-section and thus an increase in the effective stress. For the calculation of damage, three type of stress can be considered [40]. The first is the true stress which accounts for the geometric reduction in cross-section due to macroscopic deformation

$$\sigma_T = \frac{F}{A_i} = \sigma \cdot (1 + \varepsilon) \tag{15}$$

where σ_T is true stress, F is applied force, A_i is an initial cross-sectional area, σ is engineering stress and ε is engineering strain. The second is the net stress which is a type of true stress that accounts for geometric homogenization

$$\sigma_N = \sigma_T \cdot \left(\frac{A_i}{A_N} \right) = \frac{\sigma_T}{(1-\Omega)} \tag{16}$$

where A_i is the current cross-sectional area, A_N is the mean area of de-cohesion, and Ω is the fraction of area de-cohesion. The net stress is higher than the true stress. Finally, there is the effective stress which accounts for local stress concentration, the interaction between defects, and mechanical behavior homogenization. The effective stress can be defined as the stress required to attain macroscopic engineering strain ε in an undamaged volume element subject to the engineering stress σ [40,41].

$$\begin{aligned} \bar{\sigma} &= \sigma \cdot \frac{A}{\bar{A}} = \frac{\sigma}{(1-\omega)} \\ \omega &= 1 - \frac{\bar{E}}{E} \end{aligned} \tag{17}$$

where $\bar{A}$ is an effective (reduced) cross-setional area, ω is damage, and $\bar{E}$ and E are the effective and initial elastic modulus respectively. As damage accumulates to unity, the effective elastic modulus approaches zero.

Kachanov-Rabotnov Model

In 1967, Kachanov observed a varying creep ductility but did not identify the damage mechanism responsible for tertiary creep [28]. Kachanov assumed creep displacement rates are much faster within the uncavitated regions than cavity growth regions and cavitation does not affect the macroscopic creep deformation. Fracture occurs when cavities are linked up throughout whole

transverse grain boundaries. This initial model did not predict tertiary creep for constant stress conditions. Later, in 1969, Rabotnov assumed the creep displacement rates is slower at the uncavitated regions than those of cavity growth regions [29]. Thus, stress is loaded up to the uncavitated zones from fast growing cavitated zones. The redistributed stress increases the creep rate. Rabotnov coupled the damage with the creep rate through an stress increment associated with a load reduction in bearing area as the cavitations/damage develops. This coupled model leads to an accelerated/tertiary creep rate [44].

In the Kachanov-Rabotnov model, amplified stress due to a local reduction in cross-sectional area is the basis of the damage variable, ω. The reduction in cross-section area is due to the formation of microcracks, cavities, and voids. The effective stress [Eq. (17)] is applied. The Kachanov-Rabotnov coupled creep-damage constitutive equations are as follows

$$\dot{\varepsilon}_{cr} = \frac{d\varepsilon_{cr}}{dt} = A \cdot (\frac{\sigma}{1-\omega})^n \tag{18}$$

$$\dot{\omega} = \frac{d\omega}{dt} = \frac{M \cdot \sigma^{\psi}}{(1-\omega)^{\theta}} \tag{19}$$

where A and n are the Norton power law constants, σ is equivalent stress and M, ψ and θ are the tertiary creep-damage constants [28,29]. The ψ constant controls the magnitude of M and can be set arbitrarily to any number greater than or equal to unity. Rupture time and critical damage can be predicted by integration of the damage evolution [Eq. (19)] and assuming the initial time t_0 and initial damage ω_0 are equal to zero [11,40].

$$t = [1-(1-\omega)^{\theta+1}] \cdot [(\theta+1) \cdot M \cdot \sigma^{\psi}]^{-1} \tag{20}$$

$$\omega(t) = 1-[1-(\theta+1) \cdot \mathrm{M} \cdot \sigma^{\psi} \cdot t]^{\frac{1}{(\theta+1)}} \tag{21}$$

The tertiary creep constant M can be calculated by rearranging [Eq. (20)]

$$M = \frac{1-(1-\omega_r)^{\theta+1}}{(\theta+1)\cdot\sigma^{\psi}\cdot t_r} \tag{22}$$

At rupture time, assuming the critical damage $\omega_r = 1$ gives

$$M = \frac{1}{(\theta+1)\cdot\sigma^{x}\cdot t_r} \tag{23}$$

One of the major drawbacks of the KR model is the difficulty determining the tertiary creep-damage constants. Two complementary analytical procedure was recently developed (Strain approach and Damage approach) to mitigate this issue [11]. In the strain approach (SA), the damage evolution equation is incorporated into the creep strain rate equation such that the experimental creep strain can be directly applied to find the constants. In the damage approach (DA), finite difference is applied to obtain the creep strain rate and the creep strain rate plugged into the creep strain rate equation to calculate "analytical damage". This analytical damage is then used to calibrate the damage rate equation. A brief discussion of these two approaches is follows.

Strain Approach

In the Strain Approach (SA) the damage prediction, [Eq. (21)] is introduced into the creep strain rate [Eq. (18)] and integration is performed to get a creep strain equation. Then the *M* constraint [Eq. (22)], is introduced and the equation simplified to produce the following creep strain formula

$$\varepsilon_{cr}(t) = \frac{A\cdot(\theta+1)\cdot[t\cdot\left(\frac{\sigma}{\tau}\right)^{n} - t_r\cdot\left(\frac{\sigma}{\tau}\right)^{n} + \mathrm{t}_r\cdot\sigma^{n}]}{1+\theta-n}, \tau = \left(1-\frac{t}{t_r}\right)^{\frac{1}{1+\theta}} \tag{24}$$

here, both the *M* and ψ tertiary creep-damage constants are eliminated. The ψ constant can be set arbitrarily to any number greater than or equal unity. The *M* constant should be calculated from

[Eq. (22)]. The constant, θ can be determined from available creep strain data using the creep strain [Eq. (24)] and regression software.

Damage Approach

In the Damage Approach (DA), the creep strain rate, [Eq. (18)] is algebraically rearranged to get analytical damage at each time step

$$\omega\left(\dot{\varepsilon}_{cr}\right)=\frac{\left(\frac{\dot{\varepsilon}_{cr}}{A}\right)^{1/n}-\sigma}{\left(\frac{\dot{\varepsilon}_{cr}}{A}\right)^{1/n}} \tag{25}$$

Thus the creep strain rate from experiments, $\dot{\varepsilon}_{cr}$ will produce an analytic damage curve, $\omega(\dot{\varepsilon}_{cr})$. The introduction of *M* constraint [Eq.(22)] into the damage prediction [Eq. (21)] gives the following

$$\omega(t)=1-\left[\frac{t}{t_r}\cdot[(1-\omega_r)^{\theta+1}-1]+1\right]^{\frac{1}{\theta+1}} \tag{26}$$

where the tertiary creep-damage constant, θ, is the only unknown. The constant θ can be determined by using the available creep strain data, the analytic damage, [Eq. (21)], the modified damage, [Eq. (26)], and regression analysis software. The ψ constant can be set arbitrarily to any number greater than or equal unity. The *M* constant should be calculated from [Eq. (22)].

Limitation of Local Approach

Kachanov-Rabotnov's (KR) local CDM approach shows stress sensitivity. In the KR approach damage is assumed to be an internal state variable which evolves from zero to critical damage, $(0\le\omega<\omega_{cr})$, where critical damage is often assumed equal to unity $(\omega_{cr}=1)$. Qi et al. and

Lemaitre made it clear that the assumption that critical damage is equal to unity is not realistic [19, 37]. The value of critical damage is less than unity and varies from 0.2-0.8 for most metals. Chaboche, explained that KR model uses local cross-sectional area reduction to account for effective stress amplification during damage, but in reality, microscopic damage gives little loss of effective area before crack initiation thus the damage variable, ω is a very small value until a large fraction of life has been exhausted [38]. He proposed that an improvement can be obtained by introducing an additional damage parameter. The KR model tries to model both the creep-damage and fracture within a continuous function; however, the very high rate of damage that occurs during fracture cannot be accommodated, thus the KR model develops critical damage values equal to much less than unity. Penny stated that the damage rates of KR model become excessively high at about 90% of a lifetime such that the critical damage ω_{cr} cannot be unity [31]. This becomes clear when examining the damage function of KR [Eq. (18) and (19)], as follows

$$\dot{\varepsilon}_{cr} = f\left(\frac{1}{(1-\omega)^{n}}\right) g\left(\sigma, \mathrm{T}\right) \tag{27}$$

$$\dot{\omega} = f\left(\frac{1}{(1-\omega)^{\theta}}\right) g(\sigma, \mathrm{T}) \tag{28}$$

when damage approaches unity these functions becomes infinitely large suggesting that these functions attempt to encapsulate both the continuous damage of creep and the instant of fracture [45]. For further proof, taking the variation of damage $\partial\omega(t)$, [Eq. (26)], with an infinitesimal variation of stress $\partial\sigma(t)$ produces

$$\partial\omega(t) = \psi \frac{M\sigma(t)^{\psi} t}{[1-(\theta+1)M\sigma(t)^{\psi} t]^{\frac{\theta}{\theta+1}}} \frac{\partial\sigma(t)}{\sigma(t)} \tag{29}$$

Replacing the portion, $M\sigma(t)^{\psi}t$, by rearranging [Eq. (26)] and introducing it into the above equation provides

$$\partial\omega(t) = \psi \frac{1-(1-\omega)^{\theta+1}}{(1-\omega)^{\theta}} \frac{\partial\sigma(t)}{\sigma(t)} \tag{30}$$

For an infinitesimal variation of stress, $\partial\sigma(t)$, when damage is critical $(\omega_{cr} \to 1)$, the damage variation $\partial\omega(t)$ is near infinite as the denominator becomes zero. Damage cannot be equal to unity. To overcome these issues, a damage evolution equation that exhibits a finite variation of damage $\partial\omega(t)$ for an infinitesimal variation of stress $\partial\sigma(t)$ is needed.

Numerous investigators have written papers describe the limitations of the local CDM approach [36,46-48]. These authors observed damage localization around the crack tip in FEM analysis and experienced mesh dependency where the FE solutions upon mesh refinement do not converge to a single solution. Extensive mesh dependence studies on the KR and Sinh models have been reported elsewhere [38,39].

Sinh Model

In this study, a CDM-based Sinh creep-damage constitutive model is used. A detailed monograph on this model is available [41]. Classically, the simplest stage of creep to analysis is the secondary stage where a balance between hardening and recovery mechanisms leads to a steady-state/minimum creep strain rate, $\dot{\varepsilon}_{\min}$. The Mcvetty minimum creep strain rate equation

$$\dot{\varepsilon}_c = B\sinh\left(\sigma/\sigma_s\right) \tag{31}$$

can fit the non-linear bend observed in minimum creep strain rate versus stress on a log-log scale. The constants B (1/s) and σ_s (MPa) are the creep coefficient and secondary creep mechanism-transition stress respectively [49].

Creep Strain Rate and Analytical Damage

The CDM based damage variable has three functions; to model the tertiary creep regime, track the evolution of creep-damage, and predict rupture. To achieve these goals the damage variable, ω, is coupled to the secondary viscous function as follows

$$\dot{\varepsilon}_{sc} = f(\sigma)\cdot g(T)\cdot h(\omega) \tag{32}$$

where the $h(\omega)$ function describes how the current state of damage influences the strain rate. A detailed monograph of the damage evolution has been derived [41].

Introducing $h(\omega)$, into the total creep strain rate, $\dot{\varepsilon}_{cr}$, [Eq. (31)], and solving for $h(\omega)$ produces

$$h\left[\omega(t)\right] = \frac{\dot{\varepsilon}_{cr}(t)}{B\sinh\left(\sigma/\sigma_s\right)} \tag{33}$$

It is proposed that $h(\omega) = \exp(\lambda\omega^p)$, where λ and p are unit-less material constants. Introducing it into above equation and solving for damage provides

$$\omega^*(t) = \left\{\frac{1}{\lambda}\ln\left[\frac{\dot{\varepsilon}_{cr}(t)}{B\sinh\left(\sigma/\sigma_s\right)}\right]\right\}^{1/p} \tag{34}$$

where $\omega^*(t)$ is the analytical damage derived from the creep strain rate, $\dot{\varepsilon}_{cr}(t)$. Considering the time just before fracture $t \simeq t_r$, where $\dot{\omega}_{cr} = 1$, the creep strain rate, [Eq. (33)], becomes

$$\begin{aligned} &\dot{\varepsilon}_{cr} = \dot{\varepsilon}_{final} \approx B\sinh\left(\sigma/\sigma_s\right)\exp(\lambda) \\ &\lambda = \ln\left(\frac{\dot{\varepsilon}_{final}}{\dot{\varepsilon}_{\min}}\right); \qquad \dot{\varepsilon}_{\min} = B\sinh\left(\sigma/\sigma_s\right) \end{aligned} \tag{35}$$

where the material constant λ can be determined directly from experimental data. It is proposed that the best value for *p* is 3/2 unit-less. Thus, the creep strain rate of the Sinh model becomes

$$\dot{\varepsilon}_{cr} = B\sinh\left(\sigma/\sigma_s\right)\exp\left(\lambda\omega^{3/2}\right) \tag{36}$$

Damage model

Using the concept of Liu and Murakami [45], that the problem of stress-sensitivity and mesh-dependence can be mitigated by representing damage as an exponential function within the creep rate and damage evolution equations, the following damage evolution equation is proposed

$$\dot{\omega} = \frac{Q\left[1-\exp\left(-\phi\right)\right]}{\phi}\sinh\left(\frac{\sigma}{\sigma_t}\right)^{\chi}\exp\left(\phi\omega\right) \tag{37}$$

where Q, ϕ, χ, and σ_t are material constants that must be greater than zero. The portion $\left[1-\exp\left(-\phi\right)\right]/\phi$ is necessary to avoid an undefined error when the damage evolution equation is integrated. Integration of the damage rate [Eq.(37)] with the assumption of the initial time, t_o and initial damage, ω_0 equal to zero, gives the following damage and rupture prediction

$$\omega\left(t\right) = -\frac{1}{\phi}\ln\left[1-\left[1-\exp\left(-\phi\right)\right]\frac{t}{t_r}\right]; \qquad t_r = \left[Q\sinh\left(\frac{\sigma}{\sigma_t}\right)^{\chi}\right]^{-1} \tag{38}$$

where the constants Q, χ, and σ_t can be found using stress-rupture data. The remaining constants ϕ, can be determined simultaneously by minimizing the error of the following equation [a combination of Eqs. (34) and (38)]

$$\begin{aligned} &\omega(t) = \omega^{*}(t) \\ &-\frac{1}{\phi}\ln\left[1-\left[1-\exp\left(-\phi\right)\right]\frac{t}{t_r}\right] = \left\{\frac{1}{\lambda}\ln\left[\frac{\dot{\varepsilon}_{cr}(t)}{B\sinh\left(\sigma/\sigma_s\right)}\right]\right\}^{1/p} \end{aligned} \tag{39}$$

It can be observed from [Eq. (38)] that the damage trajectory depends on the material constant ϕ. Taking the variation of damage, $\partial\omega(t)$ with an infinitesimal variation of stress, $\partial\sigma(t)$ [Eq. (38)] and replacing the portion $Q\sinh\left(\sigma/\sigma_t\right)^{\chi}$ by rearranging [Eq. (38)] gives

$$\partial\omega(t) = \frac{[\exp(\phi\omega) - 1]}{\phi} \frac{\partial\sigma(t)}{\sigma_t} \tag{40}$$

where when damage is critical $(\omega_r \to 1)$, the variation of damage, $\partial\omega(t)$ does not become infinite and remains finite throughout the damage evolution.

Chapter 3: Materials and Experimental Data

3.1 Alloy 304 Stainless Steel (SS)

The alloy 304 stainless steel (304SS) is a Fe-Cr-Ni alloy that has high temperature, oxidation, and corrosion resistance [50]. Experimental data is obtained from a study on the statistical creep properties of 304SS at elevated temperature [51]. Creep data in the form of minimum-creep-strain-rate, stress-rupture, and creep deformation are collected from various courses and used. The minimum-creep-strain-rate data for 304 SS at eleven isotherms are shown in Figure 3.1. It is observed that minimum-creep-strain-rate data exhibit wide range of variation; data from various sources overlaps. Stress-rupture data for 304 SS collected from various sources are shown in Figure 3.2. It is observed that data from various sources does not or slightly overlaps, exhibits stability over minimum-creep-strain-rate data. Creep tests were repeated five times and performed according to ASTM E139 at 160, 180, 240, 260, 300, and 320 MPa stress from 600°C to 700°C as shown in Figure 3.3. The chemical composition of 304SS is provided in Table 2.

Table 2 – Chemical composition of 304SS (% wt.) [50]

C	Mn	P	S	Si	Cr	Ni	N	Cu	Fe
0.020	1.83	0.029	0.009	0.4	18.22	8.13	0.102	2.06	Balance

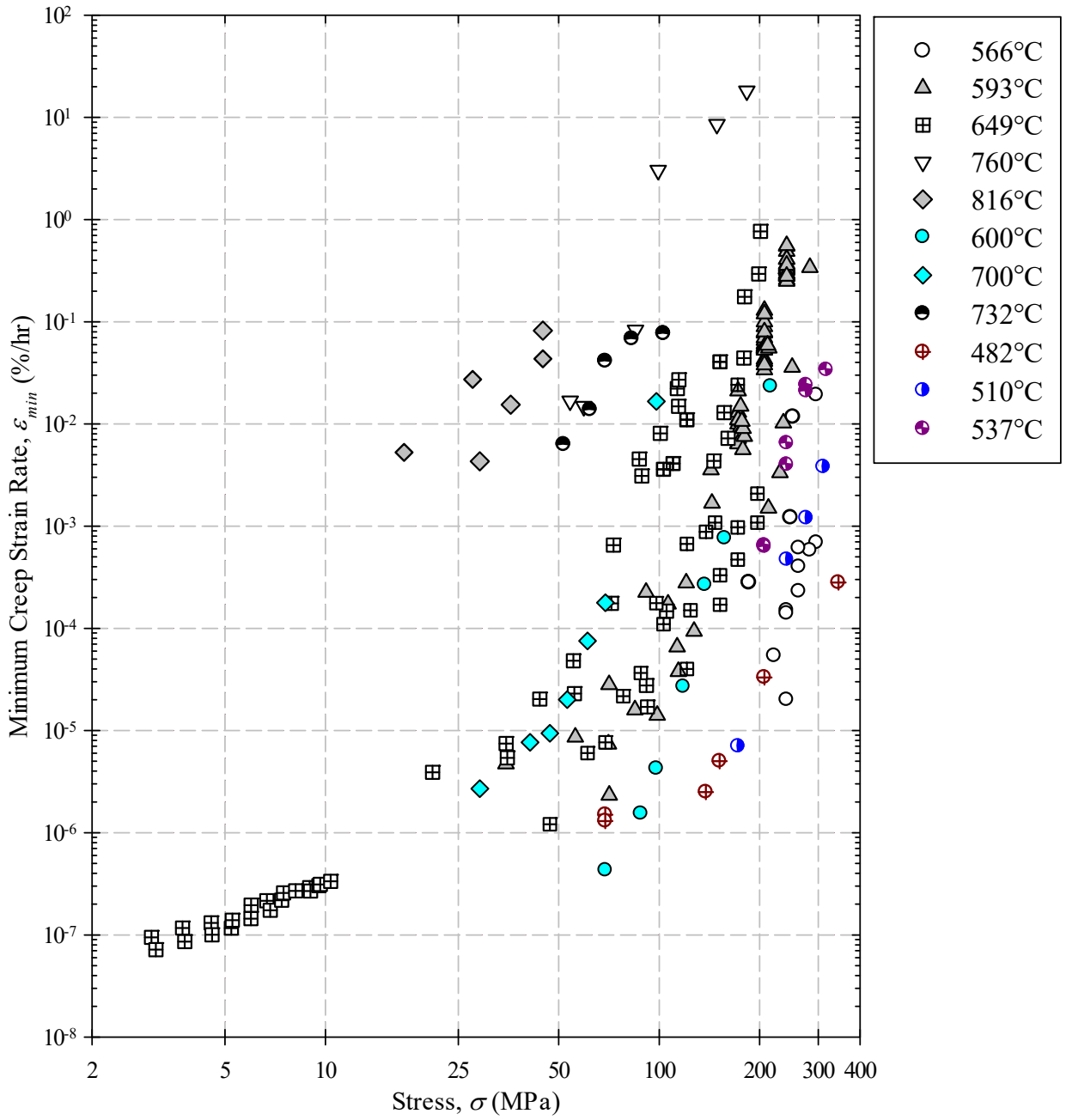

Figure 3.1 – Minimum-creep-stain-rate vs stress data for 304 SS at 11 isotherms ranging from 482 to 816°C

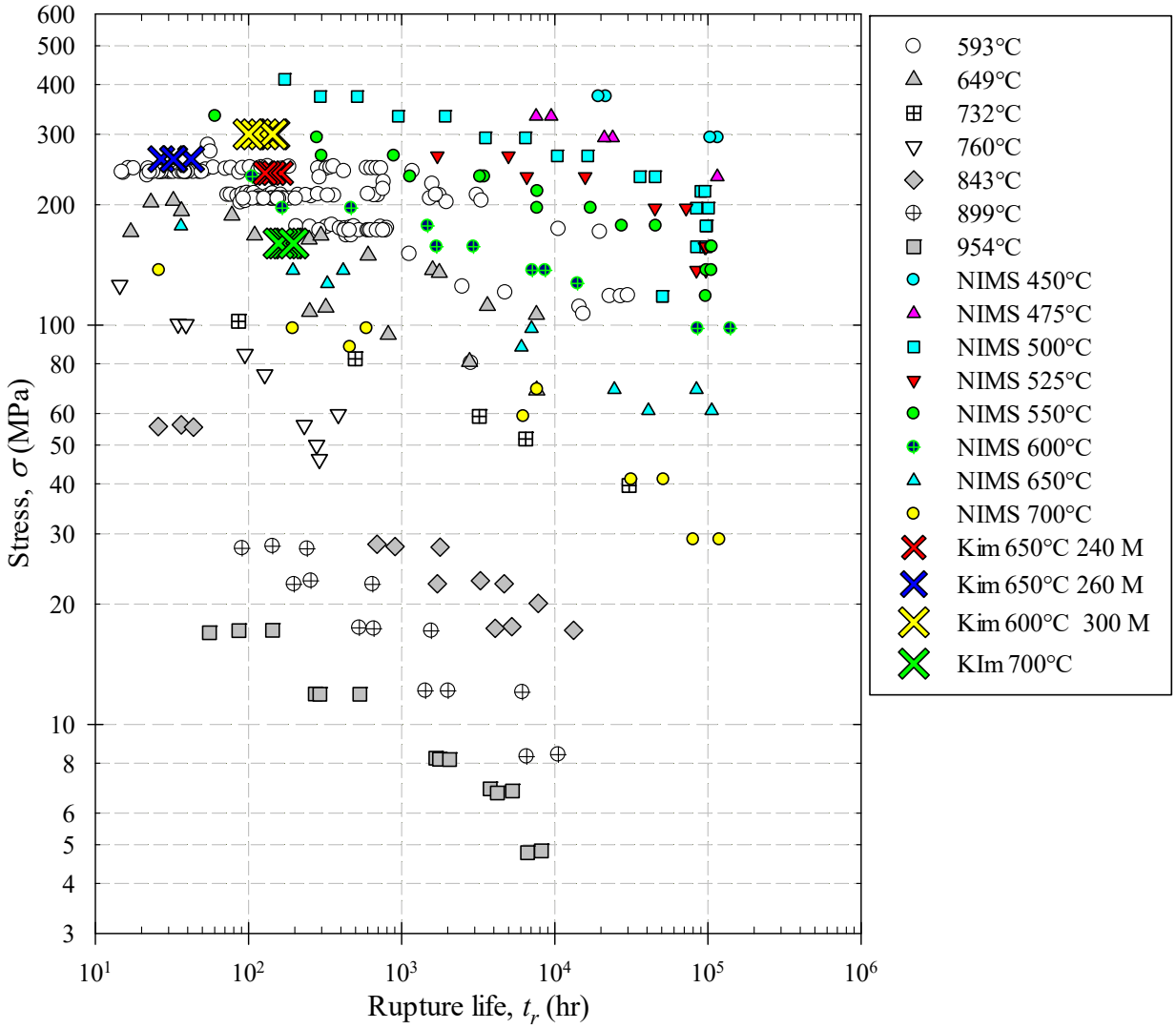

Figure 3.2 – Stress-rupture data for 304 SS collected from various sources

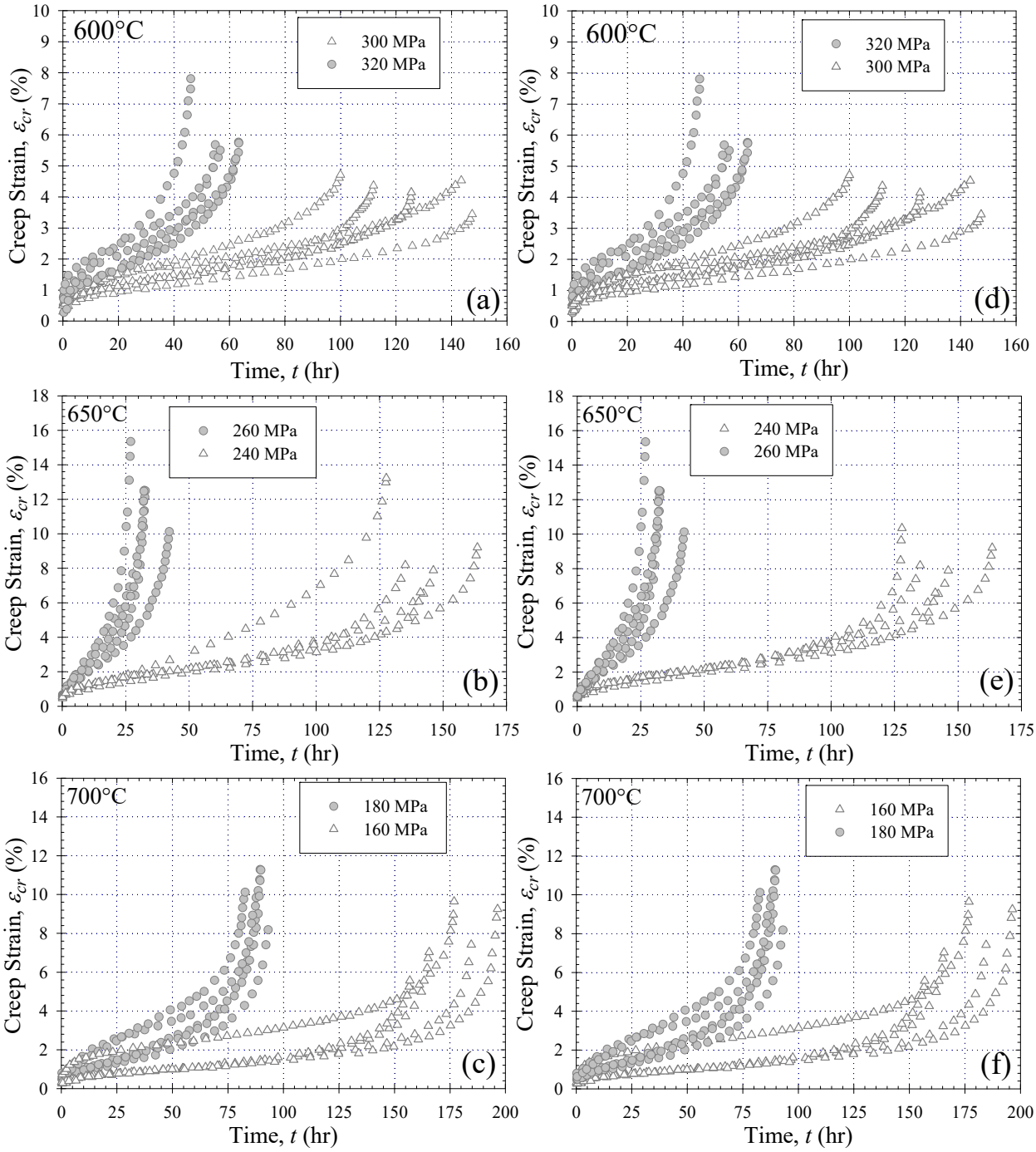

Figure 3.3 – Creep deformation curves for 304 SS (a,d) 600, (b,e) 650, and (c,f) 700°C

3.2 HASTELLOY X

Hastelloy X has been widely used in the hot combustion zones of IGT's (Industrial Gas Turbine) such as transition ducts, combustor cans, spray bars, afterburners, and tailpipes [91]. Stress-rupture data at seven isotherm is shown in Figure 3.4. Experimental data at two temperatures (1200-1600°F) and four stress conditions is collected as depicted in Figure 3.5. The creep ductility and rupture life are listed in **Table 3**. Hastelloy X does not exhibit the primary creep stage; therefore, it is not studied.

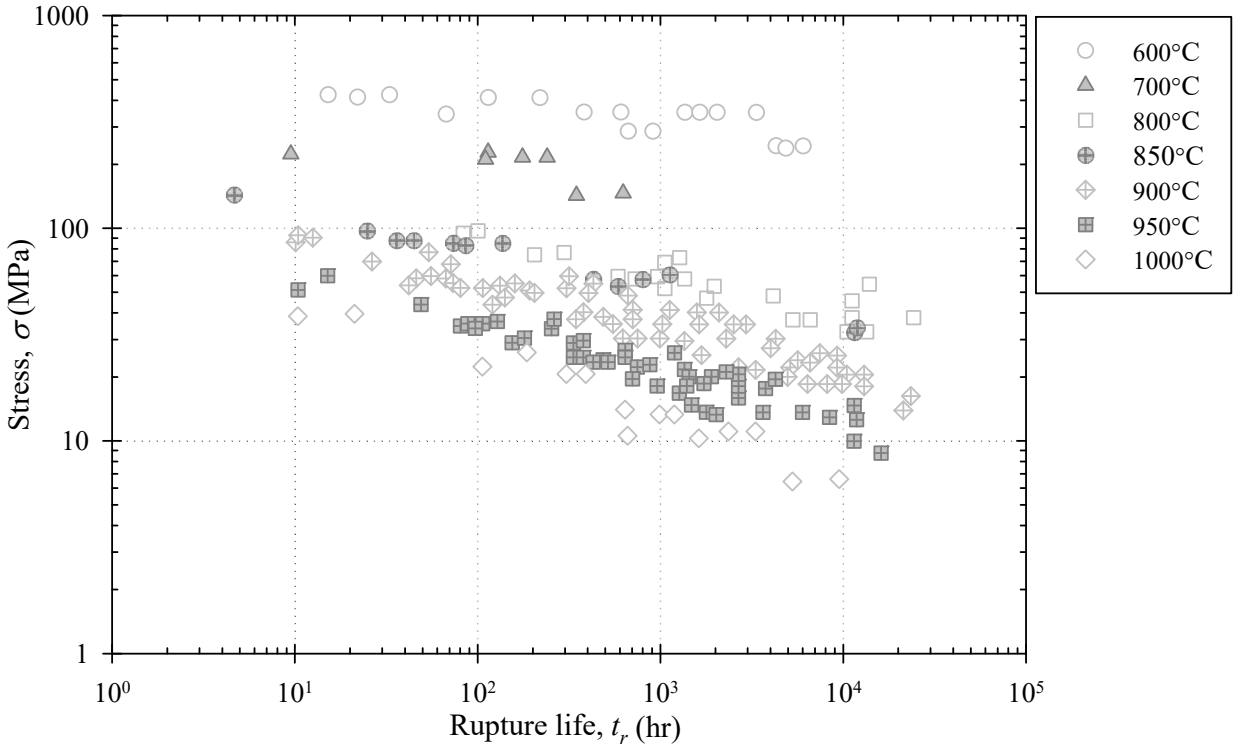

Figure 3.4 – Stress-rupture data for Hastelloy X at seven isotherm ranging from 600 to 1000°C

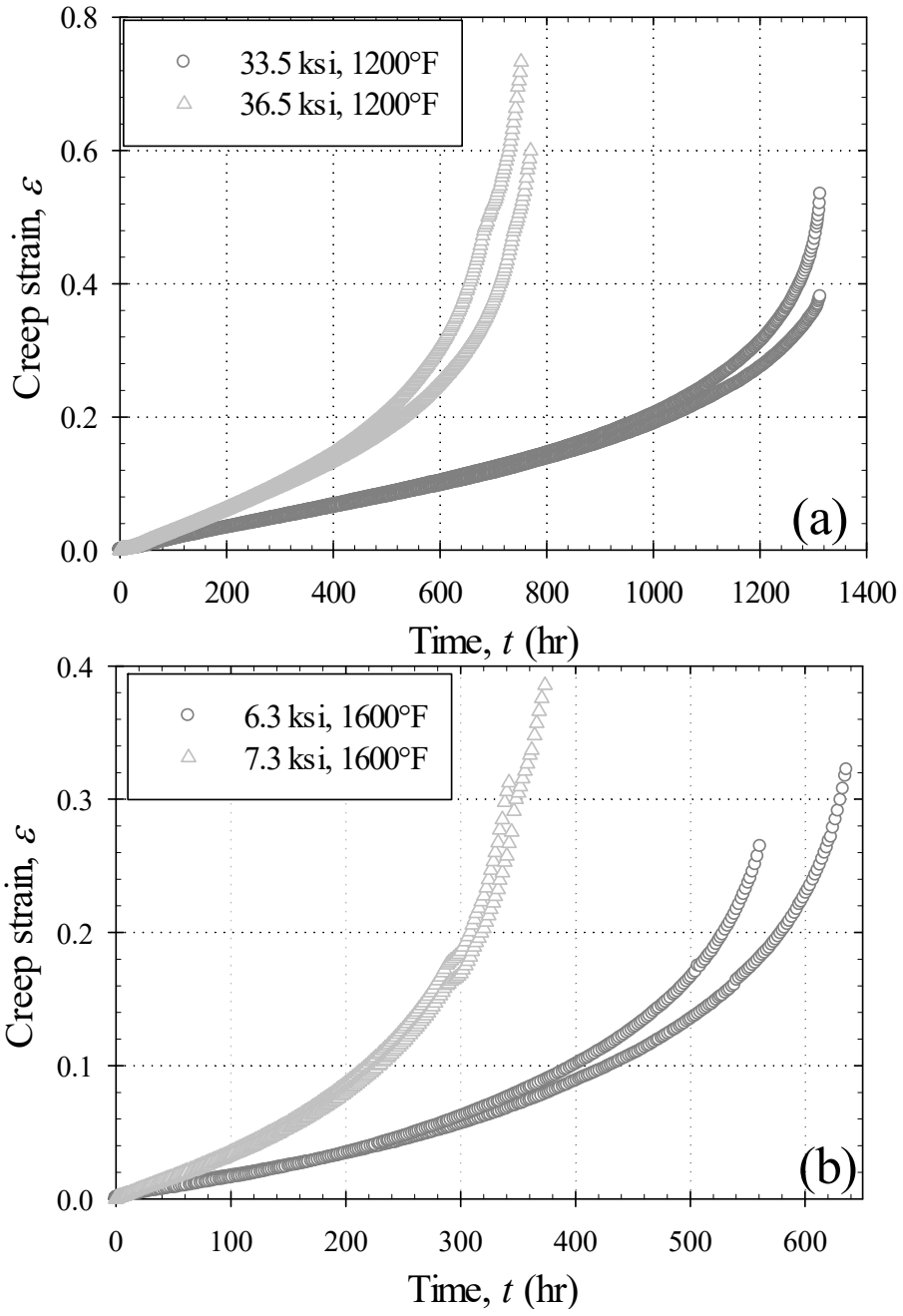

Figure 3.5 – Creep Deformation of Hastelloy X (a) 1200°F and (b) 1600°F

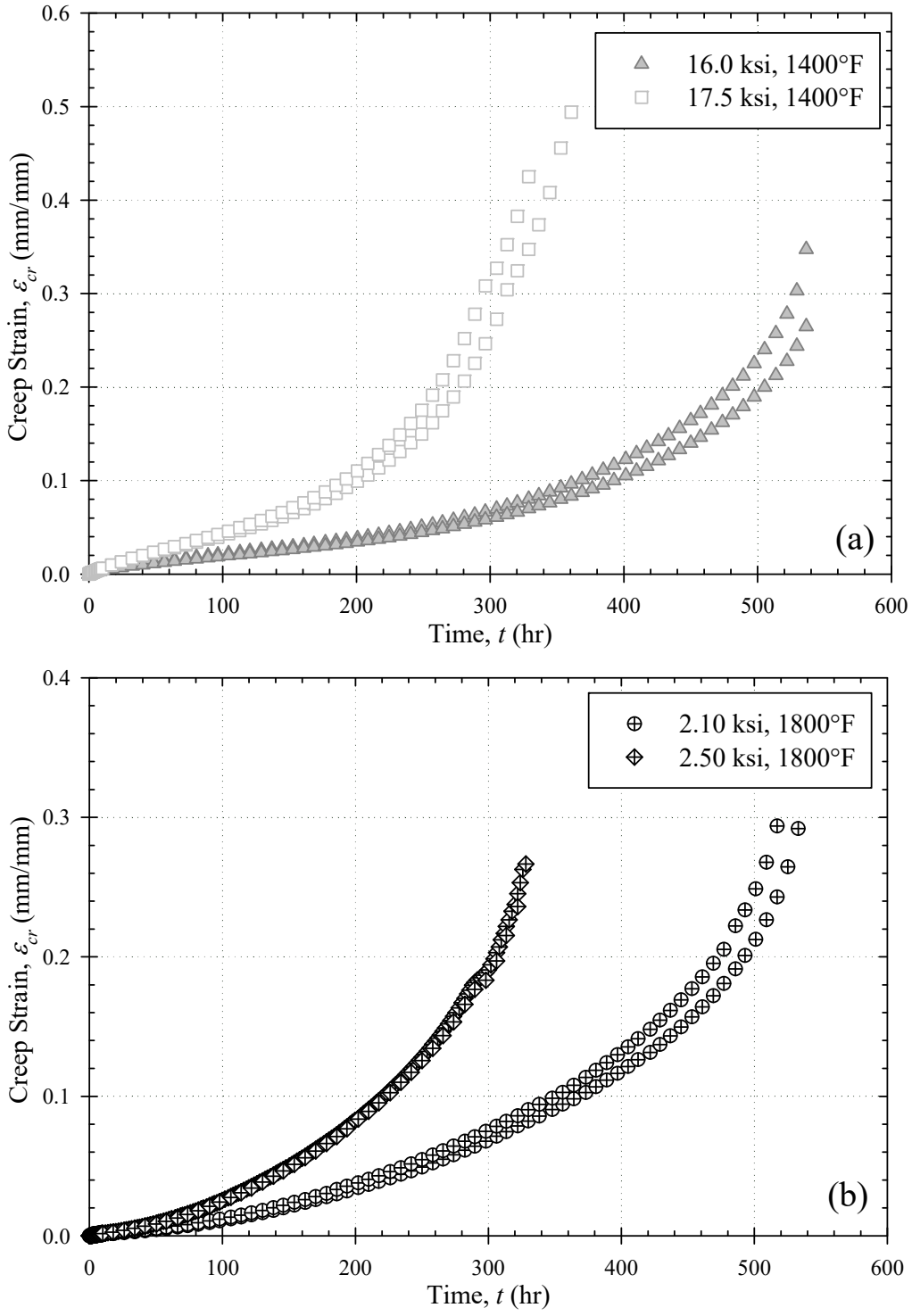

Figure 3.6 – Creep Deformation of Hastelloy X (a) 1400°F and (b) 1800°F

Table 3 – Creep deformation and rupture properties at 1200°F to 1800°F from Siemens

Temperature, T		Stress, σ		Minimum Creep Strain Rate, $\dot{\varepsilon}_{\min}$	Creep Ductility, ε_r	Rupture Time, t_r
(°C)	(°F)	(MPa)	(ksi)	(1/hr)	(%)	(hr)
649	1200	231.0	33.5	1.318E-04	53.43	1314
649	1200	231.0	33.5	1.259E-04	38.02	1314
649	1200	251.7	36.5	3.336E-04	73.31	751.6
649	1200	251.7	36.5	2.901E-04	59.96	769.7
760	1400	110.3	16	1.660E-04	35.50	537.2
760	1400	110.3	16	1.400E-04	27.11	537.2
760	1400	120.7	17.5	3.660E-04	50.88	362.9
760	1400	120.7	17.5	4.000E-04	44.26	332.7
871	1600	43.4	6.3	1.121E-04	32.18	636.5
871	1600	43.4	6.3	1.180E-04	26.44	561.3
871	1600	50.3	7.3	3.207E-04	31.25	342.1
871	1600	50.3	7.3	2.861E-04	38.56	373.3
982	1800	14.5	2.1	4.256E-05	29.20	533
982	1800	14.5	2.1	4.260E-05	30.06	519
982	1800	17.2	2.5	8.652E-05	26.65	328.3
982	1800	17.2	2.5	8.660E-05	25.80	332.5

3.3 GRADE P91

The P91 steel alloy has been widely applied in fossil energy power plant components such as superheater coils, headers, steam pipes, etc. due to its high-temperature strength and oxidation resistance [12]. According to ASTM standard A335, alloy P91 has a room temperature tensile strength of 585 MPa, yield strength of 415 MPa, and elongation minimum of 30% in the longitudinal and 20% in the transverse direction [13]. Experimental data for four isotherms (550, 600, 650, 700°C) of alloy P91 are collected from the National Institute for Materials Science (NIMS) database. The creep-rupture data includes experiments of alloy P91 tubes, plates, and

pipes as depicted in Figure 3.7. Thus, it can be considered the data represents the creep behavior of alloy P91 free of geometrical effect. The chemical composition of alloy P91 is presented in Table 4.

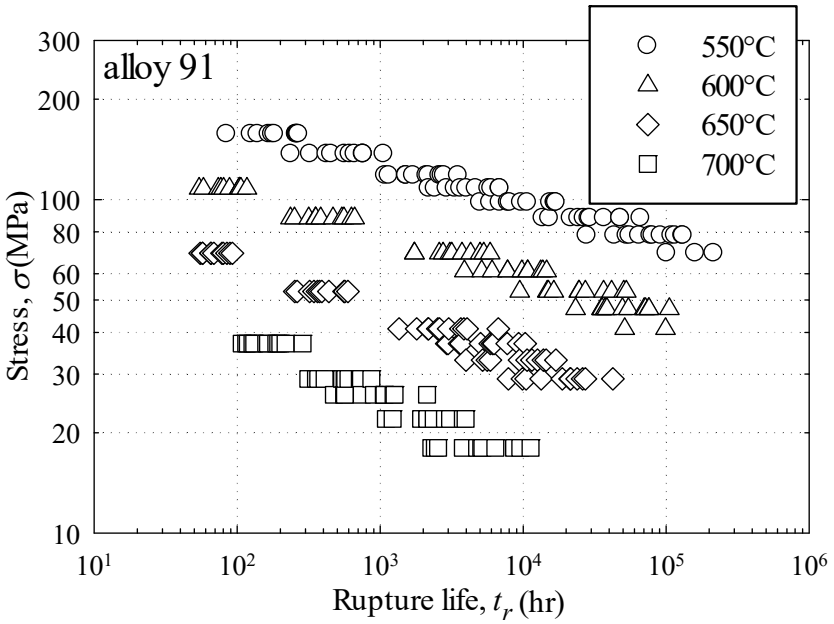

Figure 3.7 – Stress-rupture data for alloy P91 at four isotherm ranging from 550 to 700°C

Table 4 – Chemical composition of alloy P91 steel wt%

C	0.08-0.12	**Mo**	0.85-1.05	**Zr**	0.00-0.01
Mn	0.30-0.60	**N**	0.03-0.07	**Ti**	0.00-0.01
P	0.00-0.02	**V**	0.18-0.25	**Cr**	8.00-9.60
S	0.00-0.01	**Al**	0.00-0.02	**Ni**	0.00-0.40
Si	0.20-0.50	**Nb**	0.06-0.10	**Fe**	balance

3.4 316 SS

The subject material is 316 Stainless Steel (316SS). Creep rupture data for this material is gathered from multiple public and private sources. [52,57] The list of sources and number of creep rupture data points obtained from each is shown in Table 1. A stress-rupture plot of this data is presented in Figure 1. The collected data contains 316SS in the following forms: bar, pipe, plate, and tube; and exposed to the following thermomechanical processes: annealed, cold drawn, hot rolled, and quenched. In this study, tube form is arbitrarily chosen as the metadata of interest. The temperature range of the parsed dataset is: 600°C, 650°C, 700°C, and 750°C.

Table 5 – Creep rupture data source for 316 SS [52,57]

ASM Atlas of Creep and Stress-Rupture Curve	ASTM STP 552
ASTM DS 5-S1	NIMS Creep Database
ASTM STP 124	ORNL-5237

Table 6 – Summary of the Stress-rupture data

Material	Number of data points	Temperature (°C)		Stress range (MPa)	Source
		Isotherms	Range		
P91	272	4	550-700	18.0-157.00	[5]
316 SS	1055	21	482-871	18.0-497.80	[5]
304 SS	242	9	593-954	4.77-320.26	[41]
Hastelloy X	184	7	600-1000	6.44-424.60	[128]

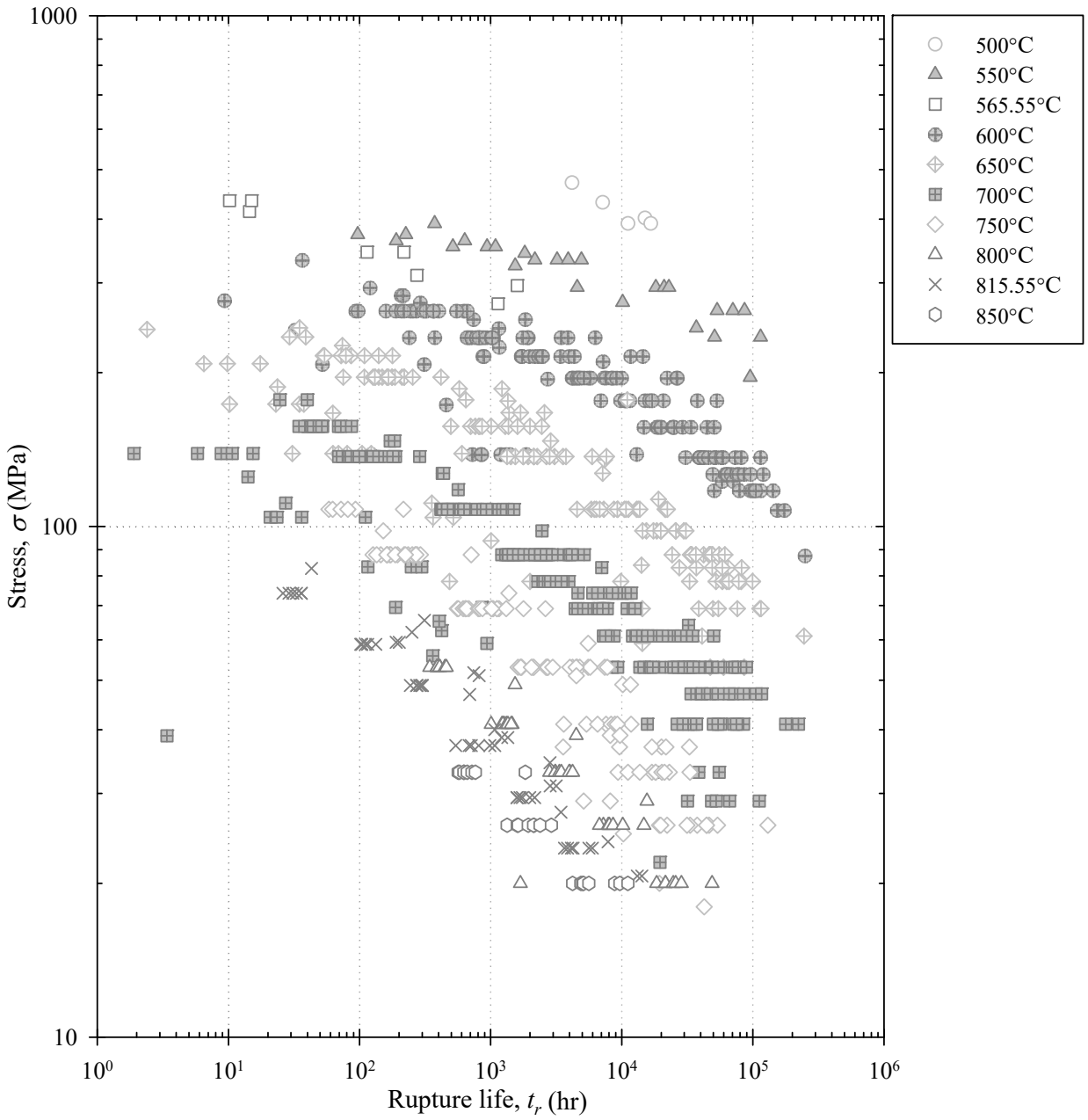

Figure 3.8 – Stress-rupture data for 316 SS at ten isotherm ranging from 500 to 850°C

Chapter 4: Adaptive Creep Modeling: Classic Rupture Model

4.1 INTRODUCTION

Many time-temperature parameter (TTP) models have been developed to predict the rupture of components subjected to creep condition. In these models generally, the parameter is fit to a function of stress. The selection of an appropriate "stress-parameter" function is critical for the accurate extrapolation of rupture time. Overall, TTP models are functionally similar and "mirror pairs" (isostress lines are mirroring each other) are common. Using this knowledge, a "mirror pair" metamodel is introduced that incorporates twelve time-temperature parameter submodels (eight existing and four new) into a single equation. This is possible by introducing material constants that switch on-and-off (as step function) to convert the metamodel into any submodel. As a result, the metamodel can be used to efficiently evaluate the twelve submodels. A literature review is performed to prepare a guideline for the selection of the most physically realistic TTP model and stress-parameter function. A MATLAB code is developed according to the guideline that can: (1) calculate the parameter and determine the most suitable stress-parameter function; (2) calibrate material constants; (3) report the normalized mean square error (NMSE); and (4) recommend the most physically realistic TTP model for a given experimental data. A detailed analysis of the metamodel and twelve submodels is performed using four isotherms of alloy P91 stress-rupture data. Secondary analysis and validation are performed on alloy 316 SS, 304 SS, and Hastelloy X.

Motivation

Recent drive to increase the efficiency of existing fossil energy (FE) power plants and the development of Advanced Ultrasupercritical (A-USC) power plants have led to design with steam pressure above 4000 psi and temperature exceeding 1400°F. The complexity of the applied thermal and mechanical loading instigates mechanical fatigue, creep and oxidation dominant damage

mechanism where creep damage becomes significant at an operating temperature above 40% of the melting temperature of the material [58].

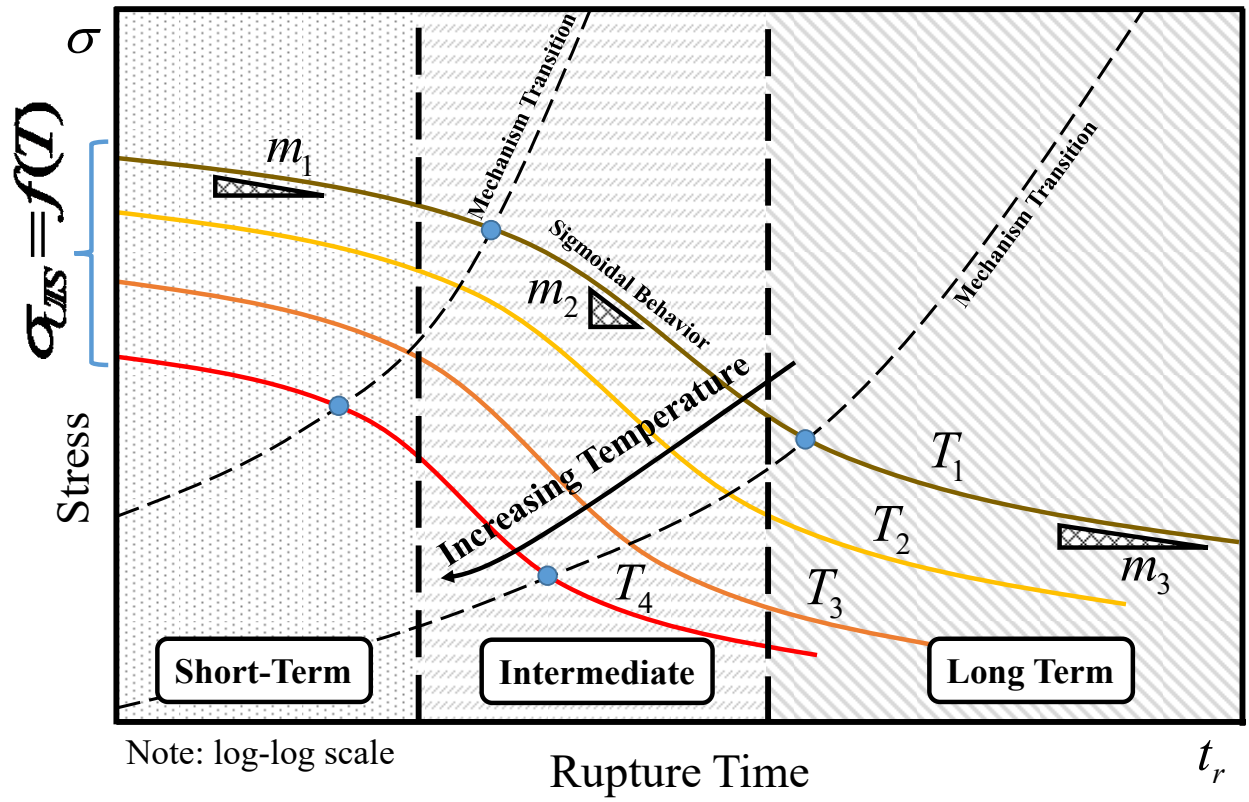

Figure 4.1 – Ideal creep rupture curve: The dotted, horizontal lined, and inclined-line pattern represent the short-term, intermediate, and long-term region respectively where the vertical dashed line represents the transition between mechanisms. In ideal case, at $\sigma = \sigma_{UTS}$ creep life is instantaneous $(t_r = 0)$ and at $\sigma \to 0$ creep life is infinite $(t_r \to 0)$.

Creep-rupture

In this study creep rupture prediction using time-temperature models are considered. Ideal creep-rupture curves at different temperature are illustrated in Figure 4.1. The creep-rupture curves can be separated into three regions: short-term, intermediate, and long-term creep. In the short-term region, operating stress is high (near UTS); a small change in applied stress leads to a large change

in predicted life. In the intermediate region, the creep mechanism is comparatively stable. And in the long-term region, an endurance limiting stress is expected, below which the creep life is infinite.

Problem

Over the years, many time-temperature models have been developed to predict creep rupture. A chronological detail of model developments is reported elsewhere [59, 60]. Each model has been proved to be accurate for at least one material over a specific range of stress and temperature; however, no single model can perform accurately for the wide variety of engineering alloys available nor meet the analysts' expectations for every service conditions. In addition, another primary concern to FE practitioners is a determination of which model is the "best", capable of reproducing the mechanisms excepted in an intended design accurately. To address these problems a novel metamodeling approach is proposed that combine and exploit the functional relationships between the existing creep models. A "metamodel" can be described as a combinational model, derived from rearranging, modifying, and/or expanding the functional relationships between different models. A metamodel can exhibit unique attributes that could potentially make them superior to the originals. A recent example is the application of metamodeling to Sin-hyperbolic, Theta projection, and MPC Omega creep deformation models to derived six new combinational submodels [59-61]. The analytic solution to determine the Sin-hyperbolic model is reported elsewhere [38-39].

4.1.1 Objective

The objectives of this study are to

A. introduce a "mirror pair" metamodel that incorporates twelve time-temperature parameter submodels into a single equation that facilitates the selection of the most suitable submodel.
B. present a guideline for the selection of the most physically realistic time-temperature parameter model and stress-parameter function from the literature review.
C. demonstrate the predictability of the "mirror pair" metamodel by validating against stress-rupture data sets for four different materials using a MATLAB algorithm.

In this study, five steps are executed to accomplish these objectives. First, eight time-temperature parameter models named Larson-Miller (LM), Manson-Haferd (MH), Manson-Brown (MB), Orr-Sherby-Dorn (OSD), Manson-Succop (MS), Goldhoff-Sherby (GS), Graham-Walles (GW), and Chitty-Duval (CD) are collected and studied. An additional four new models are derived by exploiting the similarities between the existing models. Next, the twelve models are paired into twos; grouped together as "mirror models" by the mirror like similarities of their isostress lines. Thus, six groups of "mirror models" is formed that simplifies model characteristic analysis. These TTP models tend to follow the same general framework, rules, and constraints such that they can be mathematically exercised towards metamodeling. A metamodel incorporating the twelve models is proposed to accomplish these objectives. Third, a literature review is performed to prepare a guideline for the selection of the most physically realistic TTP model and stress-parameter function. The effects of five different form of stress-parameter functions on the interpolation/extrapolation performance and the strengthening/weakening creep rupture behavior is discussed. Fourth, a MATLAB code is developed to determine:

(1) the most suitable stress-parameter function for each model by regression analysis;

(2) the material constants of the models;

(3) the Normalized Mean Square Error (NMSE) of the models;

(4) the most suitable model for the subject material.

Fifth, the metamodel is calibrated to four isotherms (550, 600, 650, 700°C) of creep data for alloy P91 using the MATLAB code. The metamodeling approach is further validated against the stress-rupture data for alloy 316 SS, 304 SS, and Hastelloy X.

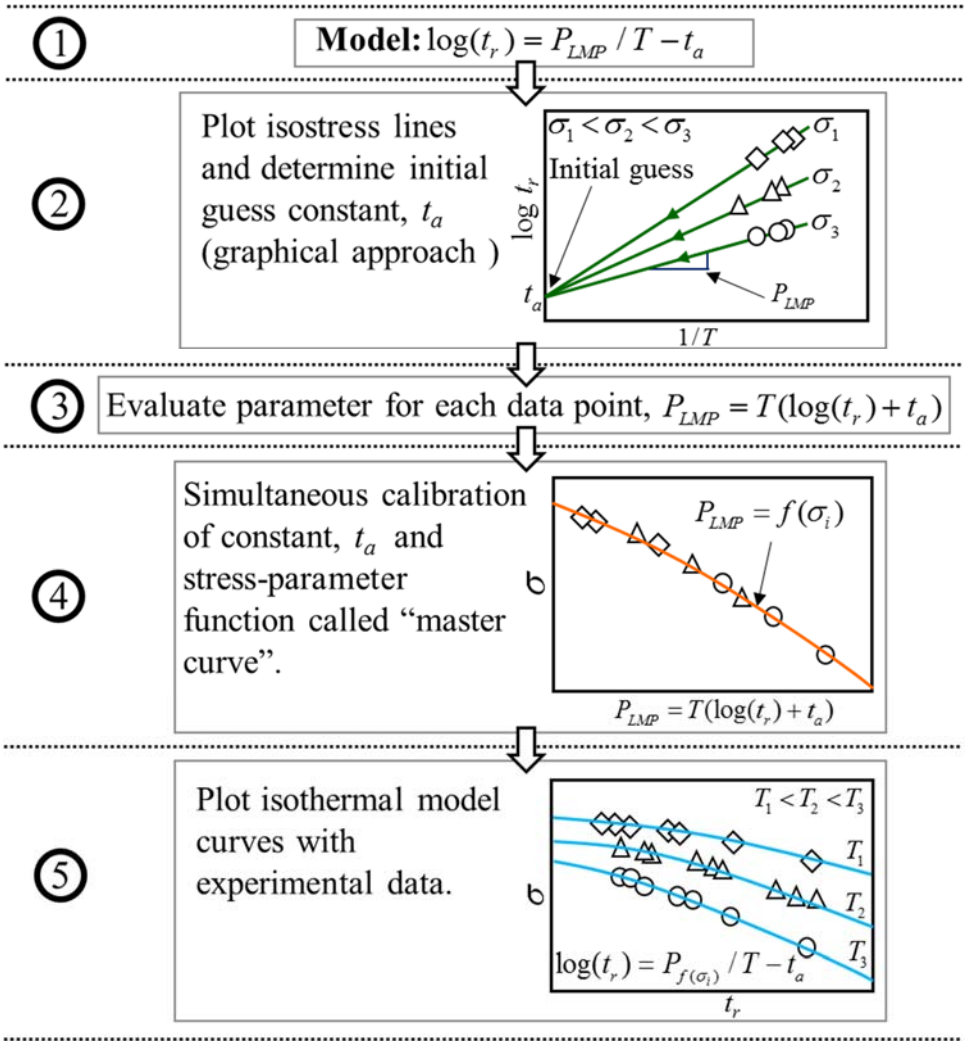

Figure 4.2 – Step-by-step process to fit Larson-Miller model

Table 7 – Summary of the time-temperature parameter creep rupture models [17,62-68]

$$P_{HS} = \frac{\log(t_r) - \alpha_0 - \alpha_1 T^r}{(T^r - \alpha_2{}^r)^q}$$

Model	Year	Parameter equation	Eqn.	Material constants	Characteristics	Metamodel condition	Ref.
Larson-Miller (LM)	1952	$P_{LMP} = T(\log(t_r) - t_a)$	(41)	$P_{LMP}(\sigma)$, t_a	Cy, L, NP, Sp	$\alpha_2 = \alpha_1 = 0$ $r = -1, q = 1$	[62]
Manson-Haferd (MH)	1953	$P_{MH} = \frac{\log(t_r) - \log(t_a)}{T - T_a}$	(42)	$P_{MH}(\sigma)$, T_a, t_a	Cxy, L, NP, Sn	$\alpha_1 = 0$ $r = q = 1$	[63]
Manson-Brown (MB)	1953	$P_{MB} = \frac{\log(t_r) - \log(t_a)}{(T - T_a)^n}$	(43)	$P_{MB}(\sigma)$, T_a, t_a, n	Cxy, NL, NP, Snv	$\alpha_1 = 0, r = 1,$ $q = n$	[17]
Orr-Sherby-Dorn (OSD)	1954	$P_{OSD} = \log(t_r) - Q/RT$	(44)	$P_{OSD}(\sigma)$, Q, R	NC, L, P, Sp=constant	$\alpha_0 = 0, r = -1,$ $q = 0$	[64]
Manson-Succop (MS)	1959	$P_{MS} = \log(t_r) - BT$	(45)	$P_{MS}(\sigma)$, B	NC, L, P, Sn=constant	$\alpha_0 = \alpha_2 = 0,$ $r = 1, q = 0$	[65]
Graham-Walles (GW)	1955	$P_{GW} = \frac{\log(t_r)}{(T - T_a)^n}$	(46)	$P_{GW}(\sigma)$, T_a, n	Cx, NL, NP, Snv	$\alpha_0 = \alpha_1 = 0,$ $r = 1,$ $q = n$	[66]
Chitty-Duval (CD)	1963	$P_{CD} = mT - \log(t_r)$	(47)	$P_{CD}, m = a\sigma^b$	NC, NP, L, Sn	$\alpha_0 = \alpha_2 = 0,$ $r = 1,$ $q = 0$	[67]
Goldhoff-Sherby (GS)	1968	$P_{GS} = \frac{\log(t_r) - \log(t_a)}{1/T - 1/T_a}$	(48)	$P_{GS}(\sigma)$, T_a, t_a	Cxy, L, NP, Sp	$\alpha_1 = 0, r = -1,$ $q = 1$	[68]
Modified-Manson-Haferd (MMH)	--	$P_{MMH} = \frac{\log(t_r) - \log(t_a)}{T}$	(49)	$P_{MMH}(\sigma)$, t_a	Cy, L, NP, Sn	$\alpha_2 = \alpha_1 = 0,$ $r = 1, q = 1$	new
Modified-Graham-Walles (MGW)	--	$P_{MGW} = \frac{\log(t_r)}{(1/T - 1/T_a)^n}$	(50)	$P_{MGW}(\sigma)$, T_a, n	Cx, NL, NP, Spv	$\alpha_0 = \alpha_1 = 0$ $r = -1, q = n$	new

Modified Chitty-Duval (MCD)	--	$P_{MCD} = \frac{m}{T} - \log(t_r)$	(51)	$P_{MCD}, m = a\sigma^b$	NC, NP, L, Sp	$r = -1,\ q = 0,$ $\alpha_0 = \alpha_2 = 0$	new
Modified-Goldhoff-Sherby (MGS)	--	$P_{MGS} = \frac{\log(t_r) - \log(t_a)}{(1/T - 1/T_a)^n}$	(52)	$P_{MGS}(\sigma),\ T_a,\ t_a$	Cxy, NL, NP, Sp	$r = -1, q = n,$ $\alpha_1 = 0$	new

Iso-stress lines are: Cx=converge to X-axis, Cy=converge to Y-axis, Cxy=point of convergence has (x,y) coordinate, NC=Non-converging, P=Parallel, NP=Non-parallel, L=Linear, NL=Non-linear, Sp=positive slope, Sn=negative slope, Spv=positive variable slope, Snv=negative variable slop

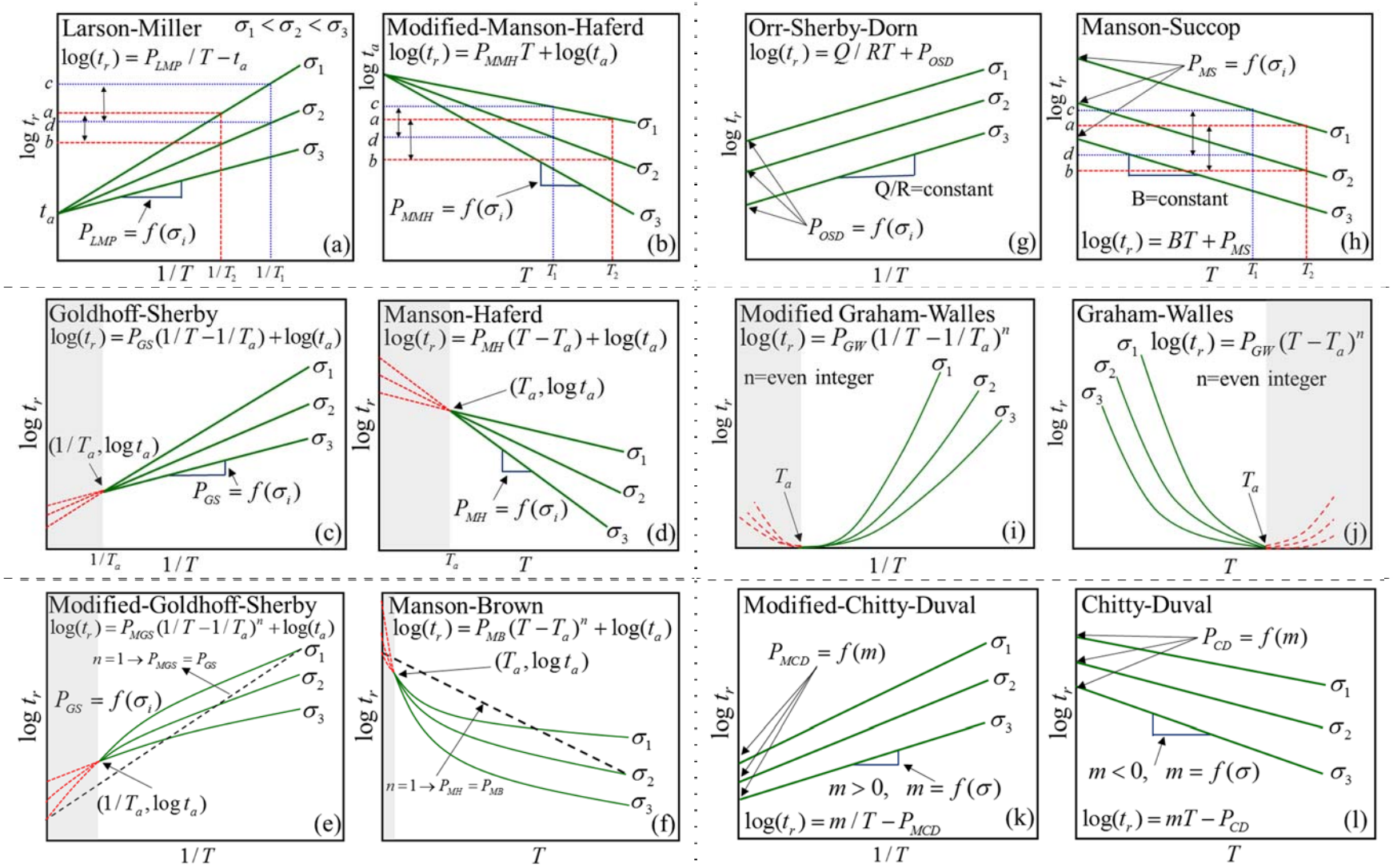

Figure 4.3 – Schematic of the isostress lines observed in twelve time-temperature parameter model

4.2 TIME-TEMPERATURE PARAMETER MODELS

4.2.1 Theory

In 1952, Larson and Miller first introduced a time-temperature parameter model to predict creep life by expanding the work of Hollomon and Jaffe [15,16]. A process to fit Larson-Miller (LM) model subdivided into five successive steps is illustrated in Figure 4.2. The LM approach specifies the expected creep life as a function of stress and temperature, $\log(t_r) = f(\sigma, T)$ as shown in Figure 4.2 (step 1). It is assumed that the isostress line on a plot of $\log t_r$ versus *1/T* converges to a point on the $\log t_r$ axis (as shown in step 2), where t_r and *T* are the rupture life and temperature respectively. An isostress line for a given stress indicates the change in rupture time with the change in operating temperature. It is assumed that the isostress line for LM model is linear with a constant slope of *P*. The slope *P*, named as a Time-temperature parameter, increases with the stress increase while converging to a single point on $\log t_r$ axis. A point of convergence of LM isostress lines suggests that the operating temperature is sufficiently high that a change in applied stress does not influence the rupture time anymore; indicates the limiting highest temperature beyond that the model is invalid. The point of convergence can be used as an initial guess of the constant, t_a. Third, the initial guess constant, t_a can be used to determine the parameter, *P* at each data point. Fourth, the calculated parameters, *P* is mapped as a function of stress by calibrating the constant, t_a to produce a single "master curve". Thus, the stress-parameter function is a mathematical expression of the master curve such that a temperature invariant parameter can be obtained for a given stress. Fifth, the stress-parameter function and the constant, t_a is plug into LM model to obtain prediction curve.

4.2.2 Family of Models

The simplicity of the Larson-Miller (LM) model made it a favorite choice among creep-rupture analysts. Over time, numerous researchers have developed competing time-temperature parameter

models by conducting creep tests on different materials at different creep conditions and apply different interpolation/extrapolation analysis. Most of these models are a modification, expansion and/or collective representation of the parent LM model. In this study, eight commonly used time-temperature parameter models and an additional four new models are considered for analysis. The mathematical expression of the twelve models is presented in Table 7. It is assumed that the function $f(\sigma,T)$ represents both long-term and short-term creep behavior. Thus long-term creep behavior can be predicted by performing short-term tests at high temperature and extrapolating downwards. All TTP models require the similar framework as of LM model for data fitting, described in section 4.1.

4.2.3 Mirror Models

Often the pattern of the isostress lines on a plot of $\log t_r$ versus temperature (*T* or *1/T*) is used to characterize these models. The isostress lines for the models are shown in Figure 4.3. Comparing the Goldhoff-Sherby (GS) and Manson-Haferd (MH) isostress lines as shown in Figure 4.3c and d, it can be observed that both models have a similar mathematical form, with the difference being that the GS model uses *1/T* while the MH model uses *T* as a variable. This results in the isostress lines of the models mirroring of each other. A similar trend can be observed between the Orr-Sherby-Dorn (OSD) and Manson-Succop (MS) models as shown in Figure 4.3g and h respectively. These similarities can be exploited to form "mirror pairs" (for example GS-MH and OSD-MS) that have a similar mathematical form whose isostress lines are inverse/mirror image due to the temperature variable *T* being inverted. Inspired by these similarities between models, four new models are developed by modifying four existing models (Larson-Miller (LM), Manson-Brown (MB), Chitty-Duval (CD), and Graham-Wallace (GW). A list of the mirror pairs is provided in

Table 8 and the corresponding schematic of the isostress lines are illustrated in Figure 4.3. These models create additional mathematical options to choose from for creep rupture prediction.

Table 8 – List of the "mirror pairs" that have similar mathematical form whose isostress lines are inverse/mirror image due to the temperature variable *T* being inverted

(1)	Larson-Miller	↔	Mod-Manson-Haferd
(2)	Goldhoff-Sherby	↔	Manson-Haferd
(3)	Mo-Goldhoff-Sherby	↔	Manson-Brown
(4)	Orr-Sherby-Dorn	↔	Manson-Succop
(5)	Mod-Graham-Walles	↔	Graham-Walles
(6)	Mod-Chitty-Duval	↔	Chitty-Duval

4.2.4 Isostress lines and the Point of Convergence

The trend of the isostress lines and the point of convergence are important characteristics of time-temperature parameter models. The isostress lines on a $\log(t_r)$ versus *1/T* plot have a positive slope and the isostress lines on a $\log(t_r)$ versus *T* have a negative slope. The models that exhibit a point of convergence and has a positive slop, assume that the higher the operating temperature the lower the effect of stress variation on creep life. In contrast, the models that exhibit a point of convergence and has a negative slope, assume that the higher the operating temperature the higher is the effect of stress variation on creep life. For example, in Figure 4.3a and b, a stress variation of $(\sigma_2 - \sigma_1)$ at temperature T_2 leads to a variation of *a-b* in rupture life, when the temperature is reduced to T_1 for the same stress variation of $(\sigma_2 - \sigma_1)$ the variation of rupture life *c-d* is bigger

in Figure 4.3a and smaller in Figure 4.3b. Further temperature reduction leads to a similar change in rupture life until the isostress lines converge to a point where the variation of stress does not affect the rupture life at all. However, the OSD and MS models do not have a point of convergence due to the assumption that the effect of stress variation is constant at any temperature.

For example, for the MS model, a stress variation has a constant rupture life variation at any temperature, $a - b = c - d$ as depicted in Figure h. Furthermore, a point of convergence can be considered as a limiting criterion for a model such that beyond that point the model may be invalid. For example, the MH model has a point of convergence at $\left(T_a, \log t_a\right)$ as shown in Figure h. At a service temperature less than T_a, the model indicates a physically unrealistic long creep life at high stress when compared to low stress. This suggests that the MH model is invalid for a temperature below T_a. Thus, the optimized T_a constant determines the limiting temperature below which the MH model is invalid as shown in Figure d with a shade region. Similar limiting conditions can be determined for the GS, MGS, MB, GW and MGW models as shown by a gray shaded region in Figure 4.3c-f, and i-j respectively. The GW model exhibits a point of convergence in the high-temperature region at T_a as shown in Figure 4.3k. A temperature greater than T_a will predict physically unrealistic life. This realization is important for extrapolation beyond the experimental data range.

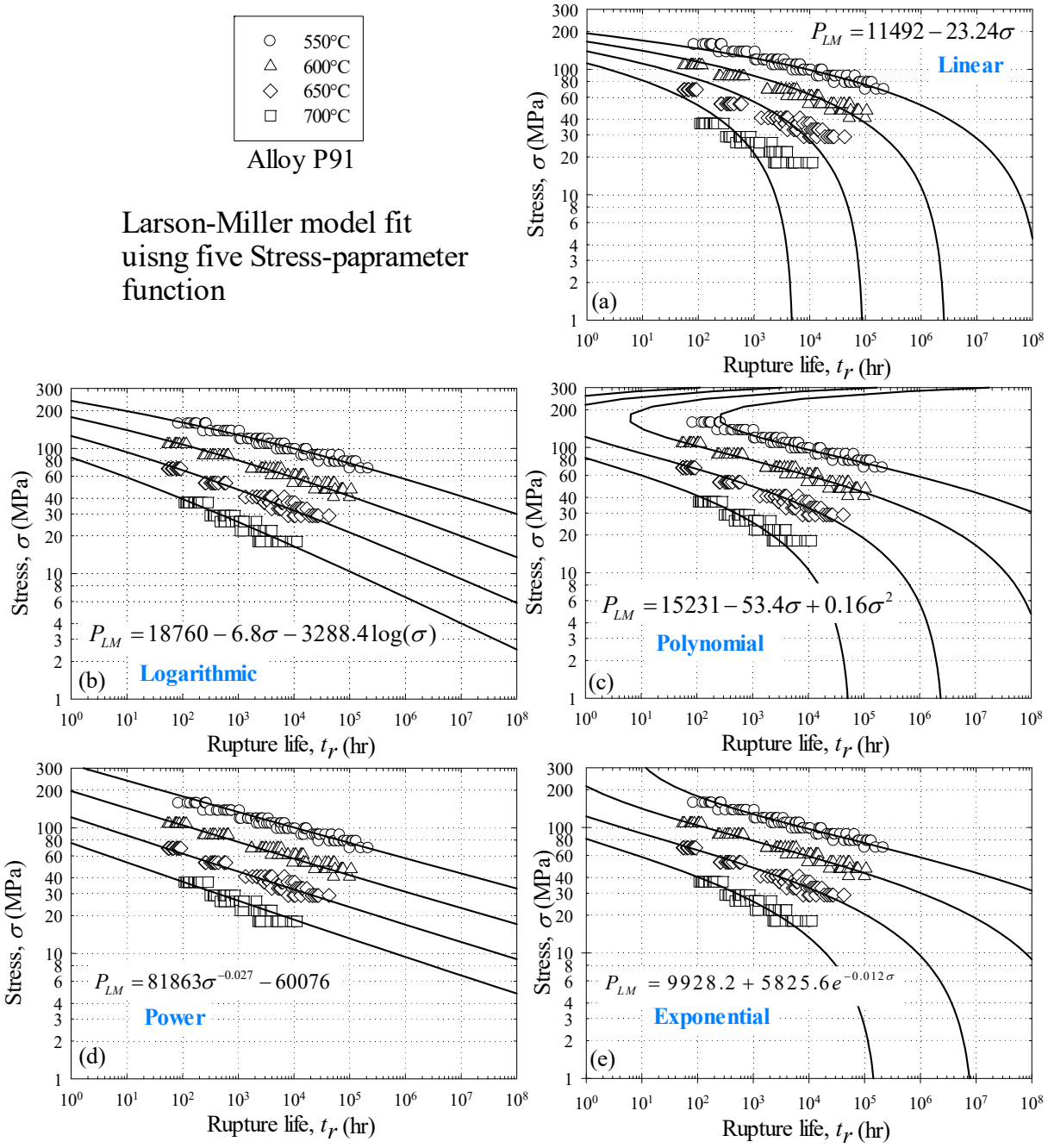

Figure 4.4 – Demonstration of the Larson-Miller model using five stress-parameter functions: (a) linear, (b) logarithm, (c) polynomial, (d) power, and (e) exponential functions

Table 9 – Effect of typical stress-parameter functions during extrapolation on Larson-Miller

Function type	Equation	Prediction type	Inflection? $\frac{dP_i}{d\sigma}=0$
Linear	$a+b\sigma$	High Weakening	NO
Logarithm	$a+b\sigma+c\log(\sigma)$	Stable	NO
Ploy-nominal	$a+b\sigma+c\sigma^2$	Weakening	YES
Power	$a+b\sigma^c$	Stable	NO
Exponential	$a+be^{c\sigma}$	Weakening	YES

4.2.5 Stress-Parameter Functions

Performance of TTP models depends on the selection of the stress-parameter function. A poor selection can lead to inflection points within or beyond the data range resulting in physically unrealistic rupture predictions. Numerous investigators have identified the inflection point issue [58,69,70]. Seruga and colleagues suggested assuming the inflection point stress as the endurance limit stress (like the endurance limit used in stress-life fatigue). Any stress that exceeds the inflection stress will have the same rupture life as the inflection stress. The approach has two drawbacks. First, the endurance limit stress approach has the potential to overpredict rupture life for an inflection in the high-stress region and underpredict rupture life for an inflection in the low-stress region. Second, an extrapolation to long life using short-term data may be impossible.

The stress at which the model exhibits an inflection point can be determined by taking the first derivative of the stress-parameter function with respect to stress and solving for zero as follows

$$\frac{dP_i}{d\sigma}=0 \tag{53}$$

This process can be applied to any model to check for the existing of an inflection and identify the inflection point stress. A simple approach to avoid this issue is to select a function such that [Eq. (53)] does not exist in a physically realistic stress condition. For example, the first derivative of a linear function as listed in Table 9 does not exist. Similarly, for a logarithmic and power functions as listed in Table 9; [Eq. (53)] is only valid at infinite or zero stress respectively. Thus, use of a linear, and/or logarithmic, and/or power function may lead to inflection free prediction. Eno and colleagues have adopted a linear logarithmic function ($P_i = a - b\log(\sigma)$) to avoid inflection issue [72]. In addition to inflection issue, materials exhibiting creep strengthening, weakening, or stable creep rupture behavior can be imitated by proper selection of the stress-parameter function.

An example of the effect of five stress-parameter functions on Larson-Miller model fit extrapolated from 1 hr to 10E8 hrs is illustrated in Figure 4.4 and summarized in Table 9. It is observed that for a linear, logarithmic, and power function' the LM model curves do not exhibit inflection; while differing in extrapolation trajectory as shown in Figure 4.4a, b, and d respectively. A linear function exhibits a high weakening behavior, and the logarithmic and power function exhibit a stable behavior. A subtle difference is noticed between the logarithmic and power function prediction. The logarithmic function exhibits a converging behavior when extrapolating to high stress and a diverging behavior when extrapolated to the low-stress level. The power function exhibits a more consistent behavior compared to logarithmic function. The polynomial and exponential function develop an inflection point in the fit curves as shown in Figure 4.4c and e. The polynomial exhibits within-data inflection at 550°C and beyond-data inflection at 600°C. Using [Eq. (53)], the inflection point stress is obtained at 166.87 MPa. The exponential function exhibits a beyond-data inflection at 550°C. This suggests that the polynomial and exponential

function may perform satisfactorily during interpolation, however, may exhibit inflection when extrapolated to a lower temperature and high-stress condition. Both the polynomial and exponential function exhibit a weakening behavior. A similar analogy can be performed for all TTP models to choose the most suitable function to mimic desired material behavior. In the ASME III and European ECCC codes, it is suggested that a provision for expert-user intervention is required to overcome these issues [68-69].

4.3 METAMODEL

The existing approach to metamodeling time-temperature parameter models is to replace the parameter, P with a "predefined" stress-parameter function, $P = f(\sigma)$. Parameters calculated from experimental data for each model are force fitted to the "predefined" stress-parameter function to test the goodness-of-fit in the process of determining the most suitable model for a given material. The first attempt to develop a time-temperature metamodel dates back to 1953 by Manson and Brown where LMP and MH are a special case. Later, many more attempts are reported. A summary of some generalized models up to the year 1979 is available [71].

In 1999, Holdsworth introduced a metamodel that incorporates the LM, MH, Mod-MH, MRM, and Mod-MRM models as special cases [73]. The Holdsworth metamodel, with a fourth order polynomial as the "predefined" stress-parameter function, is as follows

$$\log(t_r) = \left\{ \sum_{k=0}^{n} \beta_k (\log[\sigma]^k) \right\} (T - T_a) + \beta_5 \qquad (54)$$
$$n = 2, 3, 4$$

where, n indicates the order of the polynomial, and are the coefficients obtained by the least square method.

In 2008, Eno and colleagues introduced a-metamodel that incorporates the LM, MH, OSD, MS, and MRM models as special cases. The Ino metamodel, with a linear log as the "predefined" stress-parameter function, is as follows

$$\log(t_r) = \beta_0 + \beta_1\left(\frac{1}{T}\right) + \beta_2 \log(\sigma) + \beta_3 \log(\sigma)\left(\frac{1}{T}\right)$$
$$\log(t_r) = \beta_0 + \beta_1\left(T\right) + \beta_2 \log(\sigma) + \beta_3 \log(\sigma)\left(T\right) \tag{55}$$

where β_{1-3} are the coefficients obtained by the least square method [72].

In 2011, Seruga introduced another metamodel that incorporates the LM, MH, OSD, and MB models as special cases. The Seruga metamodel, with a second order polynomial as the "predefined" stress-parameter function, is as follows

$$\log(t_r) = (T - T_a.\langle q \rangle)^q (a_0 + a_1 \log(\sigma) + a_2 \log^2(\sigma)) + \log(t_a) T^{q-1} \tag{56}$$

where $\langle q \rangle$ is a conditional coefficient [58]. The value of $\langle q \rangle$ is q for $q > 0$ and zero for $q < 0$. The other coefficients $T_a, \log(t_a), a_0, a_1,$ and a_2 are obtained by the least square method. The Holdsworth, Eno, and Seruga metamodels "predefined" the stress-parameter function. This raises the risk of rejecting the submodels that do not fit the predefined stress-parameter function. An alternative approach is needed.

In this study, a new metamodel is developed without "predefined" the stress-parameter function as follows

$$P_{HS} = \frac{\log(t_r) - \alpha_0 - \alpha_1 T^r}{(T^r - {\alpha_2}^r)^q} \tag{57}$$

where P_{HS} is a general parameter and α_{0-2} are material coefficients. The metamodel alternates between *T* and *1/T* using $r = 1$ and $r = -1$ respectively. The property *q* is an integer. The new

metamodel is the capability of modeling the twelve submodels as special cases using the conditions summarized in Table 7. In this form, simultaneous regression analysis is required to determine the material constants and stress-parameter function, $P_{HS} = f(\sigma)$. More work is required to perform regression analysis; however, the new metamodel is flexible and the risk of submodel rejection due to a poor fit of the stress-parameter function is reduced.

4.4 GUIDELINE TO MODEL SELECTION

Over time numerous investigators have reported critical issues that can affect the model fit and suggested a corrective measure that should be taken into consideration to determine the most suitable physically realistic model for a given material. A collective summary guideline to model selection is presented below:

It is recommended by American Society of Mechanical Engineering (ASME) that an expert user with considerable knowledge of stress-rupture behavior perform this procedure [69]. The following guideline may be followed if the "best" model of the twelve is to be correctly identified.

- *Data pre-processing:* Pre-processing of data may influence the regression analysis. The inclusion of ongoing (and/or discontinued) creep test data, exclusion of outlier data points, and removal of low-stress data points can have an impact on interpolation versus extrapolation ability. The quantity and quality of data play an important role in model accuracy [69]. It is suggested that test data limited to only one temperature should not be used for constant calibration [70]. Data at high stress with very short failure time are usually due to tensile failure rather than creep [71]. Exclusion of high-stress data named "Left censoring" may increase the reliability of the data assessment [72]. Often stress-rupture data from various sources are combined together into a master database, due to experimental environment variability data scatter of two different temperature level may overlap. Precaution may be needed before combining all data sets. The

main objective of pre-assessment is to provide an error-free, characterized dataset for input into the main assessment [73].

- *Procedure:* According to ECCC, a basic collection of TTP models and a state-of-the-art statistical analysis procedure to assess each model against the subject material is required to select the most suitable model [76,78]. Researchers have presented multiple approaches to calibrating material constants. Most commonly used approaches are to perform regression analysis, error minimization, and graphical techniques. It is reported that a graphical approach to calibrating material constant may introduce human bias, a computer program should be used [75].
- *The purpose of Modeling*: The purpose of modeling, i.e., boundary conditions of interest, can have a dramatic impact on the identification of the best model. The requirements for interpolation are less rigorous than those for extrapolation beyond the available experimental data. A common practice is to use higher order polynomial due to its high goodness-of-fit found to be very successful during interpolation, may give physically unrealistic extrapolation [76]. Careful selection of stress-function should be made to obtain reliable prediction.
- *Temperature feasibility*: Some models exhibit a point of convergence: a point in temperature and time where the isostress lines converge. In these models, there exists a dead zone either below or above the convergence temperature, at which the models produce physically unrealistic rupture predictions. The point of convergence must not violate the purpose of modeling; otherwise, a more suitable model should be selected.
- *Stress feasibility*: The best stress-parameter function for a given model may exhibit an inflection point [58,76,78]. This inflection point can create dead zones either below or above the inflection stress where the given model will produce physically unrealistic rupture predictions. The inflection point must not violate the purpose of modeling; otherwise, a more suitable stress-

parameter model must be selected. In cases where no suitable stress-parameter function is available for a given model, the next best model should be selected and evaluated through this same process.

- *Material behavior*: Materials may exhibit strengthening, weakening, or stable creep rupture behavior [74]. A carefully selected stress-parameter function can mimic this behavior. Depending on the purpose of modeling, i.e. boundary conditions of interest, the overall material behavior may or may not be important to prediction.
- *Extrapolation*: For extrapolation, a model should be calibrated to both full and reduced experimental datasets. If the reduced-data predictions are equivalent to those of the full database, the model can be said to have "good" extrapolation ability [78]. According to ECCC guideline, while extrapolating, a random 50% data cull between $t_{r,\max}/10$ and the longest experimental time and a 10% data cull of the lowest stress data should be used to reassess the model for validation [79,80]. 'Weighting data" is another approach to increase the assessment reliability during extrapolation. It is suggested by ASME that for extrapolating to a particular temperature, the heavier weight would be given to the near temperature data [69]. Regardless of the goodness-of-fit, a visual judgment should be made on the physical realism of the model before acceptance [79,81].
- *Post-processing*: The concept of independent checks on the physical realism, goodness of fit, and extrapolation-repeatability: stability of the model equation representing the creep rupture dataset was originally introduced by ECCC [76]. A detail instruction for the post-processing is available in the ECCC post-assessment tests (PAT) section. Finally, after the selection of the model, a safety user instruction describing the advantages, deficiencies, limiting the reliable range of stress and temperature of the model should be reported [78].

4.5 MATLAB CODE

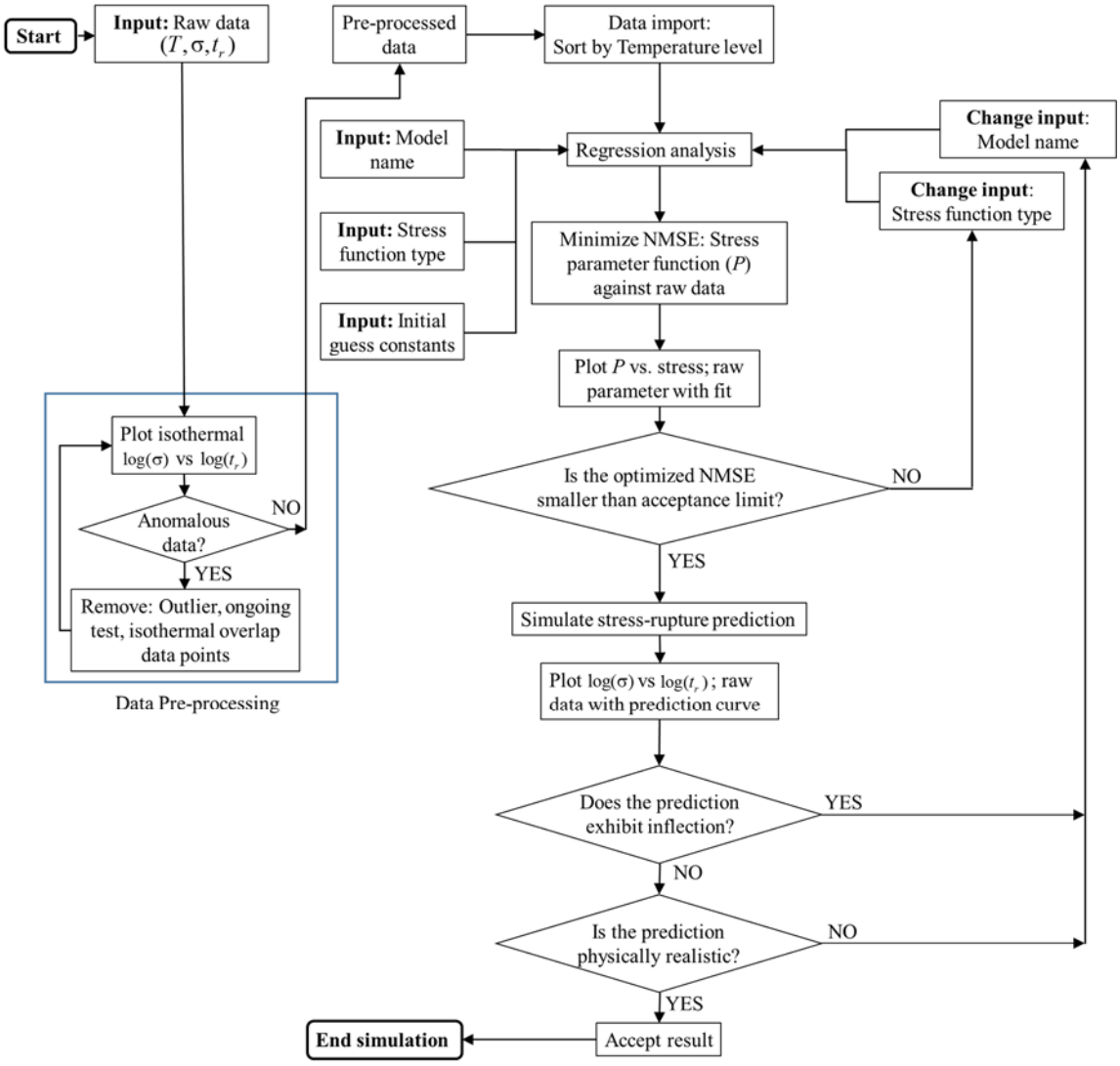

Figure 4.5 – Summary of steps in MATLAB/proposed metamodeling approach

A MATLAB code is developed such that the steps reported in the "guideline to model selection" can be performed easily and accurately. The flow diagram of the MATLAB code is depicted in Figure 4.5. The raw data is feed to the MATLAB software via a .CSV file. First, the raw data is pre-processed to improve the accuracy and reliability of the model fit. A visual

representation of the data facilitates the detection of the outlier, overlapped, and/or unrealistic data. In the following steps, the pre-processed data is considered for the analysis. The use of the metamodel and a single MATLAB code ensures that exact same procedure is followed to assess each model. The model name, stress function type, and initial guess constants are feed for analysis. For a given model, five different types of stress function are analyzed to determine the most suitable stress function and to calibrate the material constants. This calibration process is performed for each model and a Normalized Mean Squared Error (NMSE) is determined by the experimental data. The normalized mean-squared error, NMSE is a statistical measure calculated as

$$NMSE = \frac{1}{n}\sum_{i=1}^{n}[(X_{sim,i} - X_{\exp,i}) / X_{\exp,i}]^2 \tag{58}$$

where n is the total number of data points and, X_{sim}, and X_{exp}, are the simulated, and the experimental data point respectively. In the current case, the experimental data is the average of repeated creep rupture tests at each stress and temperature condition. The model with minimum NMSE producing a physically realistic prediction is the most suitable model for the subject material.

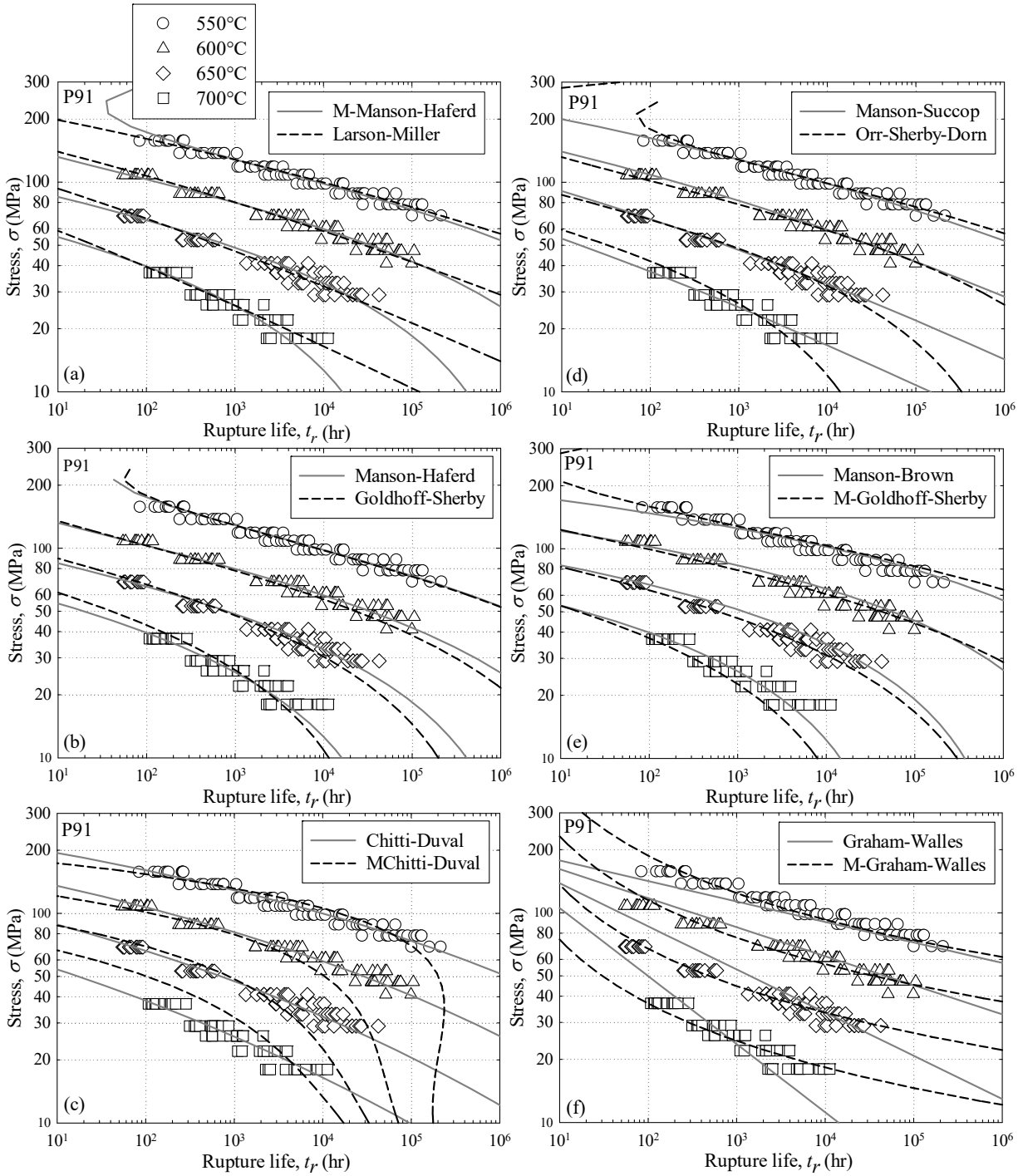

Figure 4.6 – Comparison of models with alloy P91 stress-rupture data

Table 10 – Material constants, stress-parameter functions, inflection status, and overall NMSE of the models

Model	Material Constants	Master curve/Stress-parameter function $P_i = f(\sigma)$ with minimum NMSE	NMSE $P_i = f(\sigma)$ (10^{-3})	Inflection status	Overall NMSE
MMH	$\alpha_0 = 23.87$	$P_{MMH} = 2.6E-7\sigma^2 - 1.2E-4\sigma - 0.03$	0.08	YES	0.80
LM	$\alpha_0 = -16.9$	$P_{LM} = 18760 - 6.81\sigma - 3288.4\log(\sigma)$	0.09	NO	0.91
MH	$\alpha_0 = 23.94$ $\alpha_2 = -0.70$	$P_{MH} = 2.64E-7\sigma^2 - 1.2E-4\sigma - 0.027$	0.08	YES	0.83
GS	$\alpha_0 = 32.0$ $\alpha_2 = 248$	$P_{GS} = -.023\sigma^2 + 10.2\sigma + 11142$	0.007	YES	1.17
MB	$\alpha_0 = 14.0$ $\alpha_2 = 24.9$	$P_{MB} = -2E-5 - 1E-7\sigma - 1.3E-9\log(\sigma)$	0.84	NO	1.61
MGS	$\alpha_0 = 913.5$ $\alpha_2 = 7.8$	$P_{MGS} = 0.009\sigma^2 - 4.7\sigma - 56652$	6E-5	YES	3.49
MS	$\alpha_1 = -0.033$	$P_{MS} = 33.14 - 0.015\sigma - 4.8\log(\sigma)$	0.064	NO	0.87
OSD	$\alpha_1 = 12500$	$P_{OSD} = 1.8E-4\sigma^2 - 0.07\sigma - 12.96$	0.12	YES	0.96
GW	$\alpha_2 = 1005$ $q = 3$	$P_{GW} = -4.7E-5 + 4.7E-5\sigma^{0.001}$	11.4	NO	1.73
MGW	$\alpha_2 = 900$	$P_{MGW} = 7E8\sigma^{-0.98} + 9999$	9.50	NO	3.21

	$q=2$				
CD	$\alpha_1 = f(\sigma)$	$P_{CD} = -23.4 - 0.019\sigma - 0.8\log(\sigma)$; $\alpha_1 = -0.02\sigma^{0.1}$	0.064	NO	0.81
MCD	$\alpha_1 = f(\sigma)$	$P_{MCD} = -5.98 - 0.2\sigma - 3.4\log(\sigma)$; $\alpha_1 = 477.9\sigma^{0.734}$	0.70	YES	2.23

4.6 RESULTS AND DISCUSSION

The model selection guidelines are implemented to calibrate material constants for each of the four materials. The MATLAB code is applied to the stress-rupture data to assess the models and to find the corresponding suitable stress-parameter function. Pre-processing of the raw data is performed. Normalized Mean Square Error (NMSE) of the stress function as well as of rupture prediction is considered along with the visual physical realism to determine the most suitable model. A detail step-by-step explanation is provided for alloy P91. A secondary validation is performed against the stress-rupture data of alloy 304 SS, 316 SS, and Hastelloy X; only the final results are reported.

4.6.1 Detailed Analysis of Alloy P91

The metamodel conditions listed in Table 7 (7^{th} column) are applied to the general model [Eq. (57)] to find the material constants and stress-parameter functions for each model as listed in Table 10. Simultaneous regression analysis is performed on experimental data for alloy P91 to determine the material constants and stress-parameter functions.

The material constants of each model are determined by identifying the stress-parameter function, $P_{HS} = f(\sigma)$ that produces a minimum NMSE for the given model. A second order polynomial

produces a minimum NMSE value for five models; MMH, MH, GS, MGS, and OSD as listed in Table 10. A common logarithm produces a minimum NMSE value for five models; LM, MB, MS, CD, and MCD. A power function produces a minimum NMSE value for the GW and MGW models. It should be noted that using a "predefined" stress-parameter function, such as a second-order polynomial, would lead to the LM, MB, MS, GW, MGW, CD, and MCD models producing a poor fit to the experimental data. These statistics will change to a different material. Thus, the new metamodel approach (without a "predefined" stress-parameter function) will always produce a superior fit of the submodels to experimental data when compared to conventional metamodels (with "predefined" stress temperature functions).

Taking the optimized material properties and stress-parameter functions listed in Table 10, the twelve submodels are grouped into mirror pairs and compared against the experimental data of alloy P91 at four isotherms (550, 600, 650, and 700°C) as shown in Figure 4.6a-f.

The inflection status of the models is listed in Table 10. For alloy P91, it is observed that models with the polynomial stress function are prone to produce an inflection point when extrapolated beyond the experimental data.

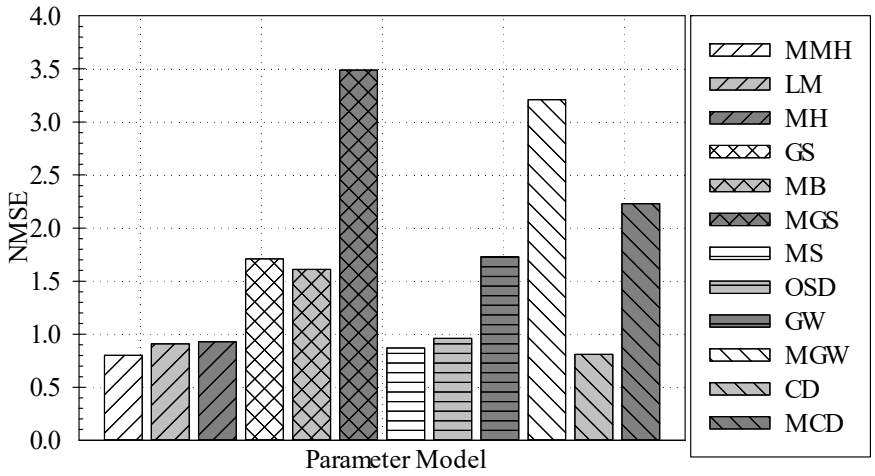

Figure 4.7 – Comparison of the cumulative creep rupture NMSE of the models

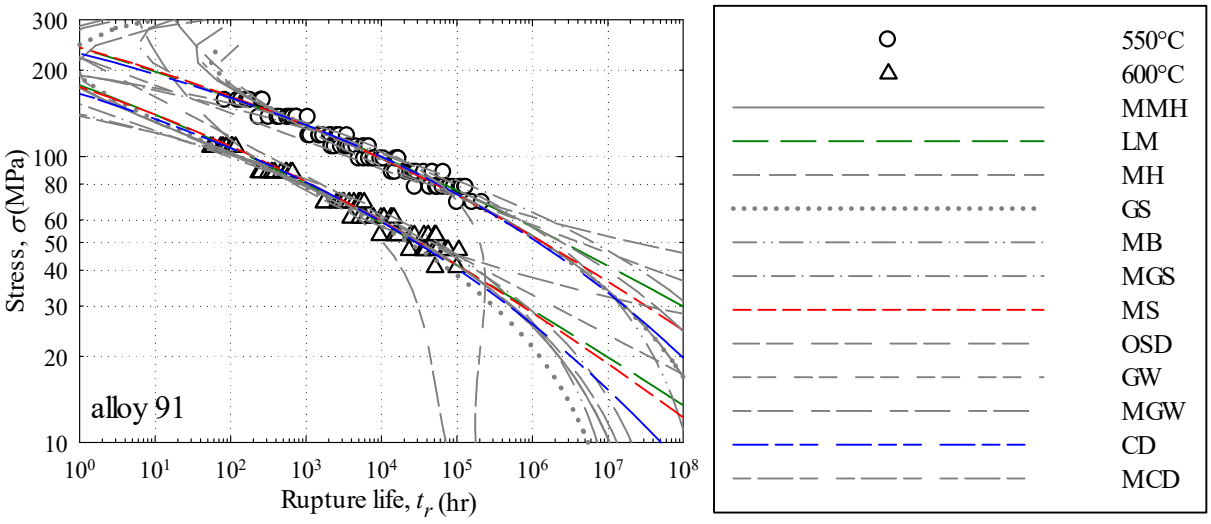

Figure 4.8 – Rupture prediction of the models at 550 and 600°C

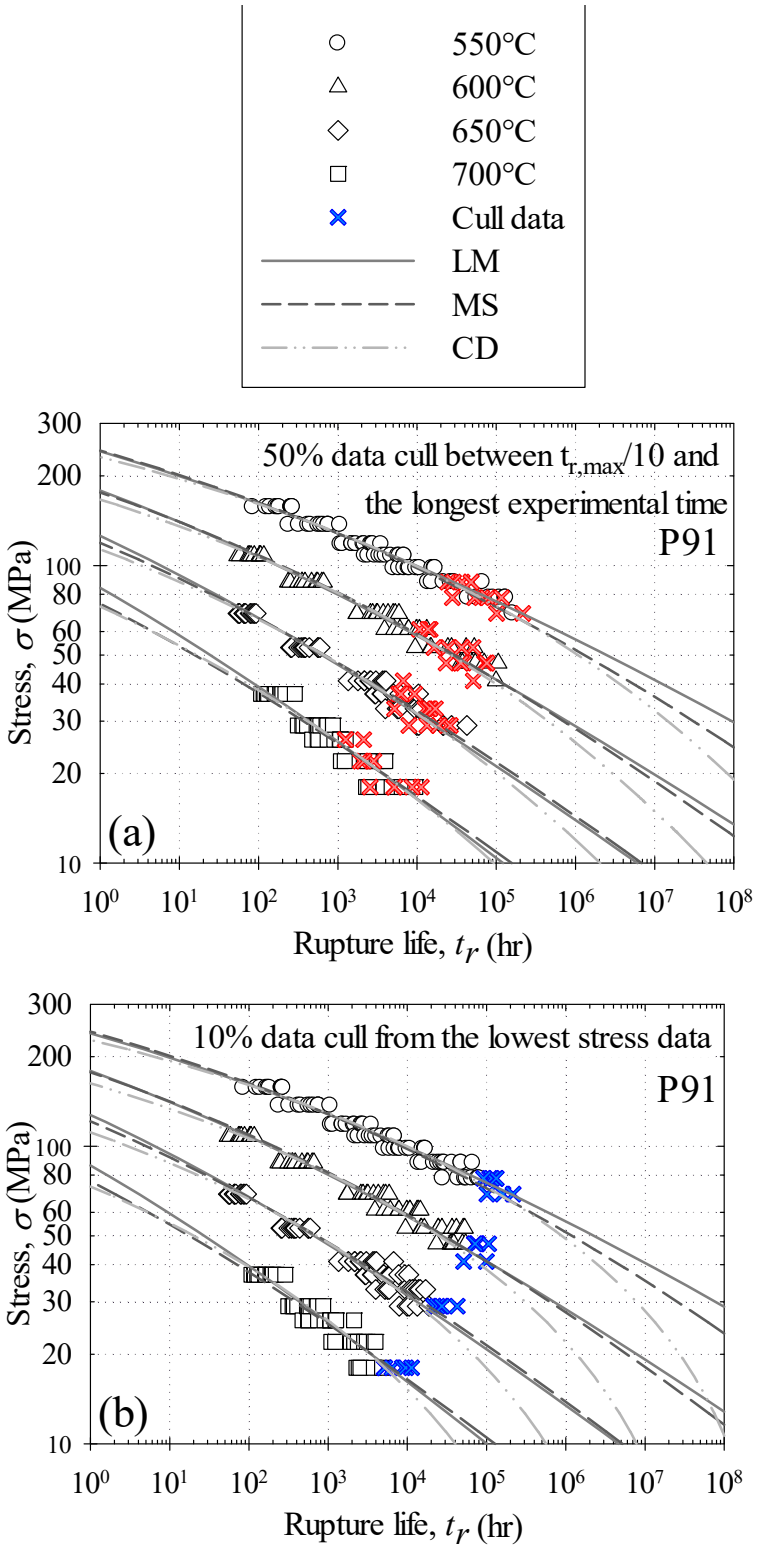

Figure 4.9 – Rupture prediction of LM, MS, and CD against (a) 50% data cull between $t_{r,\max}/10$ and the longest time and (b) 10% data cull from the lowest stress data

Model performance is quantitatively measured using the Normalized Mean Square Error (NMSE) as shown in Figure 4.7. An NMSE value of zero indicates that the experimental data and model are identical. A large NMSE value indicates a poor fit. It is observed that MMH with lowest NMSE exhibits inflection. Inflections should be avoided in stress-rupture curves. The CD, MS, and LM models do not exhibit inflection and produce the lowest NMSE at 0.81, 0.87 and 0.91 respectively. The NMSE of CD, MS, and LM models are almost the same suggesting that any of these three models can be selected for alloy P91.

Further analysis can be performed by plotting the twelve models on the same plot as shown in Figure 4.8. For simplicity, only 550°C and 600°C data and models are plotted. It is observed that among the CD, MS, and LM model; the CD produce the most conservative extrapolation, the MS exhibits a stable behavior and the LM conforms the upper bound. Depending on the sensitivity of the design components and required safety factor, the most conservative (CD), stable (MS), or upper bound model (LM) may be selected. This problem illustrates the uncertainty of creep rupture predictions when extrapolating with time-temperature parameter models. There is a need for accelerated creep tests to provide the long-term creep data needed to calibrate time-temperature parameter models. It is theorized at a creep endurance limit stress could be identified using accelerate creep tests. Further work is needed to improve the TTP models by incorporating the deformation mechanisms and metallurgical instabilities due to aging.

An ECCC recommended check on extrapolation assessment (reported in guideline section: Extrapolation) is performed. The LM, MS, and CD models are recalibrated against two sets of culled data; (a) a random 50% data cull between $t_{r,\max}/10$ and the longest experimental time, and (b) a 10% data cull of the lowest stress data. The LM, MS, and CD model performance (extrapolated to 10E8 hours) in fitting the culled data are illustrated in Figure 4.9. It is observed

that the LM, MS, and the CD models exhibit the similar trend observed in Figure 4.6 (no data cull) when fitting against the 50% cull data as shown in Figure 4.9a. The LM, MS, and CD have the NMSE of 1.02, 1.27, and 1.30 respectively. However, when the models have fit against 10% cull data the CD model shifts to a high weakening behavior as shown in Figure 4.9b. The LM and MS model behavior remains unchanged.

Finally, a required limiting reliable range of stress and temperature of the models is determined. The LM and MS model uses an inflection free logarithmic stress parameter function suggesting that both models is valid for any stress level (see Stress-Parameter Function section). However, it is observed that the LM and MS model may not be reliable at every temperature level. The limiting highest temperature for a given stress level can be determined by plugging the parameter for a given stress level, material constants into the model equation listed in Table 10. For example, for a given stress level of 100 MPa, the LM parameter is $P_{LMP} = 8719$ (from Table 10). Pugging the material constants and the parameter the LM model (from Table 7) has the following form

$$8719 = T(\log(t_r) - 16.9) \tag{59}$$

Rearranging [Eq. (59)] and plugging $\log(t_r) = 0$ (assuming, short time failure (less than 1 hour) are more likely due to tensile deformation than creep [15]) the limiting highest temperature of $T = 680.6^{\circ}C$ is obtained. This suggests that at 100 MPa stress level the LM model is reliable up to 680.6°C. Similarly, for MS model the reliable highest temperature level for 100 MPa is 667.9°C. The maximum limiting temperature can be determined at any stress level for any model by following the above-mentioned procedure. It can be concluded that both the LM and MS model is suitable for the alloy P91 prediction.

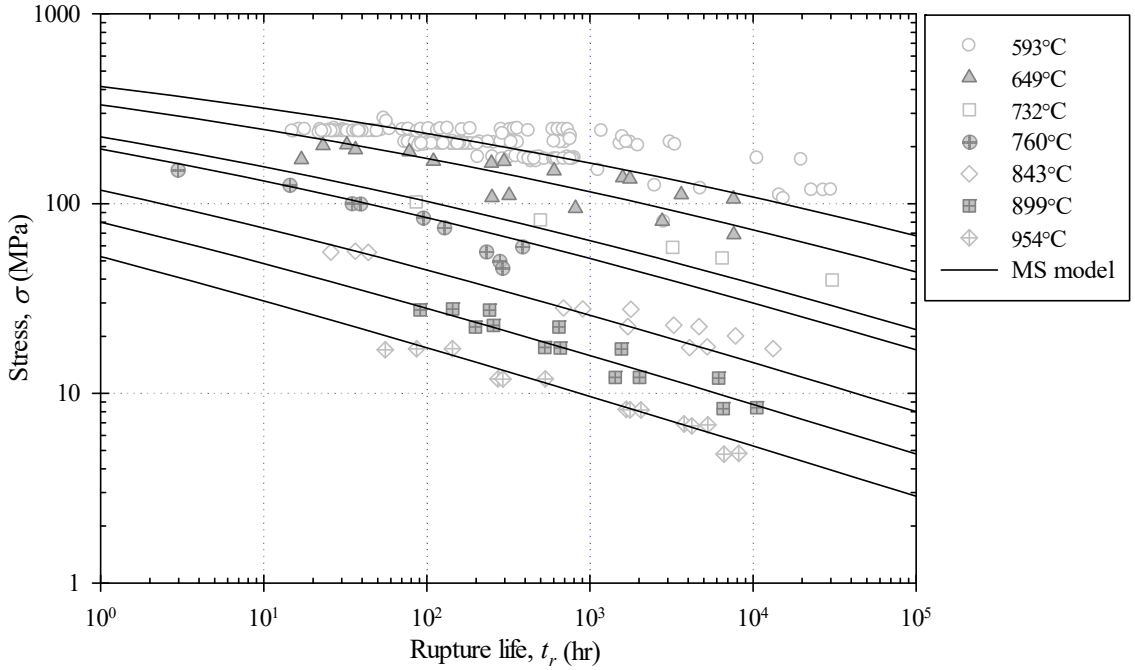

Figure 4.10 – MS model fit for alloy 304 SS stress rupture data

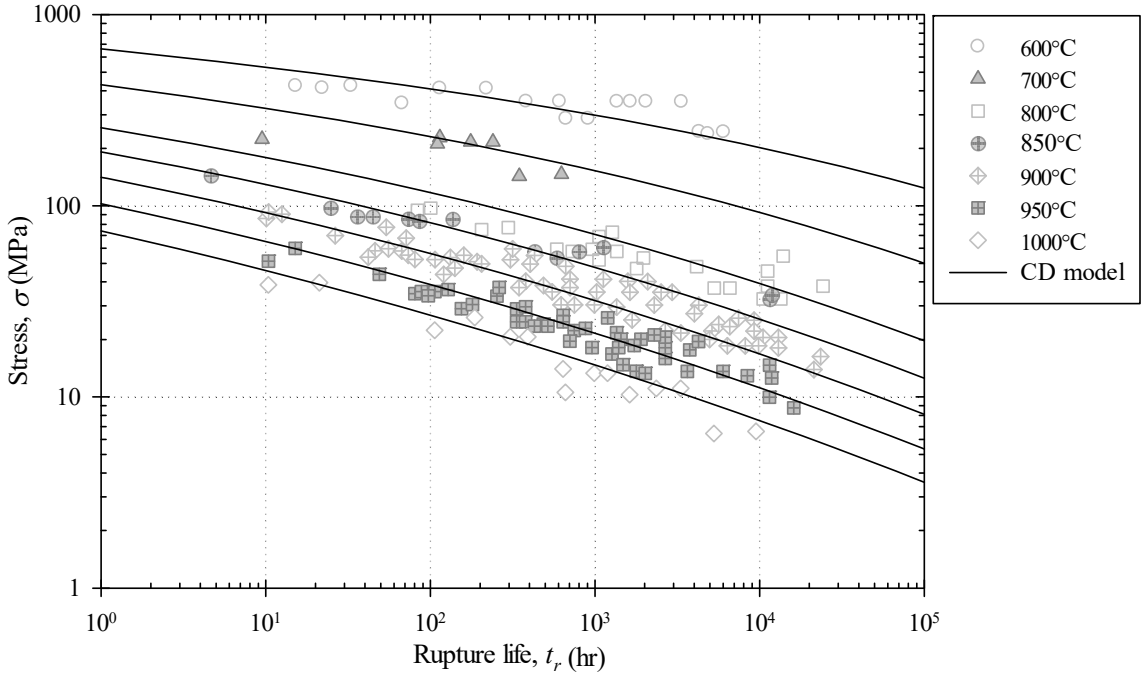

Figure 4.11 – CD model fit for Hastelloy X stress rupture data

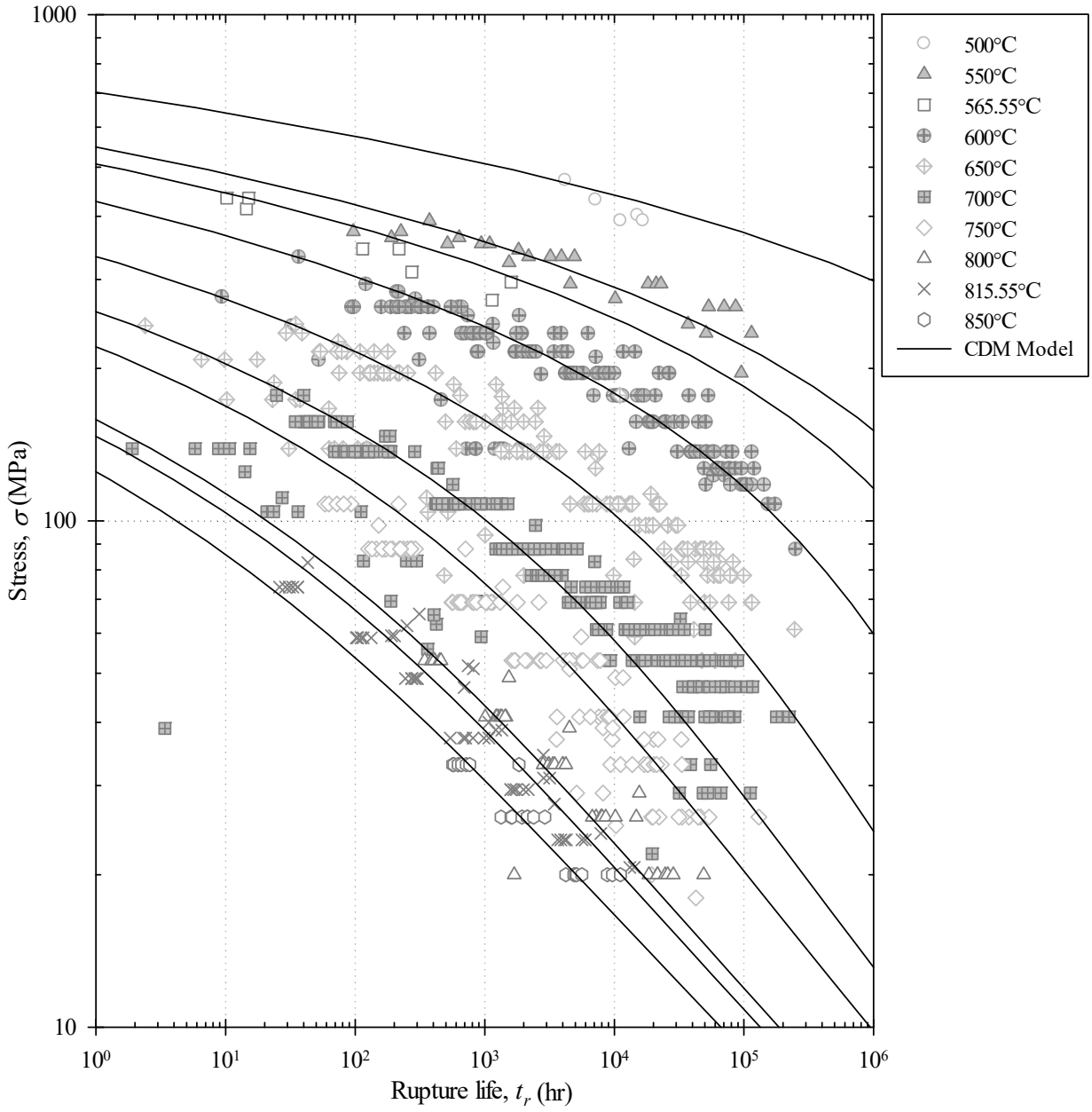

Figure 4.12 – MCD model fit for alloy 316 SS stress-rupture data

4.6.2 Secondary Analysis of 304SS, 316SS, and Hastelloy X

A similar analysis is performed for alloy 304 SS, 316 SS, and Hastelloy X. It is observed that for alloy 304 SS the MMH and MS model has the lowest NMSE of 8.54 and 8.89 with inflection free prediction as listed in Table 11. The MS is more stable than MMH when extrapolated to 10E6 hours. The prediction curves of the MMH and MS model are plotted against experimental data to check for physical realism. It is observed that both models agree with the experimental data during interpolation but follows a different trajectory while extrapolating to 10E6 hours as shown in Figure 4.10. The MS model exhibits stable extrapolation behavior while the MMH model exhibits a comparatively conservative weakening behavior. This suggests that during interpolation any of the MMH or MS models can be selected while for extrapolation the conservative MMH model may be selected.

The models with the lowest NMSE is for 316 SS and Hastelloy X is found to be different than that of 304 SS. It is observed that the CD and MMH has the lowest NMSE for Hastelloy X and MH and MCD have the lowest NMSE for 316 MS as listed in Figure 4.11 and Figure 4.12 respectively. For 316 SS, the MH has the lowest NMSE of 1.88, but the second lowest model MCD with NMSE of 2.38 exhibit more physically realistic prediction suggesting the MCD model is more suitable for 316 SS. In the case of Hastelloy X, CD and MMH model exhibit similar prediction thus any of the two models are suitable for Hastelloy X. A summary of the analysis is listed in Table 11.

Table 11 – Summary of the TTP model selection analysis for 304 SS, 316 SS, and Hastelloy X

Model	Material Constants	Master curve/Stress-parameter function $P_i = f(\sigma)$ with minimum NMSE	NMSE $P_i = f(\sigma)$ (10^{-3})	Inflection status	Overall NMSE
		304 SS			
MMH	$\alpha_0 = 12.96$	$P_{MMH} = -0.007 - 1.8E-5\sigma - 0.003\log(\sigma)$	2.00	NO	8.540
MS	$\alpha_1 = -0.015$	$P_{MS} = 21.26 - 0.006\sigma - 3.73\log(\sigma)$	1.20	NO	8.89
		316 SS			
MH	$\alpha_0 = 16.6$, $\alpha_2 = -0.15$	$P_{MH} = -0.0161 - 2.78E-5\sigma$	1.20	NO	1.880
MCD	$\alpha_1 = f(\sigma)$	$P_{MCD} = -4.33 + 0.02\sigma + 6.46\log(\sigma)$; $\alpha_1 = 3893\sigma^{0.19}$	0.89	NO	2.38
		Hastelloy X			
CD	$\alpha_1 = f(\sigma)$	$P_{CD} = -15 + 0.005\sigma$; $\alpha_1 = -0.0085\sigma^{-0.12}$	0.53	NO	1.28
MMH	$\alpha_0 = 14.68$	$P_{MMH} = -0.008 - 1.2E-5\sigma - 0.003\log(\sigma)$	0.96	NO	1.380

4.7 SUMMARY

In this study, metamodeling is applied to twelve time-temperature parameter models: eight from literature and four new models derived by exploiting similarities between the models.

I. Six pairs of “mirror models” are identified that: (a) have similar mathematical form, (b) the isostress lines are inverse/mirror image of one another, (c) the temperature variable T is inverse of one another;

II. A metamodel is developed to simplify the constant determination process.

III. A guideline is provided for easy application of the metamodel. A provision for expert-user intervention is required to produce physically realistic, accurate creep prediction.

IV. A systematic MATLAB code is developed that facilities easy application of the guidelines. (1) calculate the parameter and determine the most suitable stress-parameter function; (2) calibrate material constants; (3) report the normalized mean square error (NMSE) of each model; and (4) recommend the most physically realistic TTP model for given experimental data. Model calibration to large data set became easier.

V. The MATLAB code is validated against alloy P91 stress-rupture data. A secondary validation is performed against alloy 304 SS< 316 SS, and Hastelloy X data.

Chapter 5: Adaptive Creep Modeling: Creep Deformation

ABSTRACT

Metamodeling is an approach where the general framework, rules, and constraints of a well-poised problem are exploited. These constraints enable the manipulation of existing models to create new "meta" models. Metamodeling is applied to the problem of creep deformation, damage, and rupture. Model transformations between the Theta projection, MPC Omega, and Sin-hyperbolic constitutive models are derived to (i) facilitate conversion of one models' material constants to the constants of the other two, (ii) allow instant and simultaneous calibration of the models, and (iii) enable the derivation of combinational/metamodels with unique aspects. The constitutive models are calibrated to two isotherms of Hastelloy X creep test data. A statistical analysis involving acceptability plots, conservatism plots, and the normalized mean-squared error (NMSE) are employed to evaluate the combinational and classic models with respect to experimental data.

5.1 INTRODUCTION

Constitutive, damage, and life prediction models for creep can be mathematically described as time-temperature-stress functions; calibrated for a given material. These models tend to follow the same general framework, rules, and constraints such that they can be mathematically exploited to create "metamodels". These "metamodels" are combinational models, derived from equating and rearranging the functional relationships in the selected base models. The combinational/metamodels can exhibit unique attributes that offer the potential for superior prediction-ability. During the metamodeling process, model transformation identities can be derived that allow the instant transformation of the material constants of one model into another.

In this work, metamodeling is applied to the Theta projection, MPC Omega, and Sin-hyperbolic models.

The Theta projection and MPC Omega models are single differential equation models consisting of the creep strain rate [82-84]. The Theta and Omega model assume creep strain rate is an exponential function of time $\dot{\varepsilon} \propto \exp(t)$ and creep strain $\dot{\varepsilon} \propto \exp(\varepsilon)$ respectively. The Sin-hyperbolic (Sinh) model is a coupled differential equation model consisting of creep strain rate coupled to damage evolution [85]. The Sin-hyperbolic (Sinh) model assumes creep strain rate is an exponential function of damage $\dot{\varepsilon} \propto \exp(\omega)$. Several investigators have reported the relative performance of Theta, Omega, and Sinh models for various creep-susceptible materials [83 ,61, 128]. The Theta model can predict three creep regimes (primary, secondary, tertiary) but the rupture life depends on creep ductility. Uncertainty analysis of creep ductility is required in order to avoid poor predictions [87]. An exponential rise of the creep strain rate at the last stage of creep leads to a poor prediction for the Theta model. The Theta model does not model damage evolution. Attempts to incorporate a damage rate proportional to the creep strain rate have been performed; however, in those attempts, damage does not evolve from zero to unity [87, 90]. As a result, non-coupled linear damage rules are typically applied for damage prediction. This is also true, for the Omega model. The Omega model has the simplest form of the creep strain rate yet is capable of modeling the secondary and tertiary creep regimes [83,61]. The Sinh model has the ability to predict the minimum creep strain rate, creep deformation (secondary and tertiary), non-linear damage evolution, and life prediction using a set of coupled differential equations; however, the Sinh model is complex, with a comparatively high number of material constants [61, 128]. It is evident that each model has distinct advantages and limitations. Using metamodeling, model transformations (between the models) can be derived and implemented to create

combinational/metamodels that combine the advantages and mitigate the limitations of the original models.

In this study, the model transformation between Theta-Omega, Omega-Sinh, and Sinh-Theta models are derived. A model transformation identity will be derived for each of the above-mentioned model-combinations by equating the creep strain rate equations. Analytical approaches to determine the identities from experimental data will be derived and graphically illustrated. Six new combinational/metamodels will be derived using the model transformations. A comparison of the six new models with the experimental data for Hastelloy X will be presented. Finally, the original and combinational models will be analyzed to determine which models statistically acceptable predictions and conservatism when compared to experimental data.

5.2 CALIBRATED MATERIAL CONSTANTS

5.2.1 Theta model

The calibrated Theta constants for Hastelloy X are listed in Table 12.

Table 12 – Theta model constants for Hastelloy X

Temperature, T (°F)	Stress, σ (ksi)	θ_3 (10^{-2})	θ_4 (hr^{-1})	Avg. creep ductility, ε_r
1200	33.5	8.8	1.25E-3	0.4572
	36.5	5.1	3.40E-3	0.6663
1600	6.30	4.1	3.30E-3	0.2930
	7.30	5.5	5.50E-3	0.2714

5.2.2 Omega Model

The calibrated Omega constants for Hastelloy X are listed in Table 13.

Table 13 – Omega model constants for Hastelloy X

Temperature, T ($°F$)	Stress, σ (ksi)	Ω	$\dot{\varepsilon}_0$ (hr^{-1})
1200	33.5	6.340	1.13E-4
	36.5	4.950	2.58E-4
1600	6.30	9.550	1.61E-4
	7.30	8.842	3.16E-4

5.2.3 Sin-Hyperbolic model

The Sinh constants calibrated for Hastelloy X are listed in Table 14.

Table 14 – Sinh model constant for Hastelloy X

Temperature, T (°F)	Stress, σ (ksi)	A (hr^{-1})	σ_s (ksi)	ϕ	λ	M ($10^{-4}hr^{-1}$)	σ_t (ksi)	χ
1200	33.5	5.54E-10	3.16	3.30	3.94	1.51	25.34	3
	36.5			2.30	3.15			
1600	6.30	7.45E-8	1.67	2.10	3.27	77.0	11.00	3
	7.30			1.25	2.90			

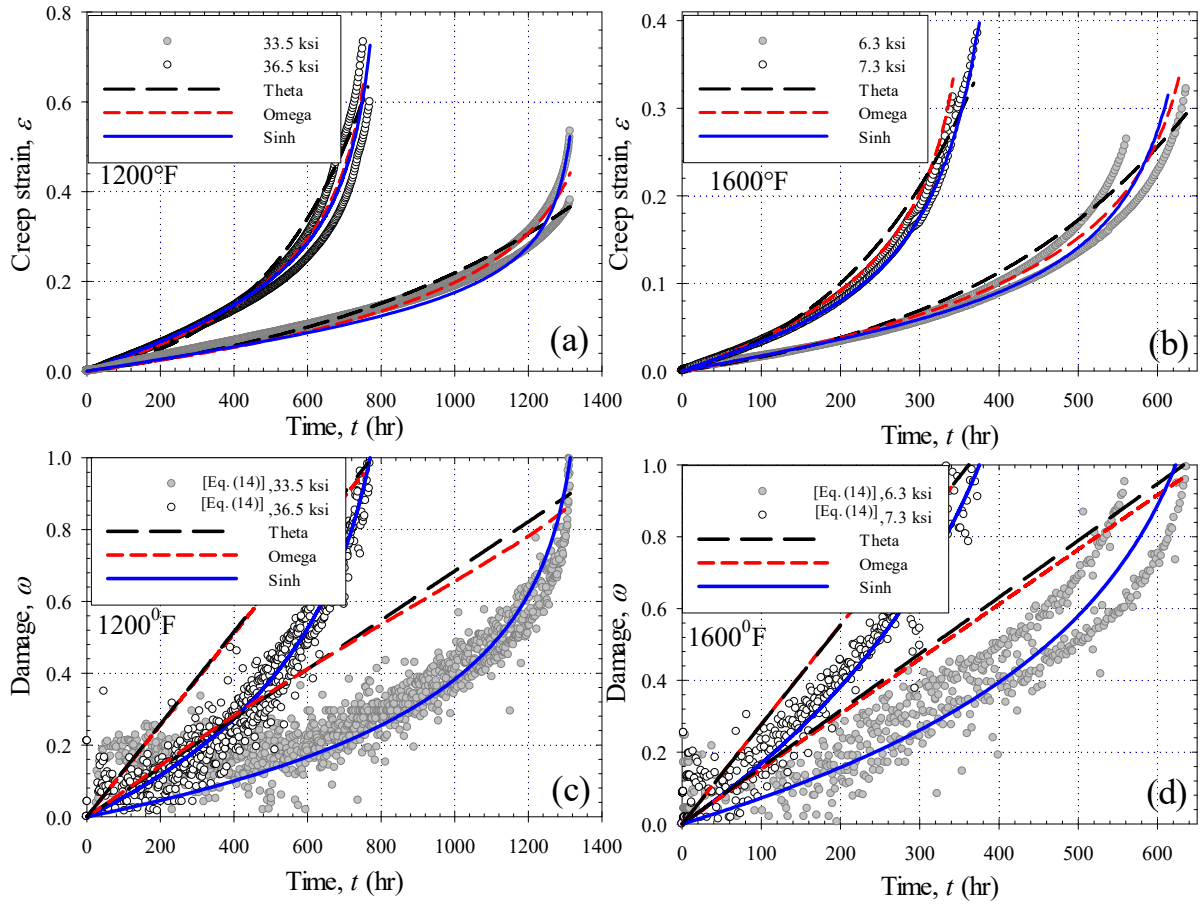

Figure 5.1 – Comparison of Theta, Omega, and Sinh models (a-b) creep deformation and (c-d) damage at 1200°F and 1600°F respectively

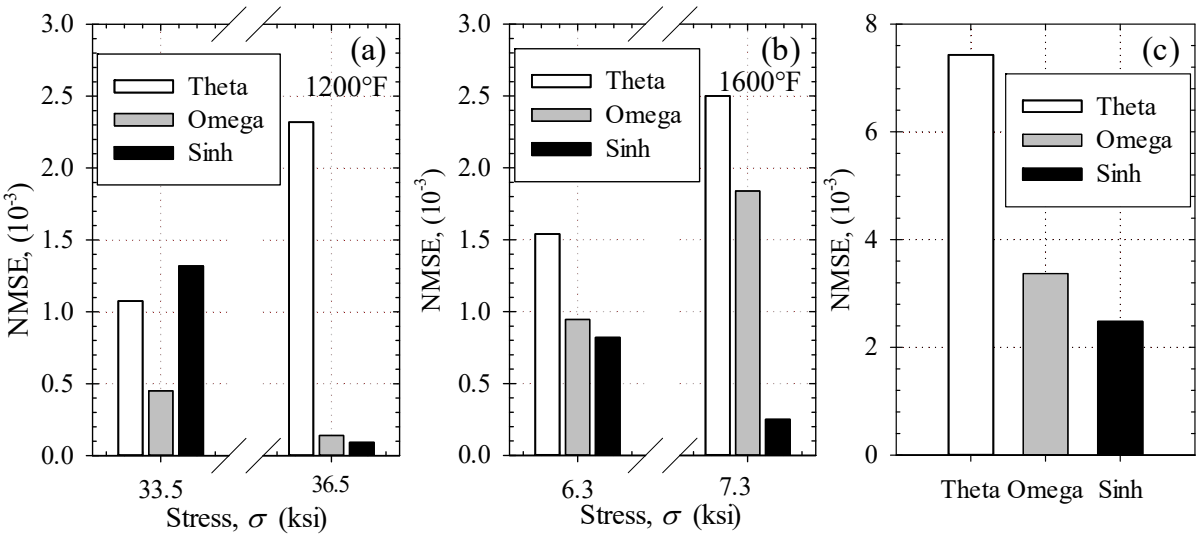

Figure 5.2 – Creep deformation NMSE of Theta, Omega, and Sinh models (a) 1200°F (b) 1600°F and (c) cumulative

5.4 Comparison of Theta, Omega, and Sinh Models

A comparison of creep deformation and damage of Theta, Omega, and Sinh models when fit to Hastelloy X creep data is shown in Figure 5.1. The creep deformation of all three constitutive models is identical at the beginning of life and diverges over time as shown in Figure 5.1a-b. The damage curves of the Omega and Sinh models are shown in Figure 5.1c-d. The omega damage [Eq. (4)] and Theta damage [Eq. (14)] follow an unrealistic linear trajectory with time [83]. Damage should follow a nonlinear accelerating trajectory. The Sinh damage [Eq. (38)] produces a more realistic nonlinear damage curve that goes from zero to unity as shown in Figure 5.1c-d. The Sinh damage fits the Sinh analytical damage [Eq. (34)] calculated from experimental data.

The quality of the creep deformation predict of each model is quantified using Normalized mean-squared error, NMSE as shown in Figure 5.2. The normalized mean-squared error, NMSE is a statistical measure calculated as

$$NMSE = \frac{1}{n}\sum_{i=1}^{n}[(X_{sim,i} - X_{\exp,i}) / X_{\max}]^2 \tag{60}$$

where n is the total number of data points and, X_{sim}, $X_{\exp}$, $X_{\max}$ are the simulated, experimental, and the maximum experimental data point respectively. In the current case, the experimental data is the average of the repeated creep deformation curves. An NMSE value of zero indicates that the experimental data and model are identical and a large value indicates a poor fit. Overall, Theta produced the highest cumulative NMSE of 7.43E-3 and Sinh produced the lowest cumulative NMSE 2.48E-3, followed closely by Omega at 3.37E-3. It is observed that the NMSE of Theta increases from low to high stress, the Sinh model displays the opposite trend, and Omega behavior is mixed. These trends are due to the constitutive equations. The Theta model assumes that creep strain is proportional to the exponent of time. At low stress, this function leads to an accelerated creep strain rate near the end of life. This contradicts experimental data that shows at low stress an accelerating creep strain rate will not occur; therefore, an attempt to fit low-stress data using the Theta model leads to a poor fit. The Omega and Sinh model assume that creep strain is proportional to the exponent of creep strain and damage respectively. Both creep strain and damage are of a low numeric value when compared to time $(t > \varepsilon > \omega)$. The accelerating creep strain rate can be better controlled.

To apply the Theta, Omega, and Sinh models for interpolation or extrapolation it is necessary to define the model's constants as a function. The Theta and Omega model constants are a function of stress and temperature. The Sinh model constants are a function of temperature only.

5.5 MODEL TRANSFORMATIONS

Metamodeling is the analysis, construction, and development of rules and constraints to modeling a pre-defined problem. In the case of creep, the variables of creep deformation, damage, and life

each have rules and constraints that must be enforced. By exploiting these relationships, model transformation identities can be derived that enable the transformation of one model into another.

5.6 THETA-OMEGA IDENTITY

The Theta-Omega identity is derived as follows. Equating the creep strain rate of the Theta and Omega models [Eq. (10) and (4)] gives

$$\dot{\varepsilon}_{Theta} = \dot{\varepsilon}_{Omega} \tag{61}$$

$$\theta_3\theta_4 \exp(\theta_4 t) = \dot{\varepsilon}_0 \exp(\Omega\varepsilon) \tag{62}$$

Rearranging [Eq. (62)] and taking the natural logarithm of both sides gives

$$\ln\left(\frac{\dot{\varepsilon}_0}{\theta_3\theta_4}\right) = \theta_4 t - \Omega\varepsilon \tag{63}$$

Introducing a unit-less Theta-Omega Identity, $I_{\theta\Omega}$, [Eq. (63)] becomes

$$I_{\theta\Omega} = \left(\dot{\varepsilon}_0 / \theta_3\theta_4\right) \tag{64}$$

$$\varepsilon = (\theta_4 / \Omega)t - \ln\left(I_{\theta\Omega}\right) / \Omega \tag{65}$$

where $0 \le I_{\theta\Omega} \le 1$. The above [Eq. (64) and (65)] will be exploited to determine Theta constants given Omega constants and vice-versa.

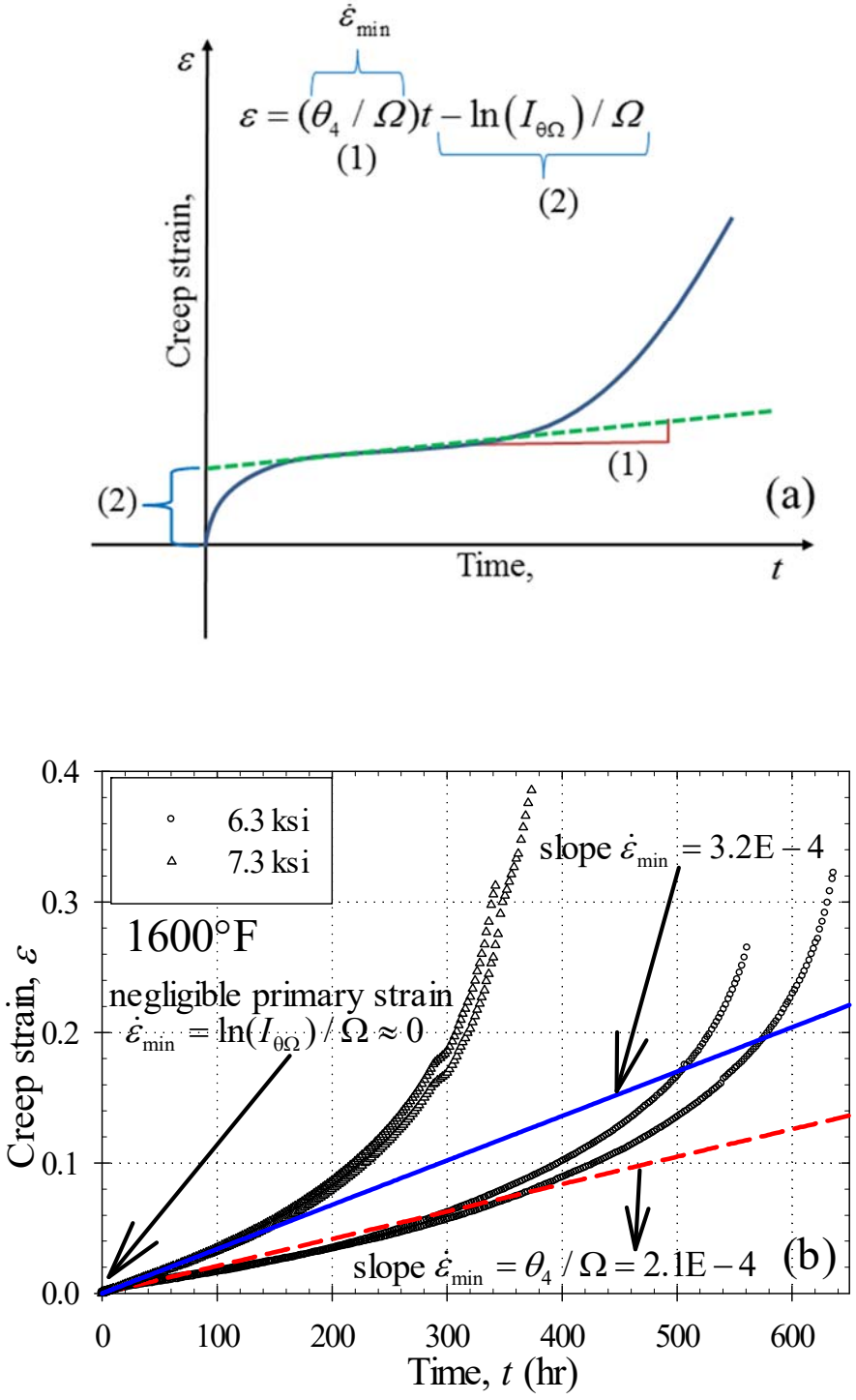

Figure 5.3 – Theta-Omega transformation (a) graphical approach (b) Hastelloy X at 1600°F

5.6.1 Constant Determination

Given the Theta constants θ_3 and θ_4, the Omega constants $\dot{\varepsilon}_0$ and Ω can be found using the graphical approach illustrated in Figure 5.3a. An example transformation curve for Hastelloy X at 1600°F is shown in Figure 5.3b. The creep strain ε is plotted with respect to time *t*. The transformation [Eq. (65)], can be rewritten as

$$\begin{aligned} &\varepsilon = \dot{\varepsilon}_{\min} t + \varepsilon_{pr} \\ &\dot{\varepsilon}_{\min} = (\theta_4 / \Omega), \quad \varepsilon_{pr} = -\ln\left(I_{\theta\Omega}\right) / \Omega \end{aligned} \tag{66}$$

where $\dot{\varepsilon}_{\min}$ is the minimum creep strain rate (during the secondary creep regime) and ε_{pr} is the accumulated primary creep strain. The Ω constant is obtained by dividing $\dot{\varepsilon}_{\min}$ by θ_4. In experimental data, during the secondary creep regime, the $\dot{\varepsilon}_{\min}$ fluctuates. This can make it difficult to obtain an accurate Ω value. This can be mitigated by determining the maximum and minimum $\dot{\varepsilon}_{\min}$ found in the secondary creep regime and profiling between these two numbers until a realistic Ω is obtain. The $\dot{\varepsilon}_0$ constant is obtained by measuring the Y-intercept, solving for $I_{\theta\Omega}$, and then rearranging $I_{\theta\Omega}$ [Eq. (64)] to solve for $\dot{\varepsilon}_0$. In the cases where no primary creep strain is observed, $I_{\theta\Omega}$ resolves to unity. The reverse of this constant determination process can be applied to find the Theta constants given Omega constants.

Using the graphical approach for the Theta-Omega transformation depicted in Figure a, on the collected Hastelloy X data, the Theta constants in Table 12 are used to find transformed Omega constants and the Omega constants in Table 13 are used to find transformed Theta constants. The results of the material constant transformation is listed in Table 15. Notice, the Y-intercept and slope are identical for both transformation directions. This is due to the ε vs t plot being pure experimental data.

Table 15 – Theta-Omega material constant transformation

Temp., T	Stress, σ	Y-Int	$\frac{\theta_4}{\Omega}$	Theta to Omega				Omega to Theta			
				θ_3	θ_4	$\dot{\varepsilon}_0$	Ω	$\dot{\varepsilon}_0$	Ω	θ_3	θ_4
°F	*ksi*		$10^{-4} hr^{-1}$	10^{-2}	$10^{-3} hr^{-1}$	$10^{-4} hr^{-1}$		$10^{-4} hr^{-1}$		10^{-2}	$10^{-3} hr^{-1}$
1200	33.5	0.0	1.90	8.8	1.25	0.97	7.81	1.13	6.34	9.38	1.20
	36.5	0.0	4.00	5.1	3.40	1.73	8.50	2.58	4.95	13.0	1.98
1600	6.30	0.0	2.10	4.1	3.30	1.10	15.7	1.61	8.84	9.10	1.77
	7.30	0.0	3.40	5.0	5.50	2.00	16.1	3.16	9.55	9.73	3.25

5.6.2 Combinational Models

The Theta-Omega identity enables combinational models to be derived that incorporate feature of both models. The Theta creep strain rate [Eq. (10)] can be rewritten as follows using the $I_{\theta\Omega}$ identity

$$\dot{\varepsilon} = (\dot{\varepsilon}_0 / I_{\theta\Omega}) \exp(\theta_4 t) \tag{67}$$

Using the $I_{\theta\Omega}$ identity, the Theta life prediction [Eq. (13)] can be recombined into

$$t_r = \frac{1}{\theta_4} \ln\left(\frac{\varepsilon_r \theta_4 I_{\theta\Omega}}{\dot{\varepsilon}_0} + 1 \right) \tag{68}$$

where life prediction depends on creep ductility.

The Omega creep strain rate [Eq. (4)] can be rewritten using the $I_{\theta\Omega}$ identity as follows

$$\dot{\varepsilon} = I_{\theta\Omega} \theta_3 \theta_4 \exp(\Omega \varepsilon) \tag{69}$$

Using the $I_{\theta\Omega}$ identity, the Omega life prediction [Eq. (4)] can be recombined into

$$t_r = \frac{1}{I_{\theta\Omega}\theta_3\theta_4\Omega} \tag{70}$$

where the Theta constants θ_3 and θ_4 are present.

5.7 OMEGA-SINH IDENTITY

The Omega-Sinh identity is derived as follows. Equating the creep strain rate of the Omega and Sinh models [Eq. (4) and (35)] gives

$$\dot{\varepsilon}_{Omega} = \dot{\varepsilon}_{Sinh} \tag{71}$$

$$\dot{\varepsilon}_0 \exp(\Omega\varepsilon) = A\sinh(\sigma/\sigma_s)\exp(\lambda\omega^{3/2}) \tag{72}$$

Rearranging [Eq. (72)] and taking the natural logarithm of both sides gives

$$\ln\left[\frac{\dot{\varepsilon}_0}{A\sinh(\sigma/\sigma_s)}\right] = \lambda\omega^{3/2} - \Omega\varepsilon \tag{73}$$

For a given stress and temperature, $\dot{\varepsilon}_0$ and $\dot{\varepsilon}_{\min}$ are constant. Introducing the unit-less Omega-Sinh Identity, $I_{\Omega S}$, [Eq. (73)] becomes

$$I_{\Omega S} = \dot{\varepsilon}_0 / A\sinh(\sigma/\sigma_s) \tag{74}$$

$$\varepsilon = (\lambda/\Omega)\omega^{3/2} - \ln\left(I_{\Omega S}\right)/\Omega \tag{75}$$

where $0 \le I_{\Omega S} \le 1$. The term $\omega^{3/2}$ evolves from zero to unity. The above [Eq. (74) and (75)] will be exploited to determine the Sinh constants given the Omega constants and vice-versa.

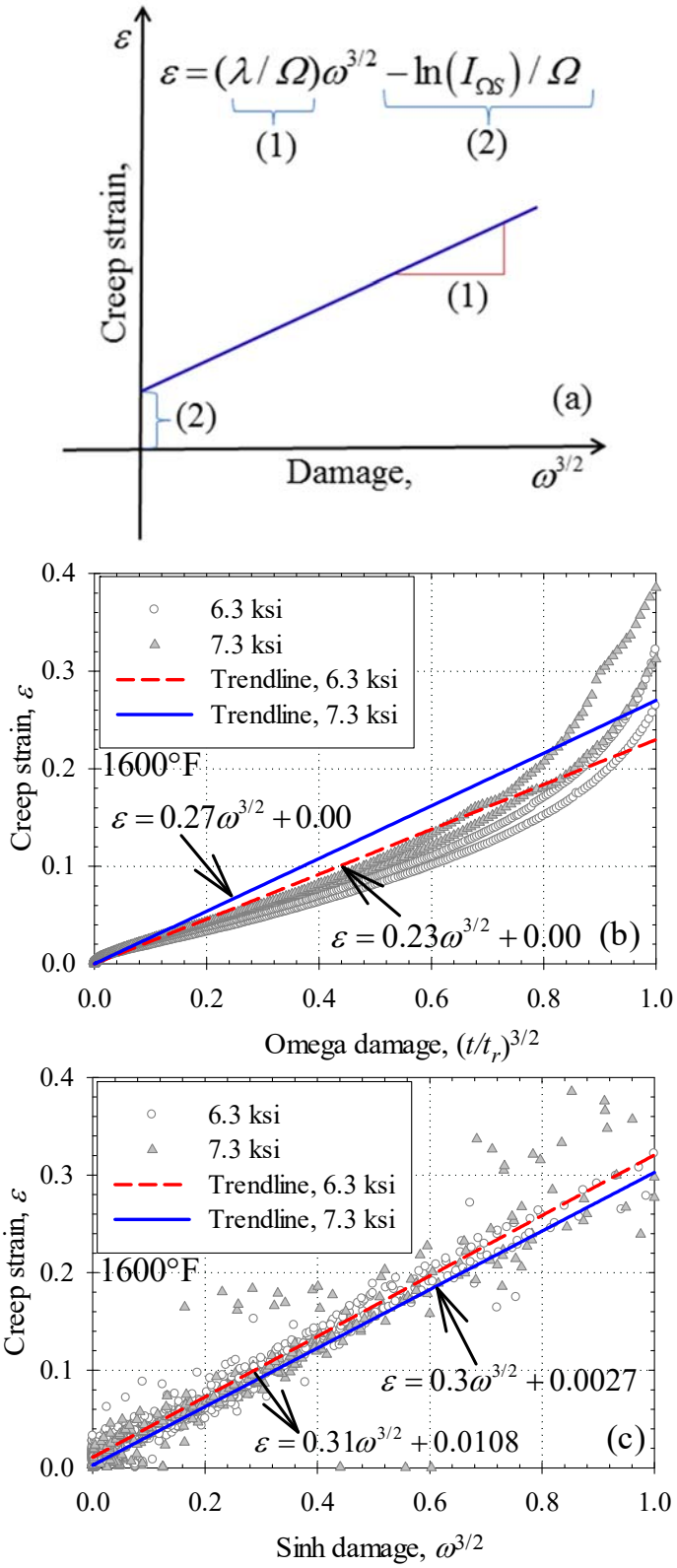

Figure 5.4 – Omega-Sinh transformation (a) graphical approach and (b) Omega-damage and (c) Sinh-damage for Hastelloy X at 1600°F

5.7.1 Constant Determination

Given the Omega constants $\dot{\varepsilon}_0$ and Ω, the Sinh constants A, σ_s, and λ can be found using the graphical approach illustrated in Figure 5.4a. An example transformation for Hastelloy X at 1600°F using Omega and Sinh damage is shown in Figure b and c respectively. The strain is plotted with respect to a damage term $\omega^{3/2}$. The transformation [Eq. (75)] can then be plotted as a linear function. The constant λ is obtained by multiply the slope by Ω. The slope is determined by performing a linear fit to obtain a maximum R-squared value. The A and σ_s constants are obtained by measuring the Y-intercept solving for $I_{\Omega S}$, and then rearranging $I_{\Omega S}$ [Eq. (74)] to solve for A and σ_s. The reverse process of this constant determination process can be applied to find the Omega constants given the Sinh constants. The Omega damage [Eq. (63)] is a function of normalized time thus the graphical approach in Figure 5.4b produces a curvy linear line. The Omega damage is zero when time and creep strain are zero, thus the Y-intercept is always zero as depicted in Figure 5.4b. The Sinh damage [Eq. (38)] is a function of creep strain rate normalized by minimum creep strain rate thus the graphical approach in Figure c produces a straight line. The Sinh damage is zero until the creep strain rate exceeds the minimum creep strain rate, thus the Y-intercept is often greater than zero and equal to the accumulated primary creep strain as depicted in Figure 5.4c.

Using the graphical approach for the Omega-Sinh transformation depicted in Figure a on the collected Hastelloy X data, the Omega constants in Table 13 are used to find transformed Sinh constants and the Sinh constants in Table 14 are used to find transformed Omega constants. The result of the material constant transformation is listed in Table 16. Notice, that depending on if Omega or Sinh damage is applied to plot ε vs $\omega^{3/2}$, the Y-intercept and slope will be different.

Table 16 – Omega-Sinh material constant transformation

Temp., T	Stress, σ	Omega to Sinh						Sinh to Omega					
		Y-Int	$\frac{\lambda}{\Omega}$	$\dot{\varepsilon}_0$	Ω	$\dot{\varepsilon}_{\min}$	λ	Y-Int	$\frac{\lambda}{\Omega}$	$\dot{\varepsilon}_{\min}$	λ	Ω	$\dot{\varepsilon}_0$
°F	*ksi*			$10^{-4} hr^{-1}$		$10^{-4} hr^{-1}$		10^{-2}		$10^{-4} hr^{-1}$			$10^{-4} hr^{-1}$
1200	33.5	0.0	0.35	1.13	6.34	1.13	2.20	3.09	0.53	1.32	3.94	7.36	1.02
	36.5	0.0	0.53	2.58	4.95	3.30	2.62	5.00	0.58	3.32	3.15	5.4	2.53
1600	6.30	0.0	0.27	1.61	9.55	1.61	2.57	1.08	0.31	1.66	3.27	10.9	1.48
	7.30	0.0	0.23	3.16	8.84	3.16	2.03	0.27	0.30	3.04	2.90	9.66	2.96

5.7.2 Combinational Models

The Omega-Sinh identity enables combinational models to be derived that incorporate features of both models. The Omega creep strain rate and life prediction [Eq.(4) and (**5**)] can be re-written using the $I_{\Omega S}$ identity as

$$\dot{\varepsilon} = I_{\Omega S} A \sinh(\sigma / \sigma_s) \exp(\Omega \varepsilon) \tag{76}$$

$$t_r = \left(\frac{1}{I_{\Omega S} A \sinh(\sigma / \sigma_s) \Omega} \right) \tag{77}$$

The Sinh creep strain rate and analytic damage [Eq. (35) and (34)] can be re-written using the $I_{\Omega S}$ identity as

$$\dot{\varepsilon} = (\dot{\varepsilon}_0 / I_{\Omega S}) \exp(\lambda \omega^{3/2}) \tag{78}$$

$$\omega(\dot{\varepsilon}) = \left\{ \frac{1}{\lambda} \ln\left[\frac{\dot{\varepsilon}_{cr}(t)}{(\dot{\varepsilon}_0 / I_{\Omega S})} \right] \right\}^{2/3} \tag{79}$$

Similarly, introducing the Omega life prediction [Eq. (4)] into Sinh damage [Eq. (38)] gives

$$\omega(t) = -\frac{1}{\phi} \ln\left[1 - \left[1 - \exp(-\phi) \right] \dot{\varepsilon}_0 \Omega t \right] \tag{80}$$

where [Eq. (79)] is used to calculate analytical damage, and [Eq. (80)] is used to predict damage.

5.8 SINH-THETA IDENTITY

The Sinh-Theta identity is derived as follows. Equating the creep strain rate of the Sinh and Theta models [Eq. (**35**) and (10)] gives

$$\dot{\varepsilon}_{Sinh} = \dot{\varepsilon}_{Theta} \tag{81}$$

$$A \sinh(\sigma / \sigma_s) \exp(\lambda \omega^{3/2}) = \theta_4 \theta_3 \exp(\theta_4 t) \tag{82}$$

Rearranging [Eq. (82)] and taking the natural logarithm of both sides gives

$$\ln\left[\frac{\theta_3 \theta_4}{A \sinh(\sigma / \sigma_s)} \right] = \lambda \omega^{3/2} - \theta_4 t \tag{83}$$

For a given stress and temperature, θ_3, θ_4 and $\dot{\varepsilon}_{\min}$ are constant. Introducing a unit-less Sinh-Theta identity, $I_{S\theta}$, [Eq. 83] becomes

$$I_{S\theta} = \theta_3 \theta_4 / A \sinh(\sigma / \sigma_s) \tag{84}$$

$$\omega^{3/2} = (\theta_4 / \lambda) t + \ln(I_{S\theta}) / \lambda \tag{85}$$

where $0 \le I_{S\theta} \le 1$.

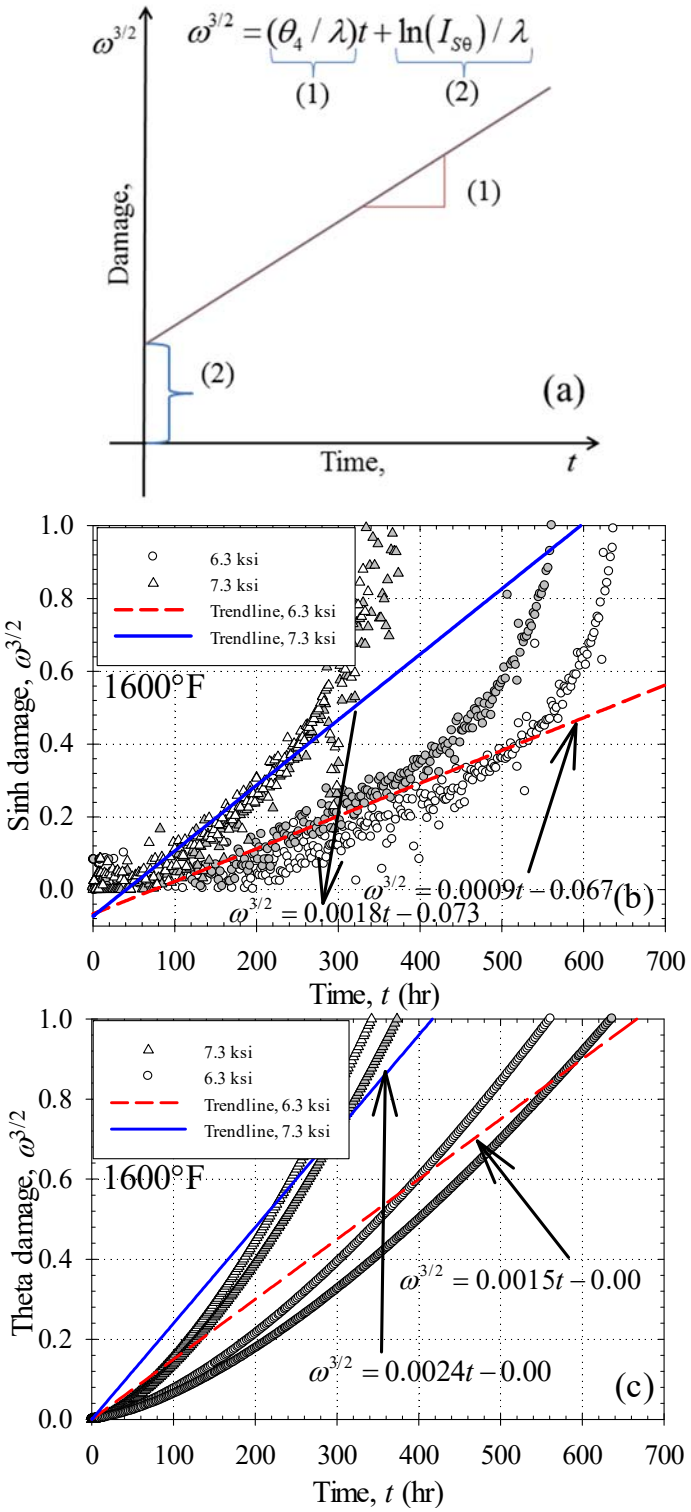

Figure 5.5 – Sinh-Theta transformation (a) graphical approach and (b) Sinh-damage and (c) Theta-damage for Hastelloy X at 1600°F

5.8.1 Constant Determination

Given the Sinh constants A, σ_s, and λ, the Theta constants θ_3 and θ_4 can be found using the graphical approach illustrated in Figure 5.5a. An example transformation for Hastelloy X at 1600°F using Sinh and Theta damage is shown in Figure 5.5b and c respectively. The damage term $\omega^{3/2}$ is plotted with respect to time. The constant θ_4 is obtained by multiply the slope by λ. The slope is determined by performing a linear fit to obtain a maximum R-squared value. The constant θ_3 is obtained by measuring the Y-intercept solving for $I_{S\theta}$, and then rearranging $I_{S\theta}$ [Eq. (84)] to solve for θ_3. The reverse of this constant determination process could be applied to find the Sinh constants given Theta constants. The Sinh damage [Eq. (38)] is a function of the creep strain rate so it produces an accelerating curve linear evolution with time. The Sinh damage is zero until the creep strain rate reaches the minimum creep strain rate. The Y-intercept is needed to offset this fact as depicted in Figure 5.5b. The Theta damage [Eq. (14)] is a function of normalized time and would produce a linear plot; however, it is curvy linear in the graphical approach due to the $\omega^{3/2}$ term. The Theta damage is zero when time and creep strain are zero, thus the Y-intercept is always zero as depicted Figure 5.5c.

Using the graphical approach of the Sinh-Theta transformation depicted in Figure 5.5a on the collected Hastelloy X data, the Sinh constants in Table 14 are used to find transformed Theta constants and the Theta constants in Table 12 are used to find transformed Sinh constants. The result of the material constant transformation is listed in Table 17. Notice, that depending on if Sinh or Theta damage is applied to plot $\omega^{3/2}$ vs *t*, the Y-intercept and slope will be different.

Table 17 – Sinh-Theta material constant transformation

Temp., T	Stress σ	Theta to Sinh						Sinh to Theta					
		Y-Int	$\frac{\theta_4}{\lambda}$	θ_3	θ_4	$\dot{\varepsilon}_{min}$	λ	Y-Int	$\frac{\theta_4}{\lambda}$	$\dot{\varepsilon}_{min}$	λ	θ_3	θ_4
°F	*ksi*		$10^{-3}hr^{-1}$	10^{-2}	$10^{-3}hr^{-1}$	$10^{-4}hr^{-1}$			$10^{-3}hr^{-1}$	$10^{-4}hr^{-1}$		10^{-2}	$10^{-3}hr^{-1}$
1200	33.5	0.0	0.42	8.8	1.25	1.10	2.08	-0.057	0.3	1.29	3.94	8.69	1.18
	36.5	0.0	0.85	5.1	3.40	2.79	2.83	-0.167	1.0	3.12	3.15	5.84	3.15
1600	6.30	0.0	0.80	4.1	3.30	1.35	2.20	-0.067	0.9	1.66	3.33	4.43	3.00
	7.30	0.0	1.60	5.0	5.50	2.75	2.29	-0.073	1.8	3.04	2.90	4.71	5.20

5.8.2 Combinational models

The Sinh-Theta identity enables combinational models to be derived that incorporate features of both models. The Sinh creep strain rate [Eq. (**35**)] can be re-written using the $I_{S\theta}$ identity as

$$\dot{\varepsilon} = (\theta_3\theta_4 / I_{S\theta})\exp(\lambda\omega^{3/2}) \tag{86}$$

and the Sinh analytical damage [Eq. (34)] can be rewritten as

$$\omega(\dot{\varepsilon}) = \left\{\frac{1}{\lambda}\ln\left[\frac{\dot{\varepsilon}_{cr}(t)}{(\theta_3\theta_4 / I_{S\theta})}\right]\right\}^{2/3} \tag{87}$$

Similarly, introducing the Theta life prediction [Eq. (13)] into the Sinh damage [Eq. (38)] gives

$$\omega(t) = -\frac{1}{\phi}\ln\left[1-\left[1-\exp(-\phi)\right]\frac{\theta_4 t}{\ln(\varepsilon_r / \theta_3 + 1)}\right] \tag{88}$$

where damage depends on creep ductility. Another option is to apply the combinational Theta life prediction [Eq. (70)] into the Sinh damage [Eq. (38)] resulting in a special Theta-Omega-Sinh combinational model for damage.

$$\omega(t) = -\frac{1}{\phi}\ln\left[1-\left[1-\exp(-\phi)\right]I_{\theta\Omega}\theta_3\theta_4 t\right] \tag{89}$$

The Theta creep strain rate [Eq. (10)] can be rewritten using the $I_{S\theta}$ identity as

$$\dot{\varepsilon} = I_{S\theta}A\,\mathrm{Sinh}(\sigma/\sigma_s)\exp(\theta_4 t) \tag{90}$$

and the Theta life prediction [Eq. (13)] can be written into

$$t_r = \frac{1}{\theta_4}\ln\left(\frac{\varepsilon_r\theta_4}{I_{S\theta}A\sinh(\sigma/\sigma_s)}+1\right) \tag{91}$$

where life prediction depends on creep ductility.

A summary of the new combinational constitutive models enabled by metamodeling is provided in Table 18. In total six new constitutive models are introduced in this study. Notice in all six models, the creep strain rate and rupture time have been transformed while the damage remains unchanged. This is due to the simplicity of the Theta and Omega damage making model transformation involving damage insignificant; however, due to rupture time being included in the calculation of damage, the damage evolution of each model will be different.

A relationship between the identities $I_{\theta\Omega}$, $I_{\Omega S}$, and $I_{S\theta}$ can be derived by combining [Eq. (64),(74), and (84)] as

$$I_{\Omega S} = I_{\theta\Omega}I_{S\theta} \tag{92}$$

Using the above relationship, calibration of any two identities will provide the third.

Table 18 – Combinational model summary

No	Base model	Creep Strain Rate	Damage	Life Prediction	Eqn.
		Theta-Omega Identity, $I_{\theta\Omega} = \left(\dot{\varepsilon}_0 / \theta_3\theta_4\right)$			
M1	Theta	$\dot{\varepsilon} = (\dot{\varepsilon}_0 / I_{\theta\Omega}) \exp\left(\theta_4 t\right)$	$\omega(t) = \frac{t}{t_r}$	$t_r = \frac{1}{\theta_4} \ln\left(\frac{\varepsilon_r \theta_4 I_{\theta\Omega}}{\dot{\varepsilon}_0} + 1\right)$	(67) (68)
M2	Omega	$\dot{\varepsilon} = I_{\theta\Omega}\theta_3\theta_4 \exp\left(\Omega\varepsilon\right)$	$\omega(t) = \frac{t}{t_r}$	$t_r = \left(\frac{1}{I_{\theta\Omega}\theta_3\theta_4\Omega}\right)$	(69) (70)
		Omega-Sinh Identity, $I_{\Omega S} = \dot{\varepsilon}_0 / A\sinh(\sigma / \sigma_s)$			
M3	Omega	$\dot{\varepsilon} = I_{\Omega S} A \sinh(\sigma / \sigma_s) \exp\left(\Omega\varepsilon\right)$	$\omega(t) = \frac{t}{t_r}$	$t_r = \left(\frac{1}{I_{\Omega S} A \sinh(\sigma / \sigma_s)\Omega}\right)$	(76) (77)
M4	Sinh	$\dot{\varepsilon} = (\dot{\varepsilon}_0 / I_{\Omega S}) \exp\left(\lambda\omega^{3/2}\right)$	$\omega(t) = -\frac{1}{\phi} \ln\left[1 - \left[1 - \exp\left(-\phi\right)\right] \frac{t}{t_r}\right]$	$t_r = \left(\frac{1}{\dot{\varepsilon}_0 \cdot \Omega}\right)$	(78) (80)
		Sinh-Theta Identity, $I_{S\theta} = \theta_3\theta_4 / A\sinh(\sigma / \sigma_s)$			
M5	Sinh	$\dot{\varepsilon} = (\theta_3\theta_4 / I_{S\theta}) \exp\left(\lambda\omega^{3/2}\right)$	$\omega(t) = -\frac{1}{\phi} \ln\left[1 - \left[1 - \exp\left(-\phi\right)\right] \frac{t}{t_r}\right]$	$t_r = \frac{1}{\theta_4} \ln\left(\frac{\varepsilon_r}{\theta_3} + 1\right)$	(86) (88)
M6	Theta	$\dot{\varepsilon} = I_{S\theta} A \sinh(\sigma / \sigma_s) \exp\left(\theta_4 t\right)$	$\omega(t) = \frac{t}{t_r}$	$t_r = \frac{1}{\theta_4} \ln\left(\frac{\varepsilon_r \theta_4}{I_{S\theta} A \sinh(\sigma / \sigma_s)} + 1\right)$	(90) (91)

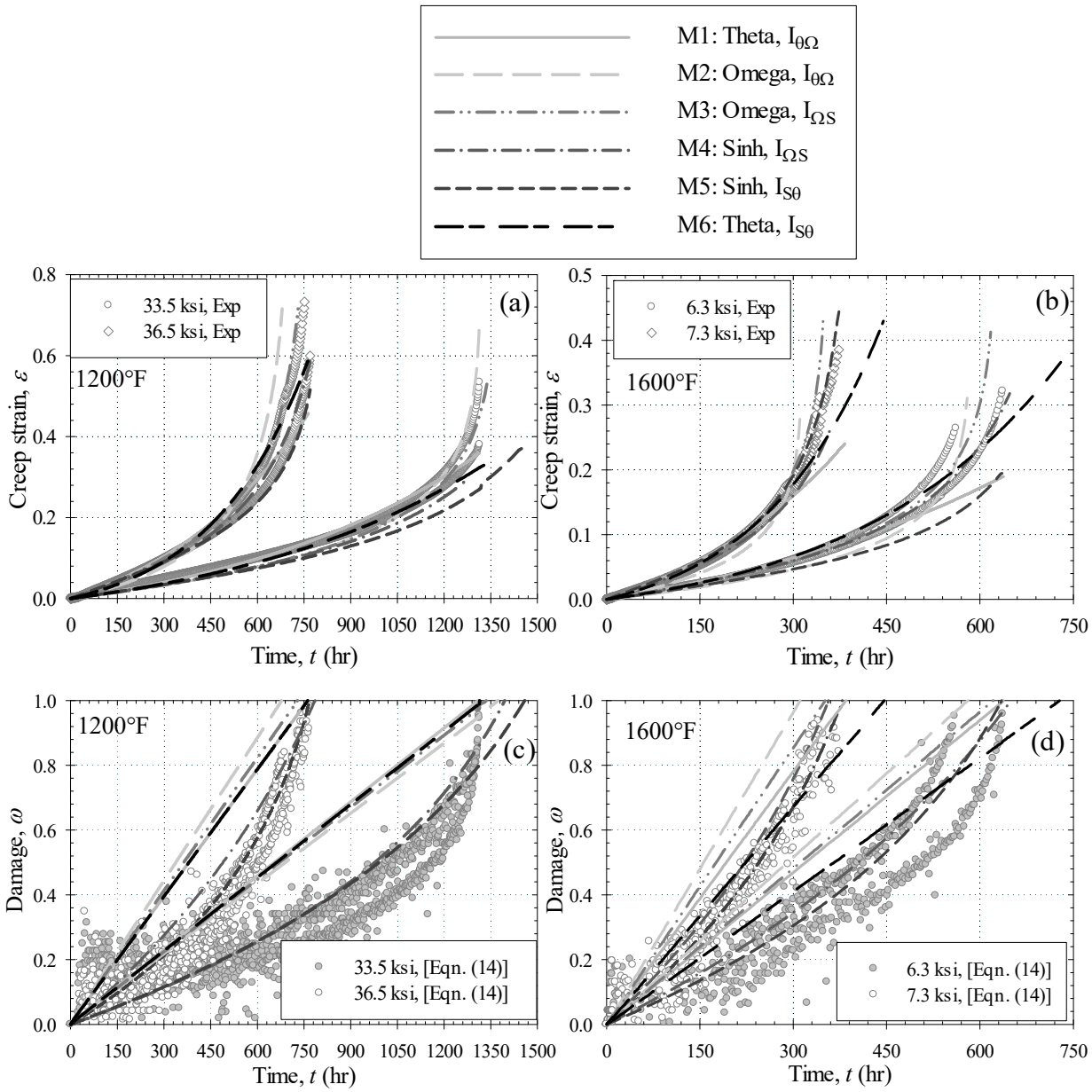

Figure 5.6 – Comparison of combinational models (a-b) deformation, (c-d) damage prediction for Hastelloy X at 1200°F and 1600°F

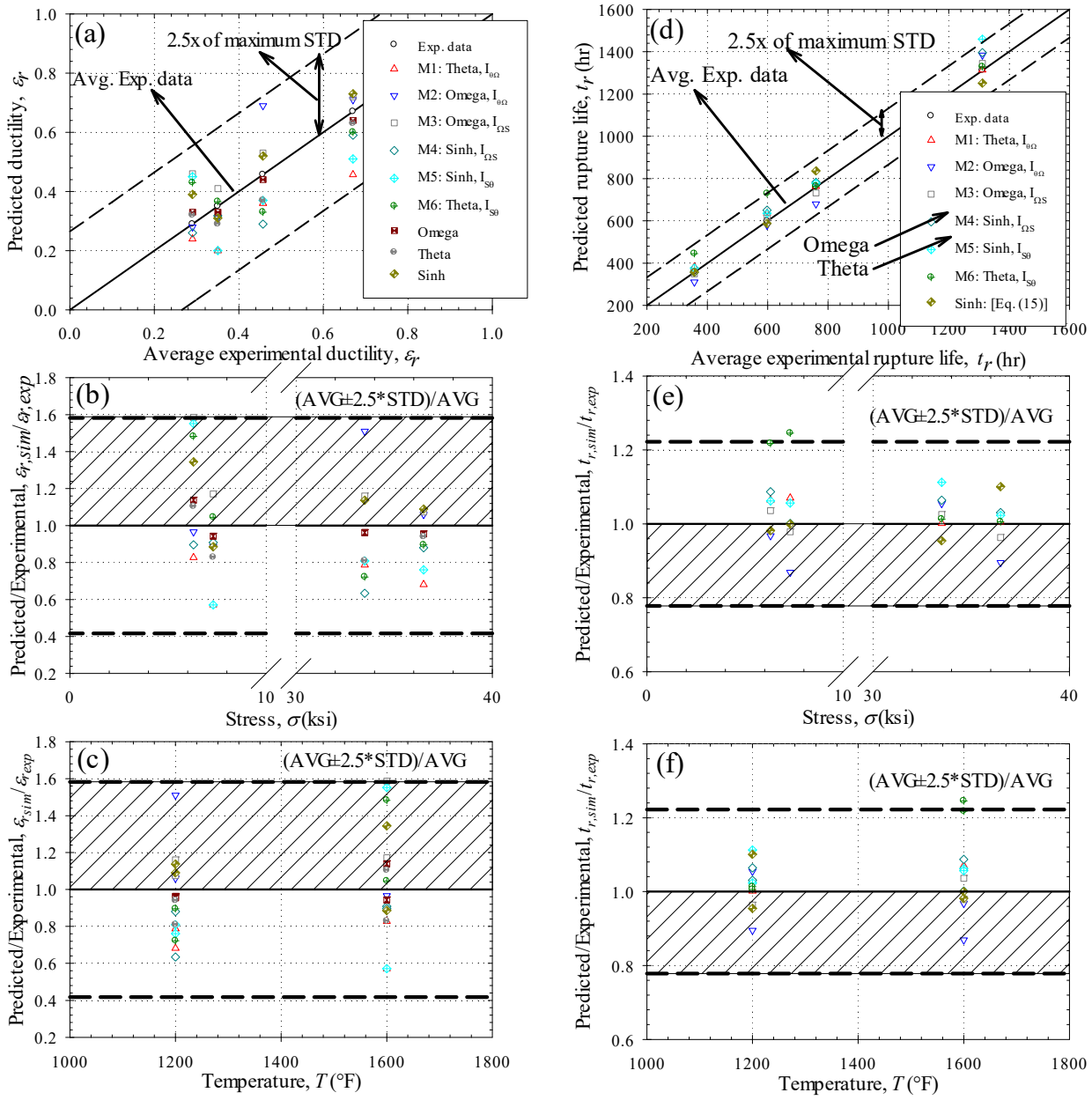

Figure 5.7 – Model performance in predicting (a-c) creep ductility and (d-f) rupture life where the dotted lines indicate 2.5x of the maximum standard deviation in repeated tests. In the ratio plots, the dotted line indicates the ratio of 2.5x of the maximum standard deviation divided by the average obtained in repeated tests. The highlight areas indicate conservative predictions.

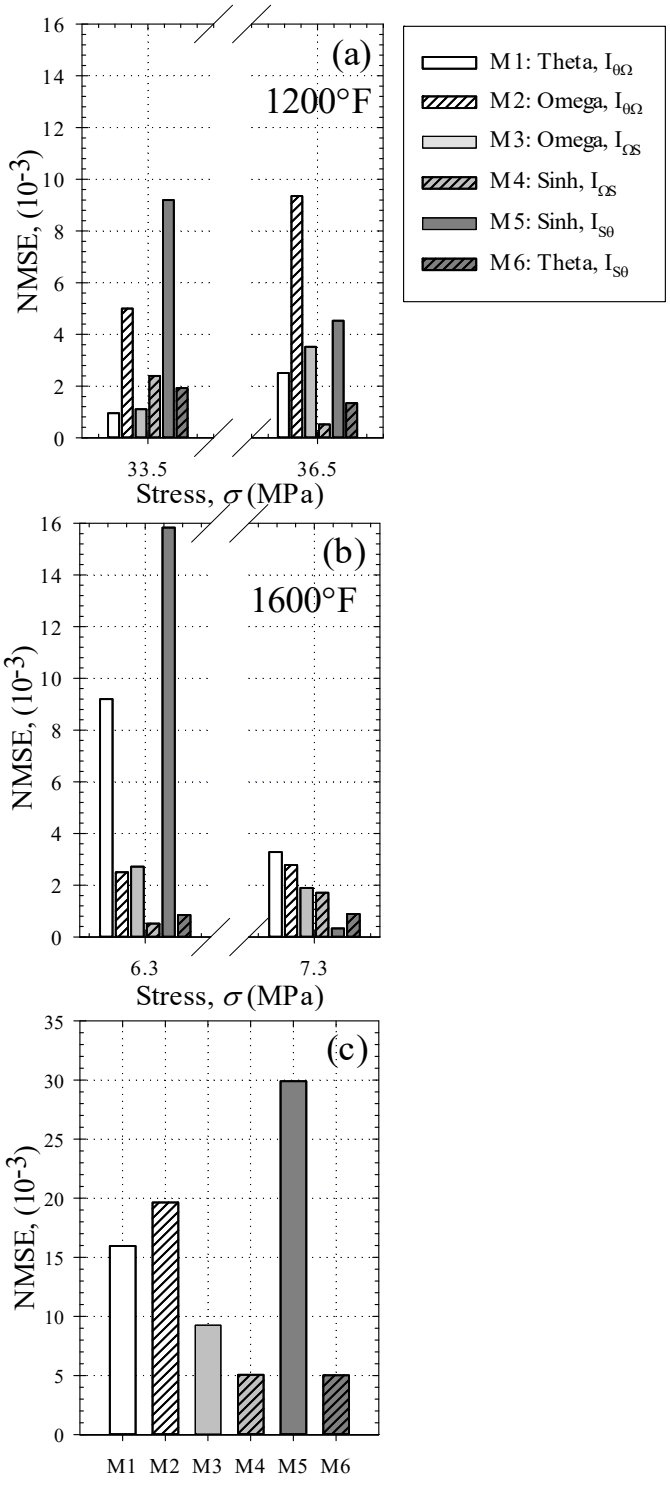

Figure 5.8 – Creep deformation NMSE of combinational models at (a) 1200°F, (b) 1600°F, and (c) cumulative

5.9 Results and Discussion

The creep deformation and damage curves calculated using the six combinational models on Hastelloy X at 1200°F and 1600°F are depicted in Figure 5.6. It is observed that in general, the creep deformation of the models is in agree with the experimental data. Regarding damage, the M1-M3 and M6 models employ a linear damage equation. While the M4 and M5 have a nonlinear damage equation. The variation observed in the damage predicted between these two types of damage equations comes from the equation used to calculate the rupture time for each model listed in Table 18.

Three approaches are applied to analysis the performance of the new combinational models. First, an acceptability analysis is performed. Next, a conservative versus non-conservative analysis is performed. Finally, a normalized mean-squared error (NMSE) analysis is performed.

5.10.1 Acceptability

In the current study, an acceptable model is a model that predicts between the average line and boundaries of 2.5x the maximum standard deviation recorded in repeated creep tests at any test condition. The boundaries encompass almost 99% of the experimental data. For creep ductility, the maximum standard deviation of 0.265 came from the tests conducted at 33.5 ksi and 1200°F. For rupture, the maximum standard deviation of 133 hr came from the tests conducted at 6.3 ksi and 1600°F. When examining the simulation versus experimental data plots in Figure a and d, it is observed that all the models lie within the boundaries.

The simulation versus experimental data plots can be deceptive because they assume that the largest standard deviation of a set of repeated tests applies for all test conditions; however, the uncertainty of creep with respect to the boundary conditions is heteroscedastic where increasing temperature or decreasing stress will lead to larger rupture time standard deviations. Similarly,

increasing temperature and increasing stress will lead to larger ductility standard deviations. This can lead to a false sense of safety for short duration creep tests. To overcome this, we can plot the upper and lower boundaries of acceptability as the ratio of 2.5x of the maximum standard deviation divided by the average obtained in repeated tests. The ratio plots Figure 5.7b,c and e,f can be used to determine model acceptability. It is observed for creep ductility that all the models are acceptable with M3 just inside the upper limit. For creep rupture, all models except M6 are acceptable where M6 is 2% above the limit.

Table 19 – Conservatism (Yes, No, or Mixed) of models at given test conditions

Model	Creep ductility, ε_r		Rupture life, t_r		Overall	Cumulative NMSE (10^{-3})
	6.3 -7.3 ksi 1600°F	33.5 – 36.5 ksi 1200°F	6.3 -7.3 ksi 1600°F	33.5 – 36.5 ksi 1200°F		
M1	NO	NO	NO	YES	NO	15.94
M2	NO	YES	YES	MIXED	YES	19.63
M3	YES	YES	MIXED	MIXED	YES	9.240
M4	NO	NO	MIXED	NO	NO	5.050
M5	MIXED	NO	NO	NO	NO	29.89
M6	YES	NO	NO	MIXED	NO	5.010
Theta	MIXED	NO	NO	NO	NO	7.430
Omega	MIXED	NO	NO	NO	NO	3.370
Sinh	MIXED	YES	YES	MIXED	MIXED	2.480

5.10.2 Conservatism

An important aspect of design for creep is the idea of conservative versus non-conservative predictions. In general, conservatism is desired due to the uncertainty of creep experiments that increases as the temperature is increased and stress increased (ductility) or decreased (rupture). A conservative constitutive model is a model that slightly over predicts the creep ductility (between the average line and upper boundary) and under predicts the rupture time (between the average line and the lower boundary) in comparison to experiments. The conservative zones are highlighted in the Figure 5.7b,c and e,f. The conservative/non-conservative performance of the models under the available test conditions is summarized in Table 19. It is observed that overall M2 and M3 are conservative, the Sinh is of a mixed nature, and M1, M4, M5, M6, Theta, and Omega are non-conservative. The M2 and M3 models outperform the classical models in conservatism.

5.10 Cumulative NMSE

To take a closer look at the performance of the new combinational models in comparison to the classics, the NMSE of the creep deformation is calculated for each model for each combination of stress and temperature and plotted in Figure 5.8. In addition, the cumulative NMSE of each model is provided in Table 19.

It is observed that the worst performing model in comparison to the classics is M5 with the highest cumulative NMSE of all models. Counter to the trend observed in the M4 and M6 models, in M5 the input model constants do not correlate to the calculated cumulative NMSE. While acceptable, the M5 cumulative NMSE is 29.89E-3; a quantity much larger than expected. The M5 model is based on the Sinh and Theta models. The error tends to accumulate in the low-stress simulations as observed in Figure 5.8. This is similar to the trend observed in the Theta model in section 0 but

exaggerated. The origin of the poor performance is multifaceted. The determination of the $I_{S\theta}$ identity is a key factor. When using the Sinh-based damage to find the constants, the Y-intercept ($\ln(I_{S\theta})/\lambda$) is non-zero leading to high sensitivity in the determination of the $I_{S\theta}$ identity. A small change in Y-intercept leads to a dramatic change in the $I_{S\theta}$ identity. Another factor is function form. Examining the M5 equations in Table 18, the $I_{S\theta}$ identity is in the denominator of the function that represents the minimum creep strain rate. The minimum creep strain rate is a sensitivity property where a small deviation in magnitude causes a significant shift of the creep deformation curve. Despite these deficiencies, the M5 model is able to produce an acceptable prediction of creep deformation and rupture data according to acceptability analysis.

The best performing models are equally M4 and M6, with the lowest cumulative NMSE of all models. The M4 and M6 models outperform the Theta model with a cumulative NMSE of 5.00E-3 versus 7.43E-3 but are inferior to the Omega and Sinh models at 3.37E-3 and 2.48E-3 respectively. It is reasoned that the goodness of the models correlates to the quality of the input model constants and source equations. The M4 model is a coupling of the Omega and Sinh constants that have a cumulative NMSE of 3.37E-3 and 2.48E-3 respectively. The M6 model is a coupling of the Theta and Sinh constants that have a cumulative NMSE of 7.43E-3 and 2.48E-3 respectively. In both cases, the cumulative NMSE remains near the parent models.

To summarize, the combinational models are acceptable, the M2 and M3 models exhibit superior conservatism compared to the classic models, and the M4 and M6 models hold NMSE values near their parent models below the Theta model.

5.11 SUMMARY

In summary, metamodeling is employed to derive functional relationships between the Omega, Theta, and Sinh creep deformation, damage, and rupture models.

1) The model transformation identities Theta-Omega, Omega-Sinh, and Sinh-Theta are derived that can be used to convert one model's constants to the constant of another. These identities when mathematically manipulated reveal six viable combinational models.

2) It is determined that the combinational models produce acceptable predictions of creep deformation and rupture data, can be more conservative than the classic models, and the normalized mean square error can be on par with the classic models. Metamodeling is a viable approach for the creep problem. Metamodeling has great potential for many classes of creep models including time-temperature parameter models, continuum damage mechanics models, unified viscoplasticity models, and even microstructural mechanism-based models. Because metamodeling is logic-based, it lends itself to numerical implementation such that given a group of symbolically programmed constitutive models, the identification of model identities and combinational constitutive models can be automated.

Regarding the current study, future work includes the 3D finite element implementation and simulation of the combinational models to analyze convergence, notch-sensitivity, and damage localization of the new models.

Chapter 6: Disparate Data Problem and Creep Design

6.1 INTRODUCTION

Creep data exists in a diaspora. Creep data is not always available in the regime (short, intermediate-, and long-term) or form (minimum-creep-strain-rate, creep deformation, stress-rupture, etc.) of interest. This is particularly true for new alloys where the time-to-qualification can take between 10 to 20 years. Often extrapolation is performed using short-term data that include high uncertainty. In some cases, extrapolation is limited up to certain multiple of the longest data (e.g. Standards recommended that stress-rupture extrapolations should not exceed three times the duration of the longest experiment). Extrapolation beyond the limit may lead to unrealistic prediction. For example, a creep deformation model calibrated using short-term creep deformation data (e.g. 10^3 hrs) is highly unlikely to generate realistic predictions near 10^5 hrs. This study proposes integrating disparate creep data in the calibration process. It is hypothesized that cross-calibrating a constitutive model to any and every form of available creep data (across test type, stress and temperature range) will lead to more reliable extrapolations. This is demonstrated by integrating minimum-creep-strain-rate, stress-rupture, and short-/intermediate-term creep deformation data into the calibration process of a constitutive model. In addition, the approach facilitates the development of creep design maps that can be used for determining design boundary condition, material selection, and to compare the interpolation and extrapolation ability of the models.

Motivation

Drives to extend the service life of existing fossil energy power plants will lead to structural components with lives beyond 10^6 hours. In addition, the ongoing development of Advanced-Ultrasupercritical (A-USC) power plants has created a materials challenge where new material are

needed to withstand operating pressures above 4000 psi and temperatures exceeding 1400°F. These conditions make it critically important to consider creep deformation and damage in the design process of FE power plant components and systems. Knowledge concerning the long-term creep behavior of existing and new materials is needed to make design decisions; however, often only limited creep data is available. The average time-to-qualification of new creep resistant alloys is between 10 to 20 years. This development time is consumed by computational materials design, thermomechanical processing optimization, and the physical experiments needed to qualify the long-term creep resistance of a material [5].

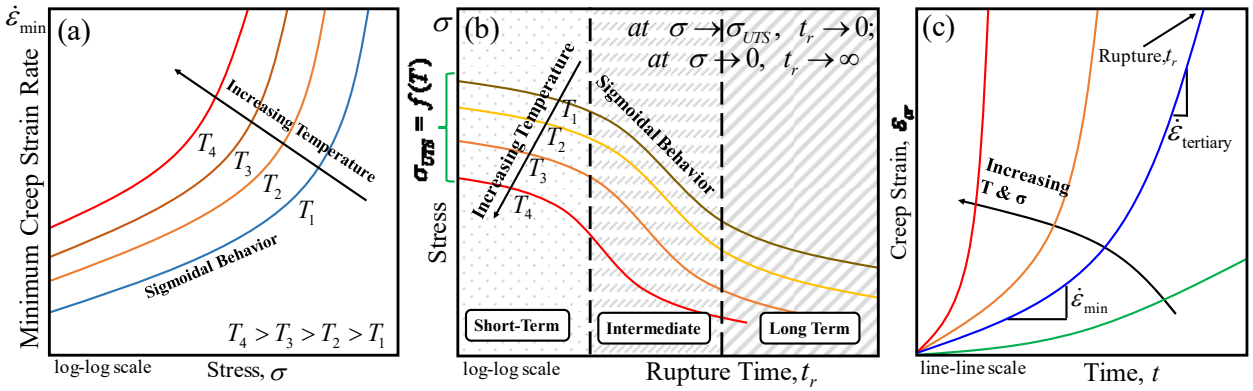

Figure 6.1 – Disparate types of creep data (a) minimum-creep-strain-rate exhibiting a sigmoidal behavior, (b) stress-rupture data that can be sub-divided into short-term, intermediate, and long-term data, (c) creep deformation including primary, secondary and tertiary regimes

Creep Data

Usually, creep data is created by performing a variety of short- and/or long-term creep tests. The most common data collected are minimum-creep-strain-rate, stress-rupture, and deformation data as shown in Figure 6.1. Minimum-creep-strain-rate data is easy to generate using short-term creep tests but it also can be created in an accelerated fashion using the stress relaxation tests (SRTs)

where multiple isotherms of minimum-creep-strain-rate data is generated from a single specimen [128]. Minimum-creep-strain-rate data is reported on a log-log scale with stress and per isotherm as depicted in Figure 6.1a. Long-term stress-rupture data is generally accrued by national laboratories and business entities who have a vested interest and suitable financial backing to commit to long-term creep testing (continuous testing for decades or more) [121]. An ideal stress-rupture curve on a log-log scale exhibits a sigmoidal transition from high-stress to low-stress as illustrated in Figure 6.1b. At the ultimate tensile strength, the specimen ruptures instantly while at very low stress, life is near infinite (>> 10^6 hours = 114 years). For legacy materials such as 304 stainless steel, tests have been performed beyond 10^5 hours and there are ongoing tests estimated to failure at $\gg 10^6$ hours [5]. Most previously performed and ongoing tests began without a digital data acquisition (DAQ) system. Instead, a military log of the elongation and time was recorded, and tables of time-to-creep-strain generated to profile the creep deformation responses. Most often the "full" creep deformation curve has not been digitized and the military logs have either been neglected and/or misplaced over the years of testing. It is difficult to obtain the full long-term creep deformation curves. To bridge this gap, short/intermediate-term creep deformation tests are performed with modern DAQs. The stress and temperature conditions of these tests are carefully selected to induce rupture within 10^4 [51]. A typical creep deformation curves is shown in Figure 6.1c. Creep deformation is composed of primary, secondary, and tertiary regimes with both the appearance and dominance of these regimes dependent on stress and temperature. The minimum-creep-strain-rate (Figure 6.1a) and stress-rupture (Figure 6.1b) exist as points of interest on a creep deformation curve at a set isostress and isotherm. For legacy materials, the availability of long-term "full" creep deformation curves are limited. For modern materials, not enough time has

passed for long-term curves to have been generated. A gap in long-term creep deformation data exists. To bridge the gap, extrapolation is necessary.

Extrapolation

The extrapolation of creep behavior can be performed by fitting different form of creep models to short/intermediate creep data and then simulating outside of the available data points. These extrapolations assume that the existing trend in the available data persists and that the models' functional form accurately describes the creep behavior in the extrapolated region. In general, extrapolations are not reliable and are difficult to assess. Empirical evidence shows that the 0% and 100% reliability bands for creep-rupture expand as the applied stress is reduced such that a low stress and elevated temperature the bands may exist decades apart [5]. The combined uncertainty of extrapolations and material performance necessitates that generous safety factors be applied in design [[**125**]. A new material with 30,000 hours of creep data, extrapolated to 100,000 hours has no guarantee of reliability. Creep extrapolation methods have evolved with the evolution of creep models. The earliest extrapolation approach uses Time-Temperature Parametric (TTP) models for stress-rupture prediction [101,129]. These models exist as a relationship between time and temperature expressed as a parametric function of stress. When calibrated to sufficient short duration stress-rupture data, extrapolations to long-life can be made. The TTP models can be further utilized to predict the time to percent-creep-strain at various increments (such as 0.1, 1, 5%, etc.) or to predict the time to onset of tertiary creep [130,131]. Standards recommended that TTP extrapolations should not exceed three times the duration of the longest experiment [[**132**]. Recent work has shown that in some cases this restriction can be eased by performing rigorous statistical analysis [133,134]. The European Creep Collaborative Committee (ECCC) has outlined a standard procedure for this process [135].

Constitutive Laws

Over time, the focus has shifted from extrapolations using simple TTP models to the use of constitutive models. First, the constitutive model is calibrated to short/intermediate-term creep data to determine the material constants per isotherm within the given stress range. Second, the material constants are defined as a function of temperature and/or stress. Third, interpolation and extrapolation are performed, either analytically or numerically (using the finite element method).

In the case of analytical extrapolation, the constitutive laws are rearranged/modified to predict points of interest such as the rupture life, damage state, creep ductility, minimum-creep-strain-rate, etc [61, 136]. Hayhurst found that 30x stress-rupture extrapolations are possible with ±20% accuracy when using the theta-projection constitutive model; however, the resulting creep deformation curves are unsuitable, largely over predicting the creep deformation and ductility [137]. Maruyama and Brown established that the theta-projection can further be used to extrapolate the minimum-creep-strain-rate, creep deformation, and rupture curves [138,139]. Abdallah and colleagues showed that extrapolated creep deformation curves can be generated by modifying the Wilshire rupture model [140].

In the case of numerical extrapolation, the constitutive models are programmed into the finite element (FE) method and the service environment and geometry of a structural component simulated. The calibrated material constants are programmed as a function of stress and/or temperature, which enables interpolation and extrapolation of the creep properties per time step. Using FE analysis, different load and temperature intensities, rates, and distributions as well as different geometry than those applied in experiments can be simulated. Rarely does the available creep data match the conditions found in an FEA simulation. For example, an ideal structural component should be design well into the elastic regime and yet the creep rupture behavior of most

alloys at <40% of the yield strength is rarely known. Continuum damage mechanics (CDM) models are popular for extrapolation because minimum-creep-strain-rate, creep deformation, and rupture predictions are furnished using a single model [40,85,140]. The application of CDM in calculating damage and crack growth under creep, fatigue, creep-fatigue, and other detrimental environments is well-poised [141,142]. Many uniaxial CDM models have been extended to a multiaxial form [143]. Rules concerning the design and life-extension of structural components using CDM models exist [144]. Models also exist for the creep of anisotropic materials; incorporating a damage tensor that accommodates various degrees of anisotropic damage [144,145]. The mathematical and numerical stability of CDM models has also been investigated [38,39].

Creep Design Maps

Once models (TTP, constitutive, CDM, or otherwise) are calibrated and the material properties functionalized, the interpolation and extrapolation ability can be reported graphically by creating a Creep Design Map. In these maps, creep properties (such as minimum-creep-strain-rate, rupture, and/or time-to-creep-strain) are presented in contour where stress and temperature form the axes. Three uses are immediately evident for creep design maps. They can be used for

(a) Design [138,148]. For a given material, creep design maps can be used to determine which boundary conditions meet specific design requirements such as rupture life, elongation, damage, etc.;

(b) Material selection [149]. Once creep design maps have been generated for several materials, the maps can be used to selection the most appropriate material for given boundary condition. Hypothetically, Ashby-like plots can also be created;

(c) Model comparison [150]. Creep design maps are specific to the model used to create them. If creep design maps are generated for more than one model, the interpolation and extrapolation ability of the models can be compared.

A variety of creep design maps have been created. Brown and Evans created time-to-creep-strain and/or rupture design maps for the extrapolation of short-term creep data [138]. Hyde and colleagues suggested the use of such design maps to determine realistic test and operating conditions [148]. Fujiyama developed Ashby-like maps to facilitate material selection under creep-fatigue conditions [149]. Stewart created time-to-creep-strain design maps to identify the dominant creep regime (primary, secondary, or tertiary) using CDM [150].

Problem Statement

It is evident that gaps exist in the creep data available for most materials. Creep data is not always available in the regime (short, intermediate-, and long-term) or form (minimum-creep-strain-rate, creep deformation, stress-rupture, etc.) of interest. It is hypothesized that cross-calibrating a constitutive model to any and every form of creep data will lead to more reliable extrapolations. This requires integrating disparate creep data into the calibration process of a constitutive model. The CDM models are ideal for this goal because the coupled nature of the creep strain rate and damage rate equations enables calibration using many types of creep data.

6.2 OBJECTIVE

The objectives of this study are to

A. provide a detailed procedure for calibrating CDM models using disparate creep data;

B. demonstrate the reliability of extrapolations using post-audit validation where the calibrated model is compared to additional creep data that was not used in the calibration process;

C. illustrate a variety of creep design maps and demonstrate that the interpolation and extrapolation ability of CDM models can be compared graphically using creep design maps.

In this study, six steps are executed to accomplish these objectives. First, the Kachanov-Rabotnov (KR) and Sine-hyperbolic (Sinh) CDM models are introduced. Next, the procedure for calibrating CDM models using disparate creep data is described. Third, the models are calibrated to minimum-creep-strain-rate, creep deformation, and stress-rupture data collected from various sources. Fourth, the calibrated material constants are defined as a temperature-dependent-function of temperature for interpolation and extrapolation. Fifth, post-audit validation is performed by comparing against additional creep data that was not used in calibration. Finally, programming into a numerical algorithm is developed to generate minimum-creep-strain-rate, creep deformation, damage, and rupture design maps.

Model Selection	Select the creep model of interest. (Kachanov-Rabotnov, Sinh, etc.)
Segregation	Segregate the model into equations related to each type of creep data. (Minimum-Creep-Strain-Rate, Stress-Rupture, Creep Deformation, etc.)
Calibration	Calibrate the material constants of the equations using the creep data.
Regression	Use regression analysis to convert material constants into temperature-dependent functions. $f_i(T)$
Validation	Take the pre-calibrated model and compare it to additional data not used in the calibration process.
Design	Make interpolative and extrapolative prediction of creep behavior. Plot these predictions as Creep Design Maps.

Figure 6.2 – Calibration procedure for CDM models to disparate creep data

6.3 Model Calibration Procedure

The first objective of this study is to provide a detailed procedure for calibrating CDM models using disparate creep data. The procedure for disparate database calibration consists of six steps illustrated in Figure 6.2. The first step is to select a model of interest. The second step is to segregate the model into equations related to each type of creep data (i.e. minimum-creep-strain-rate, stress-rupture, creep deformation etc.) such that they can be calibrated independently. In the steps three and four, the material constants are calibrated to creep data and regression analysis is performed to convert the material constants into temperature dependent functions, $f_i(T)$ respectively. The next step, is to validate the model with additional data not used in calibration process. In the sixth step interpolation and extrapolation of the creep behavior are performed to

develop design maps. The following sections (4.0-5.0) implement the calibration procedure for the KR and Sinh models.

6.4 MODEL SELECTION AND SEGREGATION

The classic Kachanov-Rabotnov (KR) and modern Sine-hyperbolic (Sinh) CDM-based creep constitutive models are selected to perform the proposed extrapolation using disparate data. These models consist of coupled creep strain rate and damage rate equations that can be utilized to predict minimum-creep-strain-rate, creep deformation, damage, and rupture. A brief description of these models and the derived equations for extrapolation are given below. A detail step-by-step derivation of the KR and Sinh models with analytical procedures to calibrate the material constants are reported elsewhere [38,39,41].

Kachanov-Rabotnov (KR) Model

The KR model consists of a coupled creep strain rate, $\dot{\varepsilon}_{cr}$ and damage rate, $\dot{\omega}$ equations [Eqs. (93) and (94)] respectively [28,29]. The KR model can be segregated into minimum-creep-strain-rate, damage, and rupture prediction by performing mathematical manipulation as listed in Table 20 [Eqs. (95), (96), and (97) respectively]. The analytical damage can be obtained by rearranging [Eq. (93)] as shown in [Eq. (98)]. A detail step-by-step derivation of the equations is reported in the previous work of the authors [38,39].

Sine-hyperbolic (Sinh) Model

The Sinh constitutive creep strain rate, $\dot{\varepsilon}_{cr}$ replaces the power law functions in the KR model with a Sine-hyperbolic functions as shown in Table 21 [Eq. (99)] [41,**151**]. The damage rate is a modified form of Liu and Murakami with a Sine-hyperbolic function [Eq. (100)] [**146**]. Similar to KR model, the Sinh constitutive model is mathematically manipulated to segregate into minimum-

creep-strain-rate, damage, and rupture prediction as listed in Table 21 [Eqs. (101),(102), and (103)]. The Sinh analytical damage is obtained by rearranging the creep strain rate [Eq. (99)] as shown in [Eq. (104)]. A detail step-by-step derivation of the equations is reported in the previous work of the authors [38,39].

Table 20 – Kachanov-Rabotnov CDM model

Purpose	Material Constants	Equations	No.
Creep Strain Rate	A, n	$\dot{\varepsilon}_{cr} = A(\frac{\sigma}{1-\omega})^{n}$	(93)
Damage Rate	M, ψ, θ	$\dot{\omega} = \frac{M\sigma^{\psi}}{(1-\omega)^{\theta}}$	(94)
Minimum-Creep-Strain-Rate (Norton Power Law)	A, n	$\dot{\varepsilon}_{\min} = A\sigma^{n}$	(95)
Damage	θ	$\omega(t) = 1 - \left[\frac{t}{t_r}[(1-\omega_r)^{\theta+1} - 1] + 1\right]^{1/(\theta+1)}$	(96)
Rupture Prediction	M, ψ, θ	$t_r = \frac{1}{(\theta+1)\sigma^{\psi}M}$	(97)
Analytical Damage	A, n	$\omega(\dot{\varepsilon}_{cr}) = \left[(\dot{\varepsilon}_{cr}/A)^{1/n} - \sigma\right] \Big/ (\dot{\varepsilon}_{cr}/A)^{1/n}$	(98)

Table 21 – Sine-hyperbolic CDM model

Purpose	Material Constants	Equations	No.
Creep Strain Rate	B, σ_s, λ	$\dot{\varepsilon}_{cr} = B\sinh(\sigma/\sigma_s)\exp(\lambda\omega^{3/2});$ $\lambda = \ln(\dot{\varepsilon}_{final} / \dot{\varepsilon}_{\min})$	(99)
Damage Rate	Q, ϕ, χ	$\dot{\omega} = \frac{Q\left[1-\exp(-\phi)\right]}{\phi}\sinh\left(\frac{\sigma}{\sigma_t}\right)^{\chi}\exp(\phi\omega$	(100)
Minimum-Creep-Strain-Rate (McVetty Law)	B, σ_s	$\dot{\varepsilon}_{\min} = B\sinh(\sigma/\sigma_s)$	(101)
Damage	ϕ	$\omega(t) = -\frac{1}{\phi}\ln\left[1-\left[1-\exp(-\phi)\right]\frac{t}{t_r}\right]$	(102)
Rupture Prediction	Q, σ_t, χ	$t_r = \left[Q\sinh\left(\frac{\sigma}{\sigma_t}\right)^{\chi}\right]^{-1}$	(103)
Analytical Damage	B, σ_s, λ	$\omega(\dot{\varepsilon}) = \left\{\frac{1}{\lambda}\ln\left[\frac{\dot{\varepsilon}_{cr}(t)}{B\sinh(\sigma/\sigma_s)}\right]\right\}^{2/3}$	(104)

6.5 CALIBRATION

In this study, the calibration procedure is demonstrated using a disparate database of 304 stainless steel creep data. Minimum-creep-strain-rate data at five isotherms is collected from literature [41, **153-156**]. Stress-rupture data at eight isotherms is pulled from multiple sources [41,**156**,**157**,**158**]. Quintuplicate creep deformation tests at six stress levels across three isotherms are gathered from an article by Kim et al [51]. The statistics of the disparate database are summarized in Table 22.

Table 22 – Statistics of disparate creep database of 304SS

Test Type	Isotherms (°C)	Stress Range (MPa)	No. of Tests
Minimum-creep-strain-rate [41, 153-156]	566, 593, 649, 760, 816	3-250	141
Stress-rupture [41,156,157,158]	593, 649, 732, 760, 843, 899, 954	5-271	216
Creep deformation [51]	600, 650, 700	160-320	30

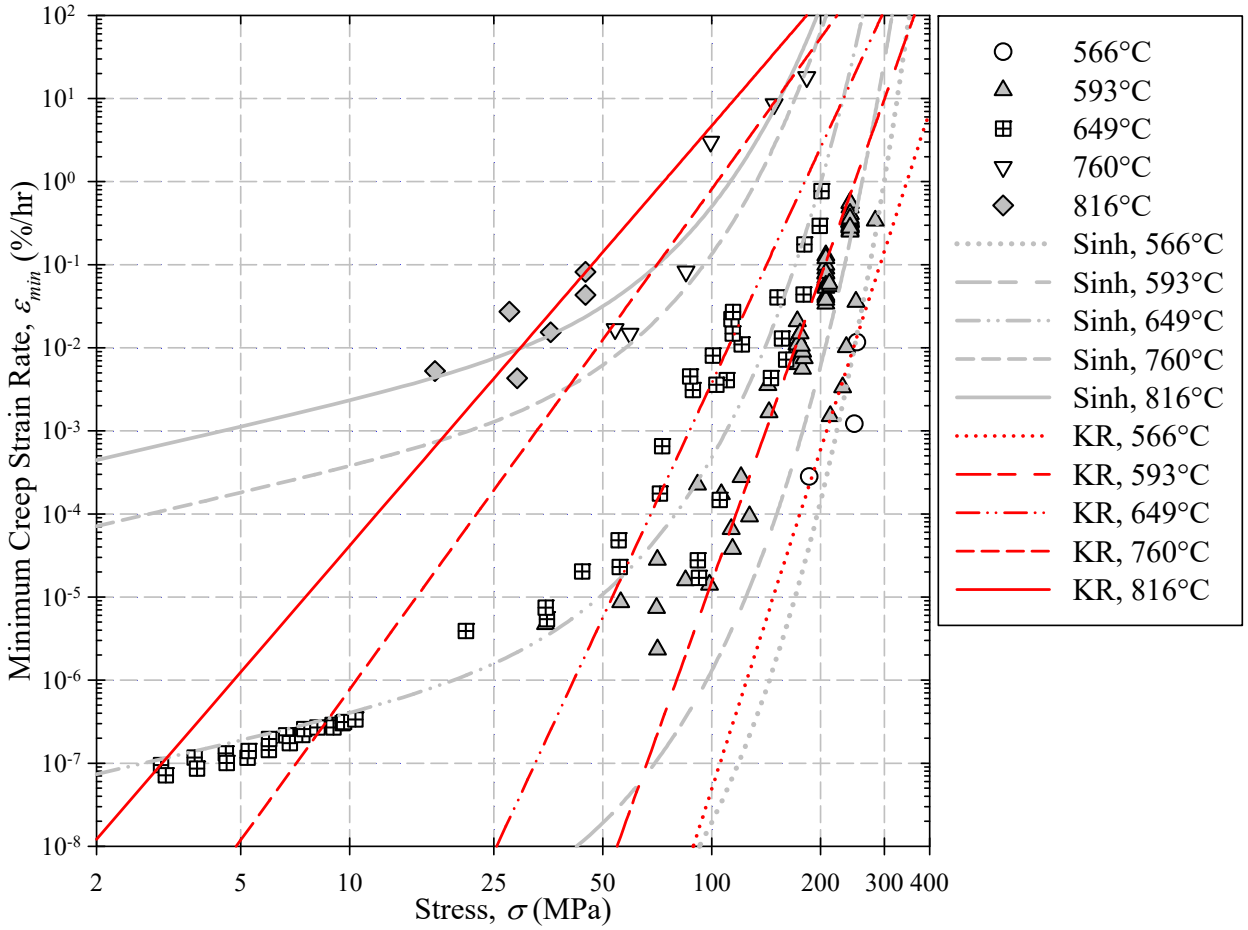

Figure 6.3 – Minimum-creep-strain-rate versus stress using the KR and Sinh models [Eq. (95)] and [Eq. (101)] respectively

6.5.1 Minimum-Creep-Strain-Rate

Minimum-creep-strain-rate predictions using KR and Sinh [Eq. (95)] and [Eq. (101)] are plotted in Figure 6.3. The calibrated material constants are listed in Table 22. Examining the data, it is observed that the 593, 649, and 760°C isotherms exhibit a sigmoidal behavior while the 566 and 816°C isotherms are linear. The KR predictions are linear on a log-log scale and are not able to model the sigmoidal behavior observed in the data; under-predicting the minimum-creep-strain-rate at low stress level. The KR model can be calibrated to fit high-stress or low-stress data but the model cannot fit both regions simultaneously. A possible solution to this problem is to use two different sets of material constants to accommodate the sigmoidal behavior; however, using a step function to switch between the material constants introduces numerical instability in simulations. Hosseini and Holdsworth reported that the assumption of a sudden change in creep mechanics for minimum-creep-strain-rate is unrealistic [**159**]. The Sinh model can model the sigmoidal behavior. In the Sinh model, the constant σ_s controls the trajectory of the bend on a log-log scale.

Table 23 – The minimum-creep-strain-rate material constants of KR and Sinh models for 304 SS

Temp. (°C)	Kachanov-Rabotnov		Sinh	
	A (%MPa^{-n} hr^{-1})	n	B (%hr^{-1})	σ_S (MPa)
566	3.82E-35	13.50	3.72E-12	11.21
593	1.10E-29	11.95	1.22E-09	11.98
649	2.75E-22	9.15	5.10E-07	13.43
760	4.81E-13	6.10	5.11E-04	16.52
816	4.54E-10	5.05	4.37E-03	18.20

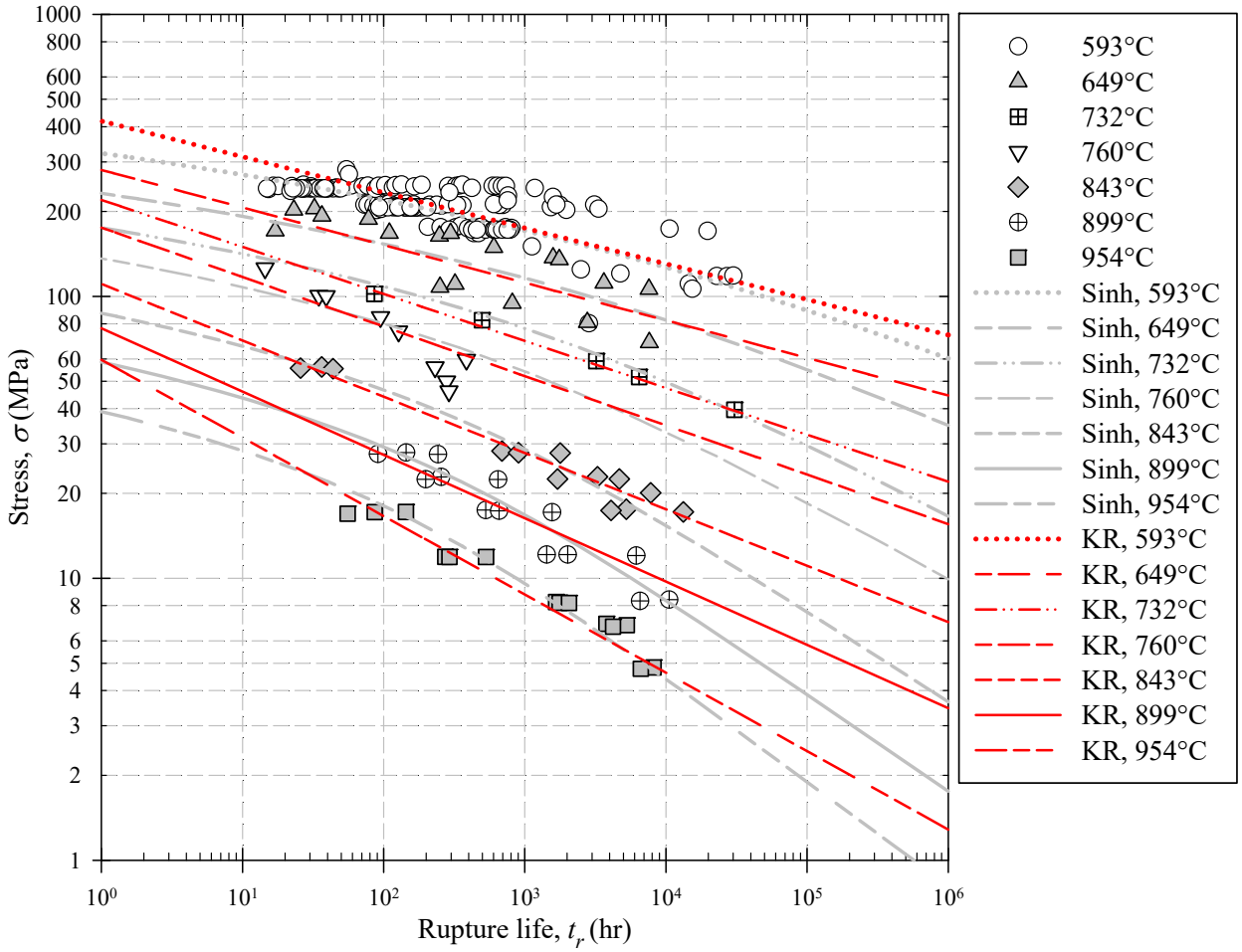

Figure 6.4 – Stress-rupture predictions using the KR and Sinh models [Eq. (97)] and [Eq. (103)] respectively

6.5.2 Stress-Rupture

Stress-rupture predictions using KR and Sinh [Eq. (97)] and [Eq. (103)] are plotted in Figure 6.4. The calibrated material constants are listed in Table 24 and Table 25 for KR and Sinh respectively. It is observed that both KR and Sinh agree with the stress-rupture data. The KR prediction is linear on a log-log scale which is not ideal considering the sigmoidal bend observed in the data. The Sinh model fits the sigmoidal bend.

Table 24 – KR stress-rupture material constants [Eq. (97)]

Temp. (°C)	M $(\mathrm{MPa}^{-\psi}\mathrm{hr}^{-1})$	θ	ψ
593	1.5E-22	12.00	7.90
649	3.9E-20	10.00	7.50
732	1.1E-15	7.00	6.00
760	2.3E-14	6.00	5.70
843	1.0E-11	5.00	5.00
899	8.0E-10	4.00	4.45
954	9.0E-08	3.50	3.60

Table 25 – Sinh stress-rupture material constants [Eq. (103)]

Temp. (°C)	Q (hr^{-1})	σ_T (MPa)	χ
593	2.6E-5	118.0	5.20
649	3.9E-5	80.0	4.60
732	9.5E-5	56.0	3.80
760	2.2E-4	45.0	3.60
843	5.5E-4	28.0	3.10
899	9.9E-4	19.0	2.90
954	1.7E-3	12.8	2.70

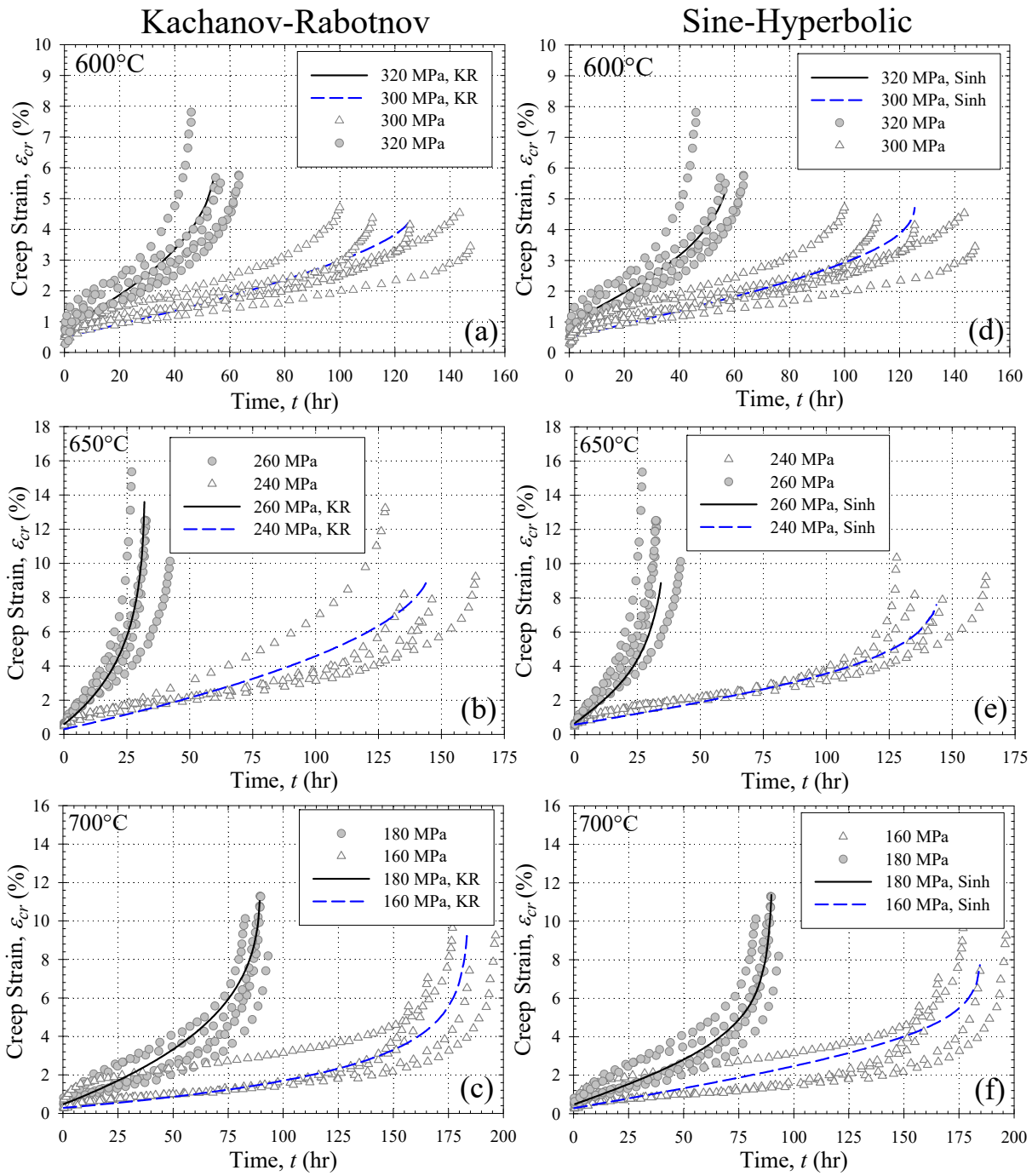

Figure 6.5 – Creep deformation simulations at 600, 650, and 700°C, (a-c) Kachanov-Rabotnov and (d-f) Sinh model [Eq. (93)] and [Eq. (99)] respectively

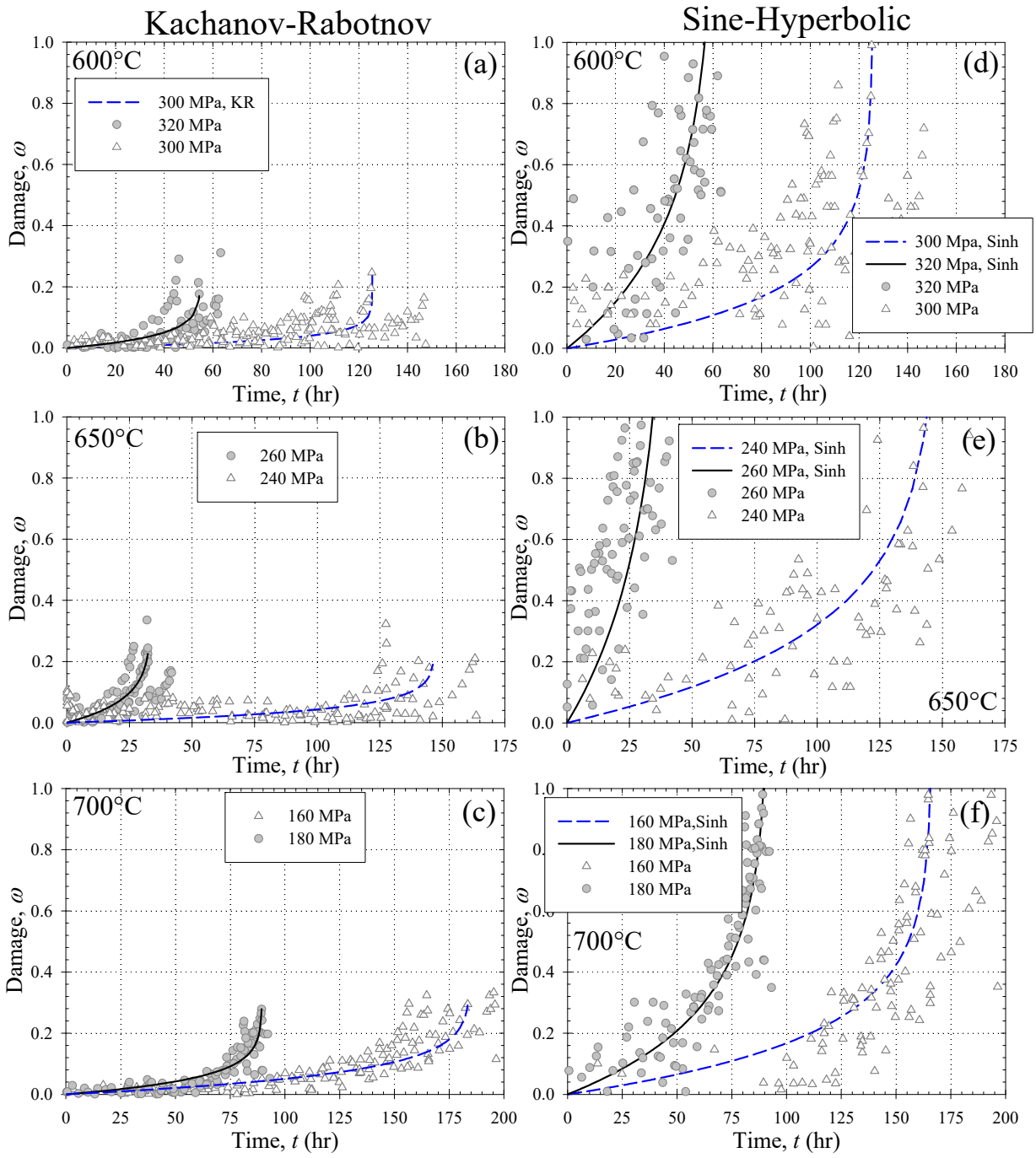

Figure 6.6 – Analytic damage evolution at 600, 650, and 700°C, (a-c) Kachanov-Rabotnov and (d-f) Sinh model [Eq (96)] and [Eqs. (102)] respectively

6.5.3 Creep Deformation and Damage

Creep deformation and damage prediction of the KR and Sinh models [Eq. (93), and (96)] and [Eq. (99), and (102)] are plotted in Figure 6.5 and Figure 6.6 respectively. The calibrated material constants are listed in Table 26 and Table 27 for KR and Sinh respectively. The material constants were obtained by fitting the creep deformation curve nearest the middle of the scatter band. Both models provide reasonable predictions of creep deformation. The accuracy of damage prediction can be broken-down to three parts: rupture life, critical damage, and the critical damage rate. Overall, the KR and Sinh models predict similar rupture lives for the given creep curves; however, the critical damage and critical damage rate are dissimilar. In the KR model, using analytical damage [Eq. (98)], the critical damage varies between 0.2 and 0.3 suggesting that rupture takes place when damage is well below unity. As a result, the critical damage rate is near-infinite at rupture. In the Sinh model, because of the material constants λ, the critical damage calculated using [Eq. (104)] is always unity.

Table 26 – KR material constants for 304SS

Temp, T (°C)	Stress, σ (MPa)	A (%MPa^{-n} hr^{-1})	n	ω_{cr}	M (MPa$^{-\psi}$ hr^{-1})	θ	ψ
700	160	6.53E-31	12.78	0.29	9.35E-11	12.5	3
	180			0.28	1.07E-10	18.5	
650	240	4.26E-33	12.98	0.17	2.69E-11	20.0	
	260			0.27	1.31E-10	12.4	
600	300	1.56E-35	13.36	0.25	9.49E-12	38.0	
	320			0.18	2.37E-11	27.0	

Table 27 – Sinh material constants for 304SS

Temp, T (°C)	Stress, σ (MPa)	B (%hr^{-1})	σ_s (MPa)	λ	ϕ	Q (hr^{-1})	σ_t (MPa)	χ
700	160	1.34E-4	27.99	4.52	5.5	1.7E-4	86.01	3
	180			4.24	3.8			
650	240	9.64E-10	13.5	3.02	3.5	1.9E-9	41.88	
	260			2.40	1.8			
600	300	2.31E-7	24.76	3.72	5.99	4.6E-7	76.00	
	320			1.93	2.62			

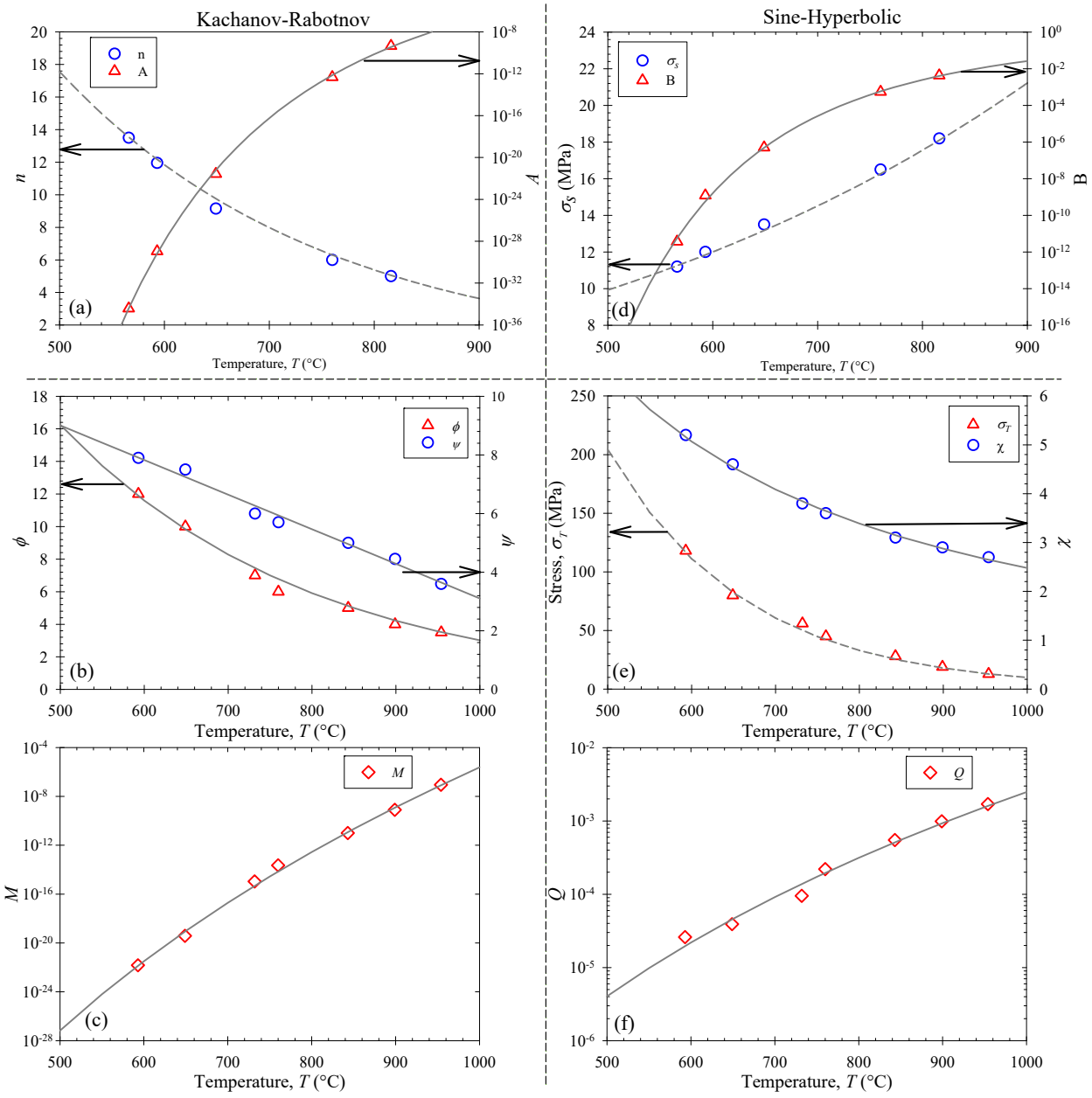

Figure 6.7 – Temperature dependence of the KR (a-c) and Sinh (d-f) material constants

6.6 REGRESSION

In the previous section, the material constants were obtained per isotherm. In this section, regression analysis is performed to convert the minimum-creep-strain rate and stress-rupture

material constants (listed in Table 23 to Table 25) into functions of temperature. Preference is given to linear, exponential, and/or power functions over polynomials due to polynomials exhibiting inflection points. Inflection points invert the concavity of the prevailing trend in data. This results in extremely inaccurate predictions [101]. The temperature-dependent functions for the material constants are listed in Table 28 along with the coefficient of determination, R^2 obtained during regression. The functions are plotted in Figure 6.7. The temperature dependent functions of the KR and Sinh model are either linear, exponential, and/or power functions and does not exhibit inflection point for a temperature range from room temperature (22°C) to 304 SS melting temperature (1400°C). The creep rupture become near infinite at room temperature and negligible at the melting temperature. The minimum-creep-strain-rate exhibit an opposite trend; it becomes negligible at room temperature and a large value at melting temperature. Constants of the KR and Sinh models (listed in Table 23 to Table 25) are fitted as a function of temperature, to facilitate prediction within and beyond the data range as shown in Table 28. The creep deformation material constants include the critical damage, ω_{cr} in KR and the material constants λ, ϕ in Sinh. It is observed in Table 26 and Table 27 that these material constants remain finite and cannot be described by a simple mathematical trend with stress and temperature. In this study, it is assumed that these material constants are stress- and temperature-independent parameters. The material constants ω_{cr} (in KR) and λ (in Sinh) control creep ductility. For conservatism, the constants are fixed to the maximum value measured in the experiments at $\omega_{cr} = 0.29$ and $\lambda = 4.5$ respectively. Please note, the ω_{cr} in Sinh is set to unity. The material constant ϕ in Sinh controls the curvature of the damage evolution [Eq. (102)]. An average $\phi = 3.0$ is selected.

Table 28 – Material constants as a function of temperature (°C)

Test Type	KR	R^2	Sinh	R^2
Minimum-creep-strain-rate	$\log(A) = -1.84E11T^{-3.534}$	0.99	$\log(B) = -5E12T^{-4.231}$	0.99
	$n = 125.92exp(-0.00394T)$	0.99	$\sigma_S = 3.84exp(0.0019T)$	0.99
Stress-rupture	$\log(M) = 31.09\ln(T) - 220.38$	0.99	$\log(Q) = 4.02\ln(T) - 30.375$	0.98
	$\theta = 87.61exp(-0.00337T)$	0.98	$\sigma_T = 4295exp(-0.0061T)$	0.99
	$\psi = -0.0118T + 14.905$	0.98	$\chi = 39293T^{-1.4}$	0.98
Creep deformation	$\omega_{cr} = 0.29$	-	$\lambda = 4.5,\ \ \phi = 3.0$	-

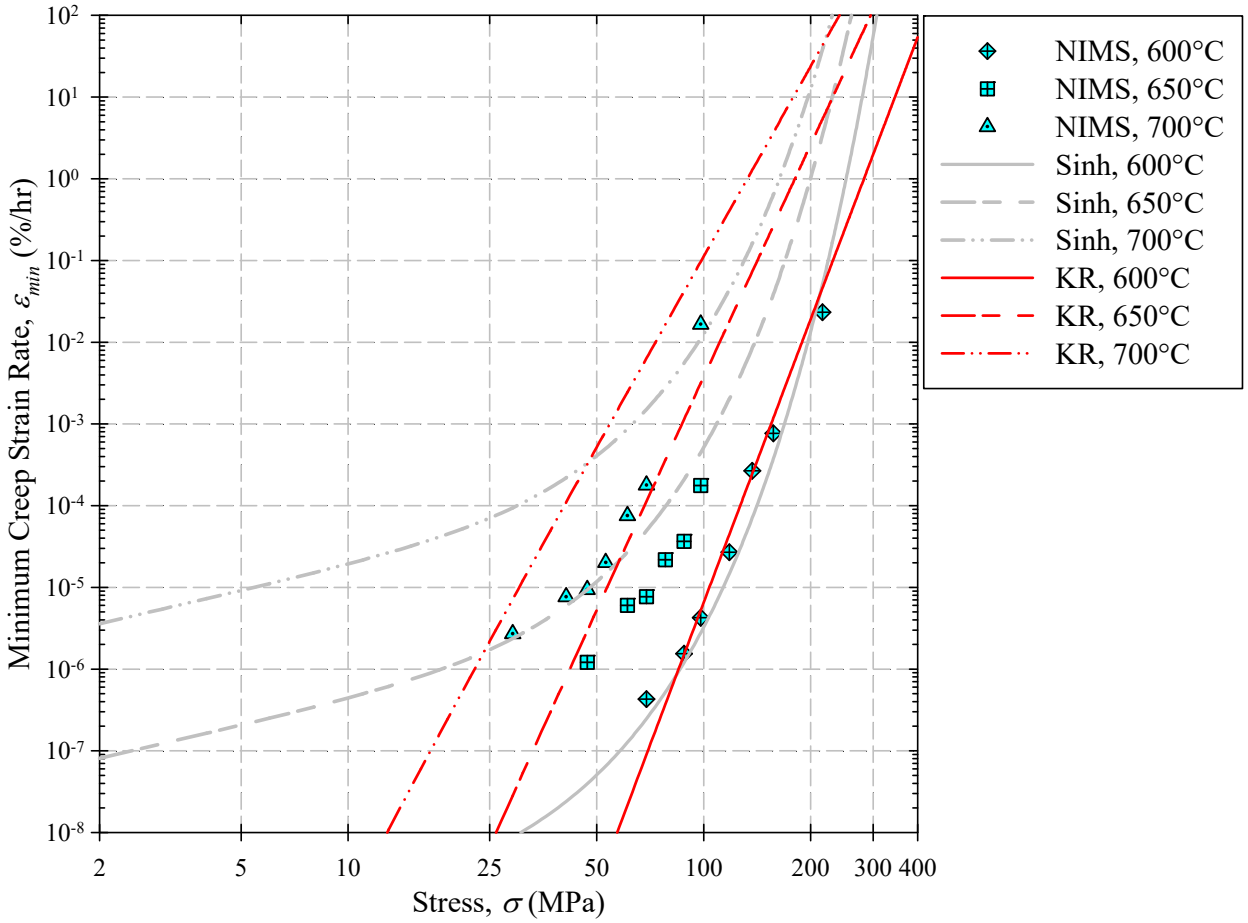

Figure 6.8 – Post-audit validation: minimum-creep-strain-rate prediction of the KR and Sinh model against NIMS data at 600, 650 , and 700◦C

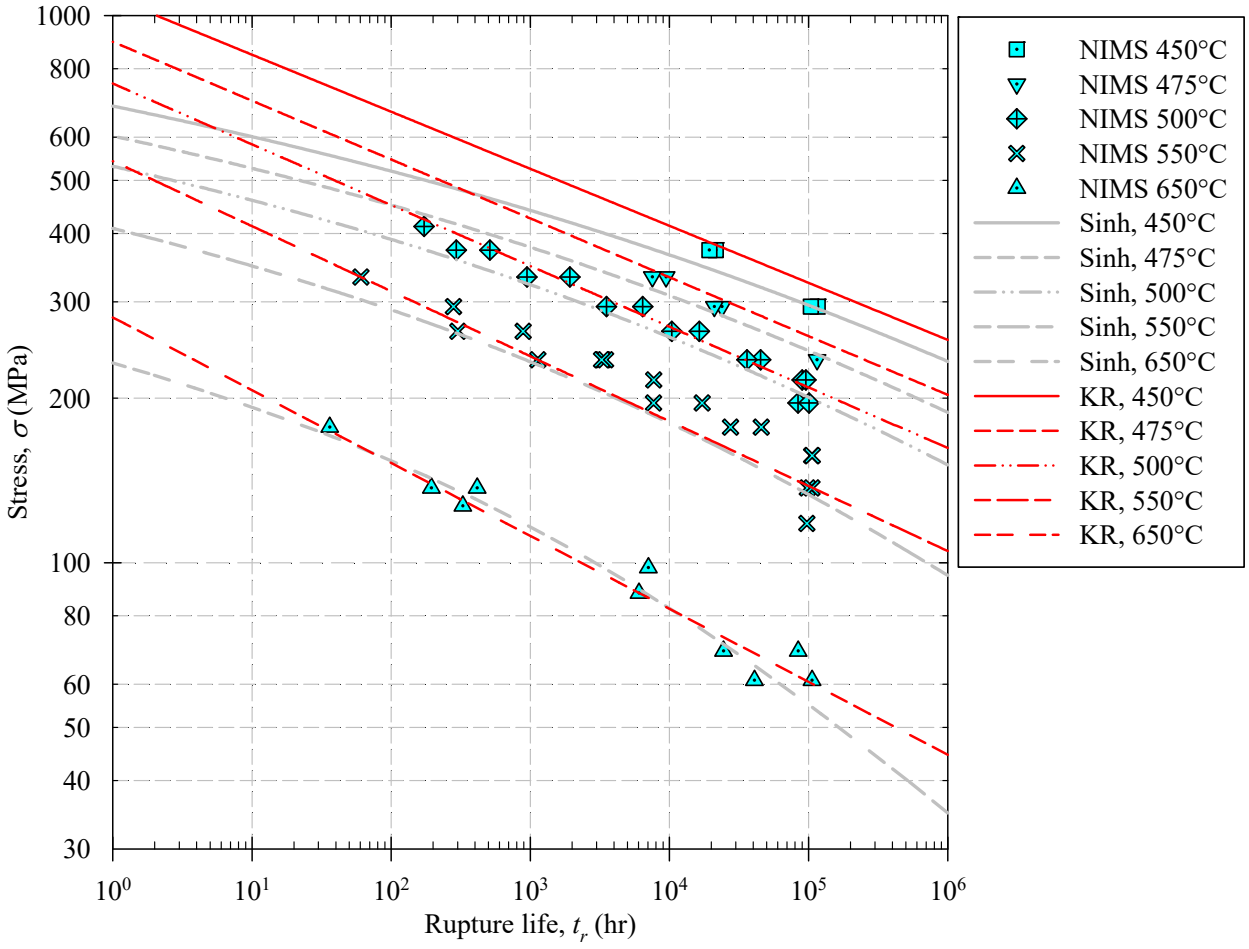

Figure 6.9 – Post-audit validation: Stress-Rupture prediction of the KR and Sinh against NIMS data at 450, 475, 500, 550, and 650°C data

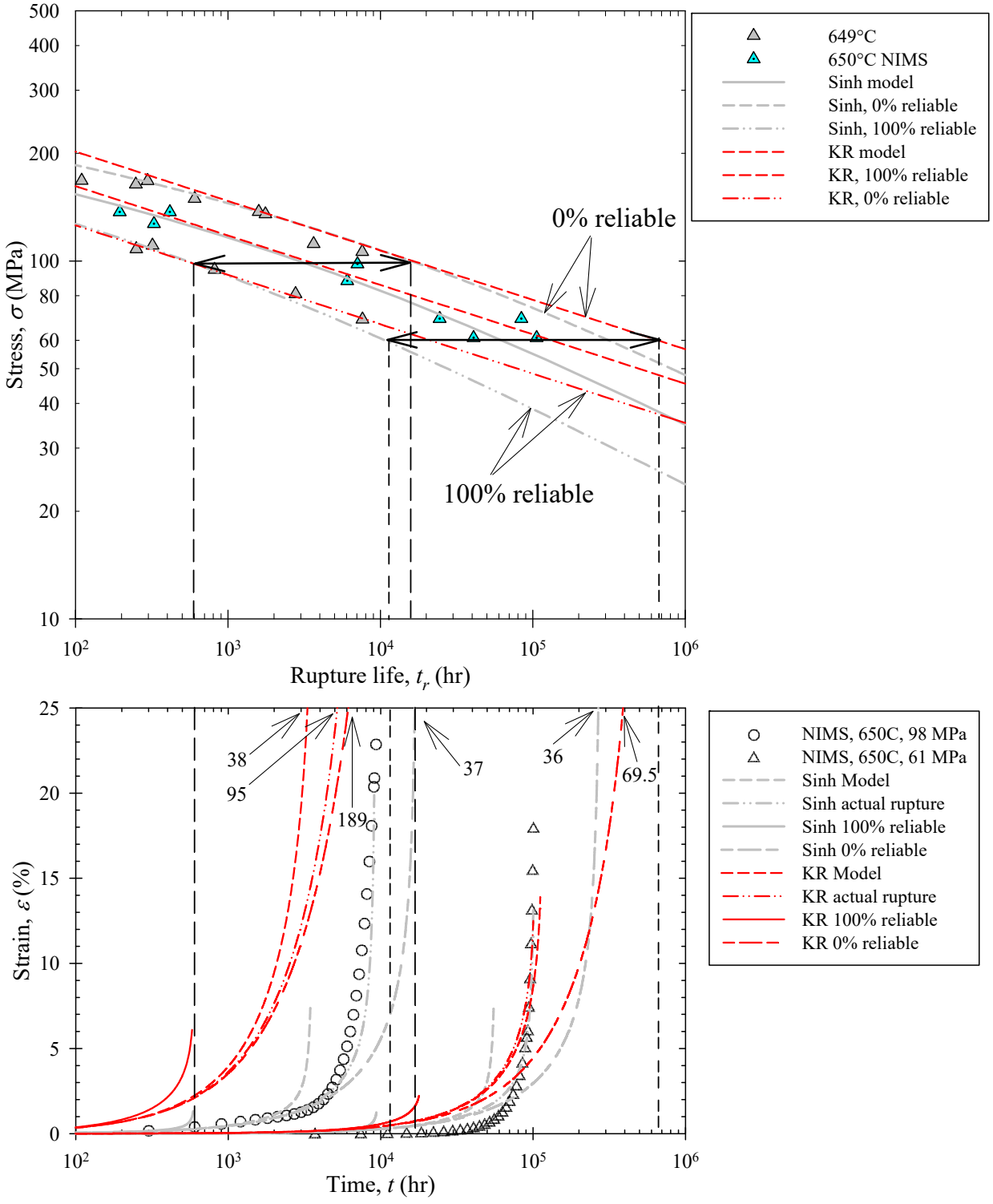

Figure 6.10 – Post-audit-validation: Creep deformation prediction of the KR and Sinh model against NIMS data at 650°C

The second objective of this study is to demonstrate the reliability of extrapolations using post-audit validation. Post-audit validation is where the pre-calibrated model is compared to additional data that was not used during calibration. Additional creep data for 304SS is gathered from the Japan National Institute of Materials Science (NIMS) material database [5]. Minimum-creep-strain rate data at three isotherms, stress-rupture data at five isotherms, and long-term creep deformation curves at 650°C are collected. The statistics of the disparate database are summarized in Table 29.

Table 29 – Statistics of the post-audit validation data from NIMS [56]

Data type	Isotherms (°C)	Stress range (MPa)	Data points
Minimum-creep-strain-rate	3	29-216	20
Stress-Rupture	5	61 - 412	52
Creep deformation	1	61, 98	2 set

The NIMS minimum-creep-strain-rate data is compared to KR and Sinh simulations plotted in Figure 6.8. It is observed that the KR and Sinh simulations at 600 and 650°C agree with the NIMS data; however, the predictions at 700°C do not agree with the NIMS data. This is because the 649°C isotherm (used during calibration) overlaps with the 700°C isotherms from NIMS. The cause of this overlap could be due to a) the limited number of tests performed at 700°C not capturing the scatter band expected at 700°C, b) differences in the chemical composition and thermomechanical processing and form of the material between the two data sources, (c) differences in the equipment, test procedure, and geometry between the two data sources.

The NIMS stress-rupture data is compared to KR and Sinh simulations shown in Figure 6.9. Both the KR and Sinh model extrapolation agree with the NIMS data. However, there is difference between the KR and Sinh prediction curves. The difference is significant for a creep life below 10^2 hrs and above 10^5 hrs. In comparison with the KR prediction, the Sinh prediction exhibit

conservatism over the KR. This is due to the sigmoidal bend of the Sinh model. Note, the stress-rupture prediction of the KR and Sinh model fit the NIMS data; and unable to fit minimum-creep-strain-rate data. This is due to the expected high variability of minimum-creep-strain-rate data compared to rupture life, leading to poor fit of minimum-creep-strain-rate data.

The NIMS creep deformation curves at 650°C are compared to KR and Sinh simulations shown in Figure 6.10. In CDM models, ductility and deformation are dependent on the predicted rupture life, with ductility increasing with rupture life. Stress-rupture data exhibits uncertainty, where at low stress, rupture life may span across decades as illustrated in Figure a at 650°C. It would be unwise to extrapolate without considering the uncertainty of stress-rupture and its effect on creep deformation. In this study, creep deformation predictions are made at four rupture points of interest. The four rupture points are:

- model predicted rupture. The calibrated rupture predictions [Eq. (97)] and [Eq. (103)] are applied. These predictions take an average path through the stress-rupture data and can be consider 50% reliable.

- 100% reliability rupture. The model predictions are shifted downwards to pass through the shortest experimental rupture-life. These are considered 100% reliable predictions because the actual rupture life is longer than the predicted life. These predictions are extremely conservative and are not ideal for design.

- 0% reliability rupture. The model predictions are shifted upwards to pass through the longest experimental rupture-life. These are considered 0% reliable predictions because the actual rupture life is shorter than the predicted life. These predictions are extremely non-conservative and are not ideal for design.

- actual rupture. The actual rupture life of each creep deformation curve is input into the CDM models. This gives the opportunity to eliminate the specimen-specific uncertainty of rupture.

Long-term creep deformation curves conducted at 61 and 98 MPa with rupture lives of 100491 and 9064 hrs and final strain of 23% and 18% respectively are collected. Creep deformation is predicted for these two tests using the four rupture points as shown in Figure b. Note, in order to plot both creep deformation curves together, time set to a log-scale. This deformation band facilitates the exercise for a certain percentage of reliability. The KR and Sinh prediction at four rupture points are:

- model predicted rupture: The KR model exhibit a good fit at 61 MPa and over predicting at 98 MPa. The Sinh model under predicting the deformation at both stress level.

- 100% and 0% reliability rupture: The 100% and 0% reliability rupture of the KR at 98 MPa develops a rupture-life range of 578-18087 hrs and final strain ranging from 6-189%. At 61 MPa, the range of rupture-life is 17872-558490 hrs and final stain is of 2.2237-69%. In comparison to the experimental data variation observed in Figure , the maximum variation in rupture life is of 48 hrs (100-148 hrs, at 600°C, and 300 MPa) and maximum variation in final strain is of 5% (10.12-15.35%, at 650°C, 260 MPa). This suggest that, a large variation may be observed for rupture life at low stress, and a large variation may be observed for final strain at high stress. It is reasonable to expect larger variation at longer rupture life, however, a final strain variation observed in KR model of 183% is astronomical, and unrealistic for 304 SS.

The Sinh 100% and 0% reliability rupture develops a rupture life range of 98 hrs (588-17287) with a reasonable final strain range of (1.3-37.91%). At 61 MPa, the range of rupture life is 9374-275710 hrs, with final strain ranging from 1.2477-36.66%.

- Actual rupture: The KR exhibit a good fit at 61 MPa, however, a poor fit at 98 MPa. The final strain at 98 MPa is peaking unrealistic 95% elongation before rupture. The Sinh exhibit good fit at both 61 and 98 MPa stress level with final strain of 20% and 14% respectively.

It is observed that for 98 MPa, KR model is over predicting the deformation; the final strain is peaking 100% elongation before rupture (much higher than the actual). The Sinh exhibit a superior behavior; matching the data for actual rupture. At 61 MPa, the KR and Sinh both model performs considerably well. Overall, the Sinh is more reliable than the KR.

6.7 Creep Design Maps

The third objective of this study is to illustrate a variety of creep design maps and compare the interpolation and extrapolation ability of CDM models. An algorithm is developed to generate creep design maps for the minimum-creep-strain-rate, stress-rupture, creep deformation, and damage. Using these maps, the KR and Sinh models are compared.

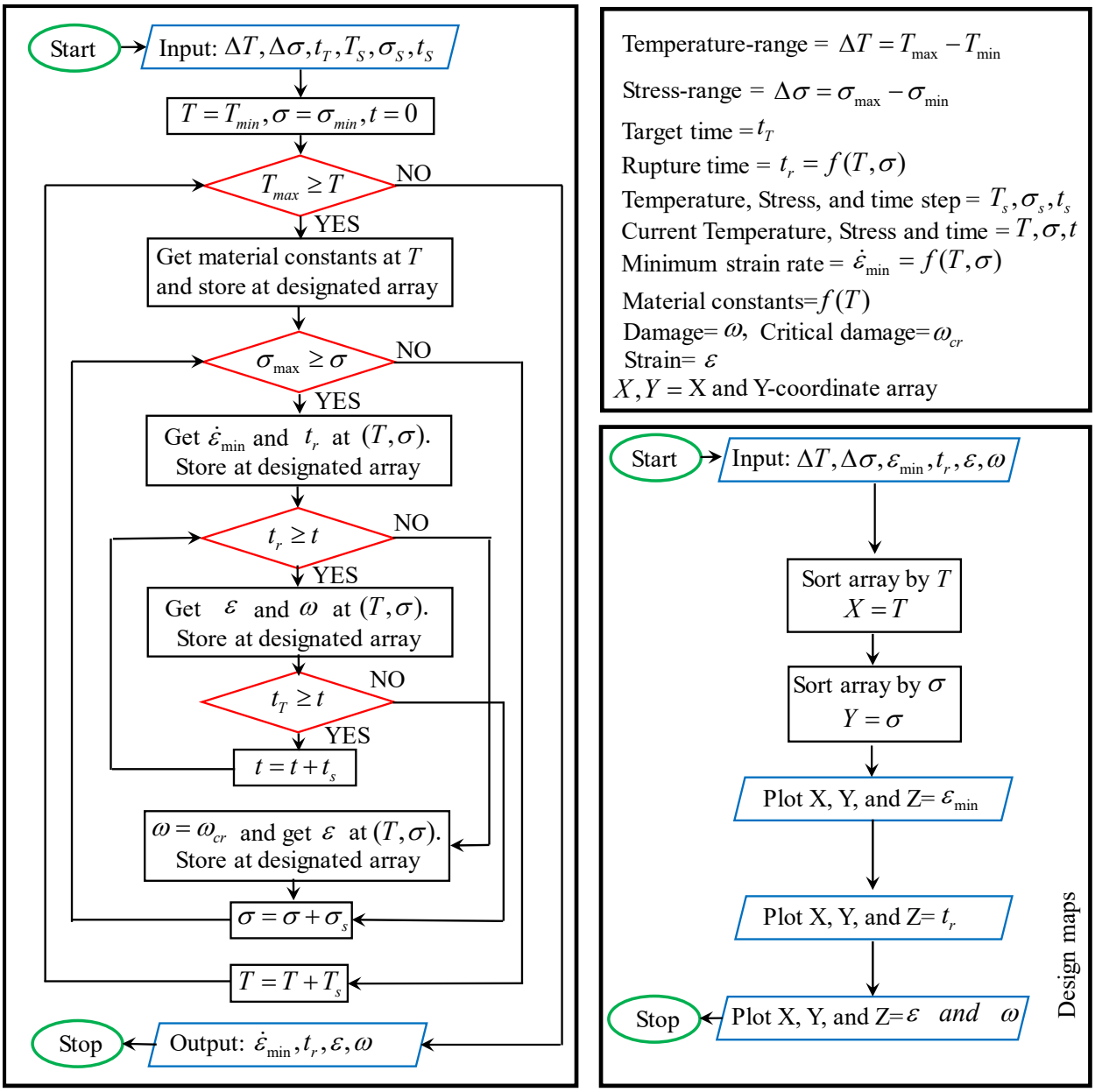

Step 1: Perform interpolation and extrapolation **Step 2: Plot design maps**

Figure 6.11 – Algorithm to generate creep design maps

6.7.1 Algorithm

To generate these creep design maps, a mathematical algorithm is developed in MATLAB to perform interpolation and extrapolation at a target time for a given range of stress and temperature as outlined in Figure 6.11. The algorithm is divided into two steps: (Step 1) to perform the interpolation and extrapolation and (Step 2) to plot the creep design maps. In the first step the temperature-range ΔT, stress-range $\Delta\sigma$, target time t_T, and the temperature step, stress step, and time step increment (T_s, σ_s, t_s) are the input. The algorithm uses the regressed temperature-dependent function to determine the material constants at any given temperature. The material constants are plugged into the constitutive model to determine the variables of interest (minimum-creep-stain-rate, rupture, deformation and damage) at the target time over the given stress and temperature range. In the second step, the variables of interest are plotted to create creep design maps by following the steps shown in Figure 6.11 (step 2). Using the algorithm, the following creep design maps are generated.

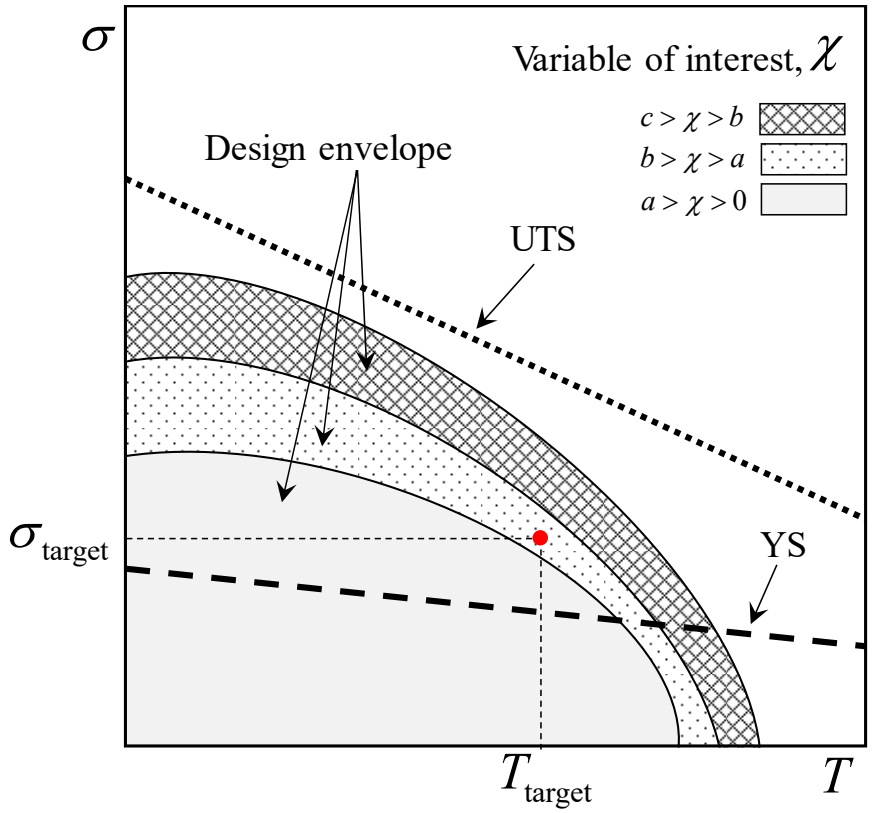

Figure 6.12 – Illustration of design map. The map includes lines indicating the tensile properties of the material and a shaded area that represent the design envelope where stress and temperature are below the user selected critical value.

6.7.2 Reading a Design Map and Application

The design maps introduced in this study are complicated. An illustration of a generic design map is provided in Figure 6.12. The design maps are contours plots. Temperature is on the x axis and stress is on the y axis. The variable of interest (minimum-creep-strain-rate, rupture life, strain, damage, etc.) is plotted as a contour value, z (indicated by color). The user can select the target temperature and stress for their design and identify the contour value. The contour value represents the predicted variable of interest. The tensile properties of the material are plotted as lines on the design map so that the user can identify the onset of rate-independent plasticity and ductile failure.

The user can also identify and plot a line represent a ***critical value*** for the variable of interest. By doing so, the user can establish a ***design envelope*** of stresses and temperatures within which a design is safe.

A design and maintenance engineer can apply design maps in two ways. In the deterministic approach, the design engineer uses the design map as-is to predict behavior and establish the design envelope. The engineer may choose to apply a safety factor to the critical value line to accommodate both the uncertainty of design and materials. In the probabilistic approach, the engineer would need to modify the algorithm and add probabilistic functions (such as Monte-Carlo methods, blah, etc.) for a more quantitative assessment of uncertainty. The outcome of the modified algorithm would be a probability distribution of the variable of interest. To plot the results, the engineer needs to establish what is the acceptable probability and plot it or develop live plots where the acceptable probability can be varied, and the design maps update to reflect the engineers' selection. For brevity, in this study only the deterministic approach is considered.

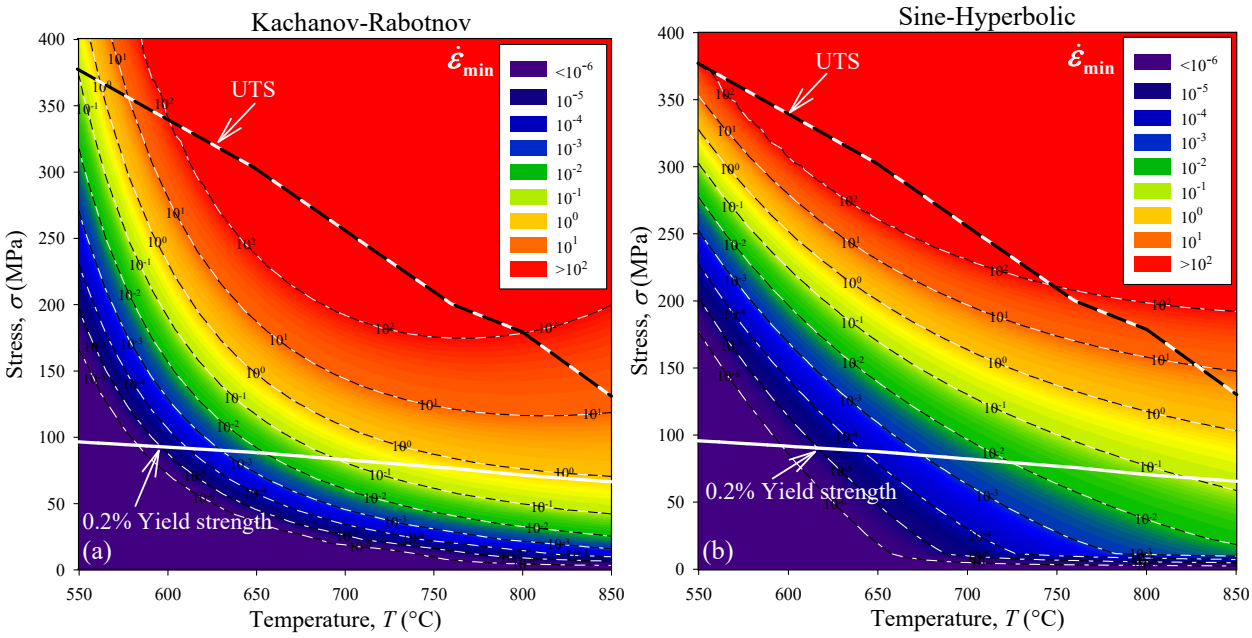

Figure 6.13 – Minimum-creep-strain-rate design maps for the (a) KR [Eq. (95)] and (b) Sinh [Eq. (101)] models respectively. The white lines indicate the 0.2% yield strength and the bold dashed line represents the ultimate tensile strength (UTS).

6.7.3 Minimum-Creep-Strain-Rate Design Map

In this section the design maps developed for minimum-creep-strain-rate are discussed. A parametric simulation is performed for a temperature ranging from 550 to 850°C and stress from zero to 400 MPa as shown in Figure 6.13. It is observed that the Sinh model is more conservative (predicts higher minimum-creep-strain-rate) than the KR model in the low-stress region (below 30 MPa) and high-stress region (above 250 MPa) due to the sigmoidal bend in of the Sinh model Mcvetty law. The KR model is more conservative than the Sinh model at stress ranging from 50 to 250 MPa. The KR model exhibits an unrealistic behavior (inflection point) at high temperature (>750°C) and high stress ($220 > \sigma > 170$ MPa). This is due to the evolution of the minimum-cree-strain-rate constant A and n. The material constat A and n, follows an temperature dependent power and exponentioal function respectively; does not exhibit inflection point. However, the

constants follows an opposite trend of each other; with the increase of temperature the A increase while n decrease. The combined effect of the two function ($\varepsilon_{\min} = A(T)\sigma^{n(T)}$) may lead to inflection status over wide range of temperature application. At a given stress, over the temperature range of 22°C to 1400°C, there exist a inflection point in the KR minimum-creep-strain-rate curve. The point of inflection varies with applied stress, and it is observed as low stress as 35 MPa (inflection observed at 1100°C). Increasing the applied stress reduces the temperature at which the inflection takes place. At 400 MPa the infectio takes place around 700°C. The Sinh model exhibits inflection point at 35 MPa (inflection observed at 1300°C) and at 400 MPa the inflection occures at 700°C; a stable behavior for a wide stress and temperature range. An analytic solution to determine the inflection point is by taking a first derivative of the minimum-creep-strain-rate equation and solving for zero ($d(\varepsilon_{\min})/dT = d(A(T)\sigma^{n(T)})/dT = 0$). In our cases, the temperature-dependent functions are complicated necessitiating numerical optimization to determine the inflcetions as shown in Figure 6.14. Expected inflection for both model over a stress range of 0 to 400 MPa for a temperature ranging from 600 to 1400°C illustrates the reliable application zone (the area below the inflection lines). It is observed that a service condition: a) below YS is free of inflection for both model, b) above YS and below UTS may exhibit inflection for the KR model at a stress range from 70 to 200 MPa for a temperature ranging from 680 to 860°C. The Sinh model inflection may occur above UTS, sugesting superioroty of the Sinh mdoel, does not exhibit inflection upto UTS. c) an operaitng condition below 650°C is free of inflection in either casses. Overall, the Sinh model is more reliable than the KR model to design for an operating stress above 0.2% yield strength and below UTS.

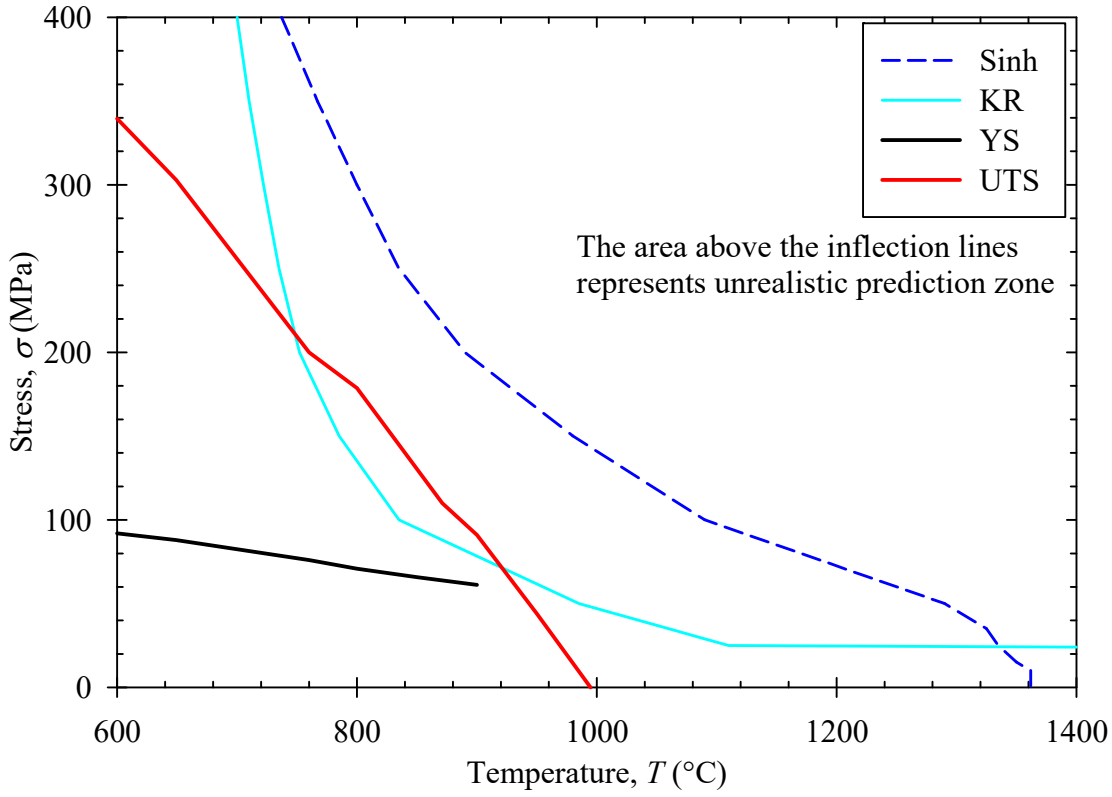

Figure 6.14 – Evolution of inflection status of the KR and Sinh model. The area above the inflection line represents the unrealistic prediction zone. The Sinh is more flexible compared to KR model.

The minimum-creep-strain-rate design map can be can used to estimate the rupture life (when the rupture design map is not available) using the Monkman-Grant model [160]. Furthermore, the minimum-creep-strain-rate design map can be used to determine the onset of tertiary creep regime using the Theta projection model [161]. The onset of tertiary creep represents the time at which appreciable creep damage begins to accumulate and grow within the material. Thus, onset design map derived from the minimum-creep-strain-rate can be used as an initial estimate in of damage-tolerant safe-life design approach. In the safe-life approach, no detectable damage is allowed in

design; rather, the component is retired after a designated duration of service. The onset of tertiary creep would be an ideal duration for the removal of components from service under the safe-life approach.

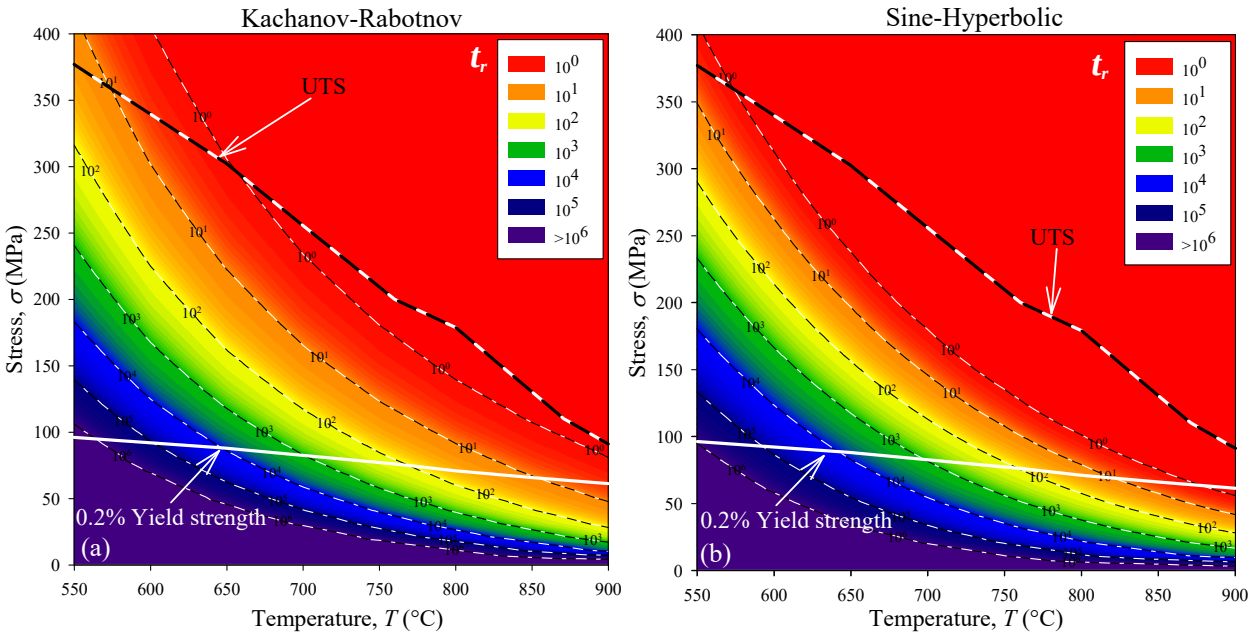

Figure 6.15 – Creep rupture design maps for the (a) KR [Eq. (97)] and (b) Sinh [Eq. (103)] models respectively. The white lines indicate the 0.2% yield strength and the bold dashed line represents the ultimate tensile strength (UTS).

6.7.4 Stress-Rupture Design Maps

In this section the creep design maps developed for stress-rupture are discussed. Parametric simulations are performed to produce stress-rupture design maps Similar approaches reported in minimum-creep-strain-rate section is exercised to develop creep rupture design maps for both KR and Sinh model as shown in Figure 6.15. It is observed that the KR and Sinh rupture predictions are similar for a life longer than 10^2 hrs and notably different for life shorter than $<10^2$ hrs. This deviation is due to the linear behavior of the KR model [Eq. (97)] predicting longer rupture lives

than the sigmoidal behavior of the Sinh model as observed in Figure 6.3 and Figure 6.8. The KR model predicts creep life above UTS for a stress range above 300 MPa and below 650°C and Sinh model predicts creep life above 350 MPa and below 600°C. This could be due to the effective creep activation temperature. In this case, it seems that the creep activation temperature for the KR and Sinh is 650°C and 600°C respectively, that is $0.46T_m$ and $0.42T_m$ of the melting temperature of 1400°C. This suggest that creep damage is no longer a dominant mechanism below this temperature. The stress-rupture design maps can be used as a tool in safe-life design. A engineer can easily apply a safety-factor to the stress-rupture design maps and proceed with design.

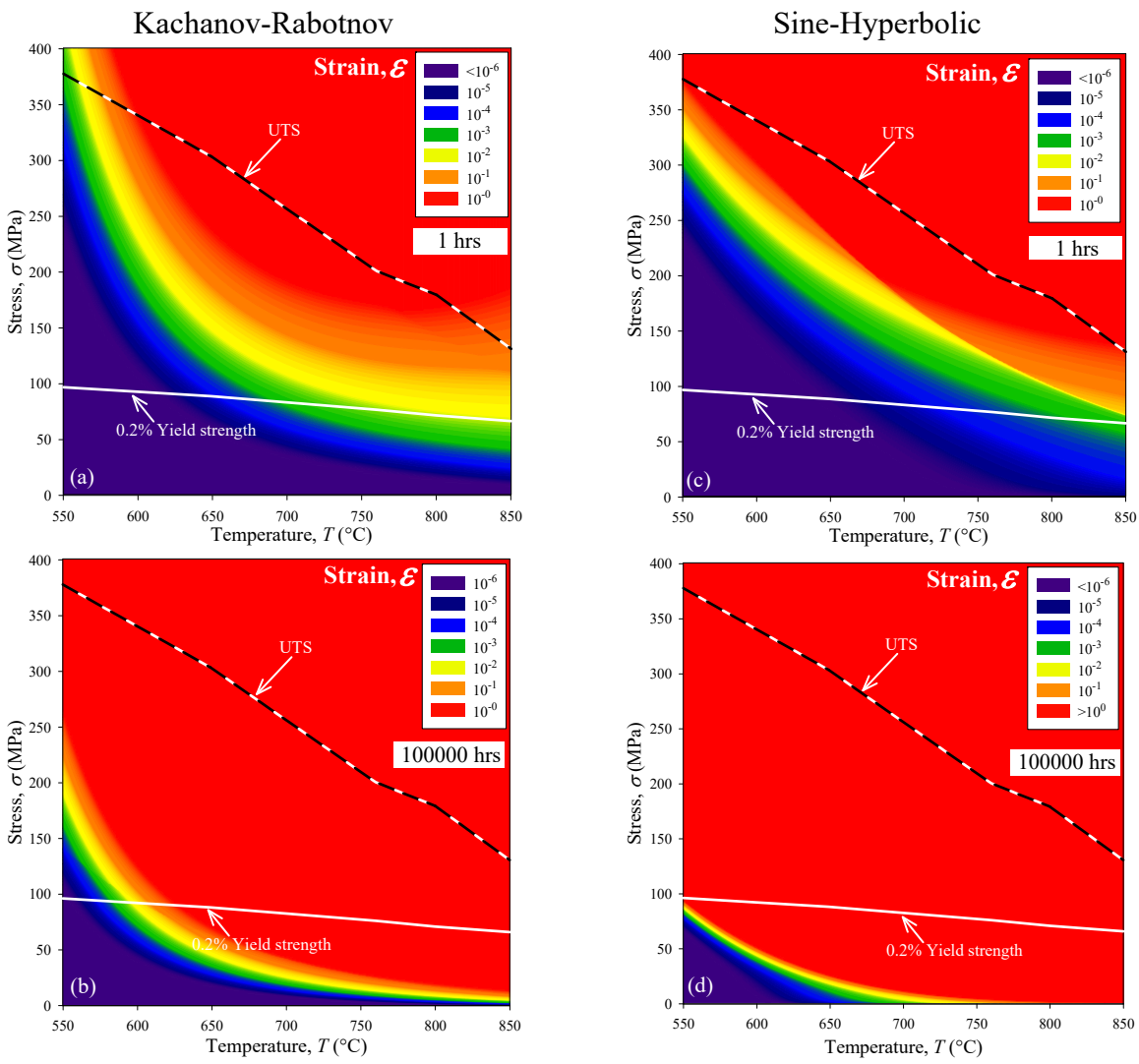

Figure 6.16 – Creep deformation design maps for the (a-b) KR [Eq. (93)] and (c-d) Sinh [Eq. (99)] models respectively. The white lines indicate the 0.2% yield strength and the bold dashed line represents the ultimate tensile strength.

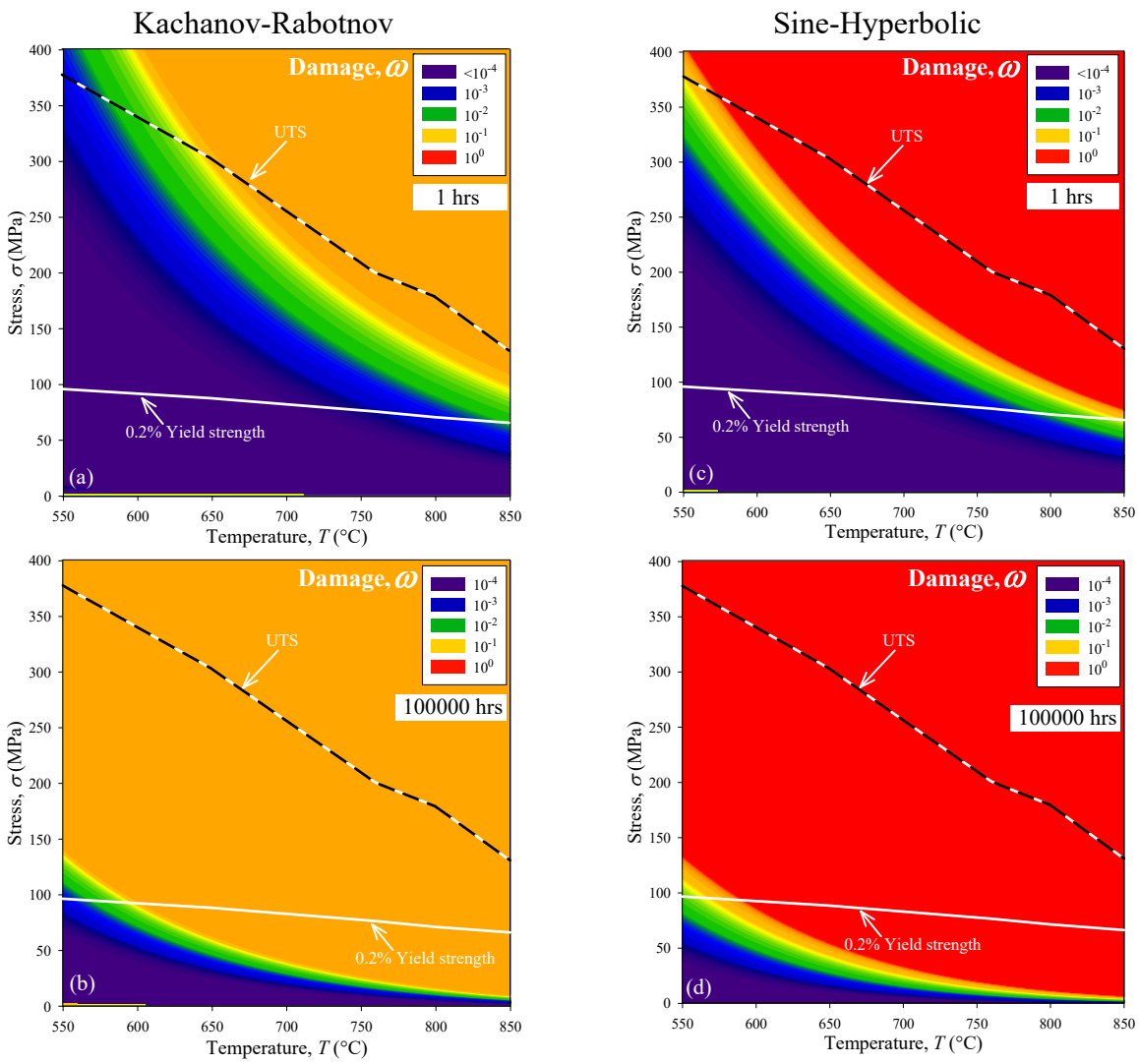

Figure 6.17 – Damage design maps for the (a-b) KR [Eq. (96)] and (c-d) Sinh [Eq. (102)] models respectively The white lines indicates the 0.2% yield strength and the bold dashed line represents the ultimate tensile strength.

6.7.5 Creep Deformation and Damage Design Maps

Parametric simulations are performed to produce creep deformation and damage design maps for the KR and Sinh as shown in Figure 6.16 and Figure 6.17 respectively. The design envelope is consider anything below the critical strain and/or damage. The engineer must decide what is considered a critical value. Stresses and temperatures below the critical value are allowable. Those above are not. For this study, the critical strain set to unity and the critical damage for KR and Sinh are set to 0.29 and unity respectively. The engineer can also select the target time at which to generate design maps. In this study, maps are plotted at two target times: 1 and 100000 hrs. The former was selected because it shows the stratification of the contour bands and allows a dicussion of creep-dominant versus ductile failure. The later was selected because it represents the useful design life of hot path components in both industrial gas and steam turbines. In equivalent base operating hours, 100000 hr conincides with the second major inspection in many fleets.

In the 1 hr design maps, the contour bands are easy to perceive. The relevent creep deformation and damage maps are Figure 6.16a,c and Figure 6.17a,c respectively. The contour bands appear similar to exponential decay functions. As the operating temperature increases, the contour bands collapse to zero allowable stress at some critical temperature. The KR and Sinh predictions are distinct; with the bands in the Sinh maps being more grouped together and appearing to collapse to zero allowable stress at a lower critical temperature. The onset of ductile failure is plotted using the ultimate tensile strength (a bold dashed line). In both KR and Sinh, there are regions where creep failure will occur before ductile failure. The shape and intercepts of these regions are distinct. Ductile failure becomes dominant at lower temperature as indicated by the UTS line passing though contours where the critical values are not exceed.

In the 100000 hr design maps, the design envelope collapses with the creep failure region increasing dramatically in size while become more similar in shape across the various maps. The relevent creep deformation and damage maps are Figure 6.16b,d and Figure 6.17b,d respectively. The engineer has a much smaller design envelope to work in if a design-life of 100,000 hours is to be achieved. It is observed that the critical temperature has decreased dramatically. The lowest critical temperature appears in the creep deformation map of Sinh at 750°C. The map suggests a design-life of 100000 hrs is not viable for 304SS at temperatures greater than 750°C. Overall, the Sinh model is more conservative when compared to KR.

These creep deformation and damage maps can be used in damage-tolerant design. Damage-tolerant design is where damage is allowed to develop within a component up to a critical value. Damage is quntified using one and a combination of several damage parameters that are obtained using destructive (small sample incised from in-service component) or non-destructive evaluation methods (in-service component is examined during major inspection) [162]. During the design phase, high-fidelity simulations are often employed in lieu of physical data.

6.8 SUMMARY

In this study it is proved that integrating disparate creep data into the calibration of creep model can lead to more reliable extrapolation. The first objective of this study was to provide a detailed procedure for calibrating CDM models using disparate data. The Kachanov-Rabotnov and a Sine-Hyperbolic CDM based model are calibrated against disparate minimum-creep-strain-rate, stress-rupture, and creep-deformation data as described in “5.0 Calibration” section.

The second objective was to demonstrate the reliability of extrapolation using post-audit validation of the calibrated model. This objective was completed by comparing the extrapolation of the KR and Sinh model with additional creep data that was not used in the calibration. It is observed that

both KR and Sinh extrapolation agree with the stress-rupture data. The minimum-creep-strain-rate extrapolations are agreeing at 600°C, but does not agree at 650 and 700°C with the data. Expected high variability in minimum-creep-strain-rate, data overlap, testing metadata, and lack of experimental data may have caused the deviation. Extrapolation of creep deformation at four rupture points developing a reliability band from 0 to 100% agree with experimental data up to 10^5 hrs.

The third objective was to illustrate a variety of creep design maps and demonstrate that the interpolation and extrapolation ability of CDM models can be compared graphically using the creep design maps. This objective was completed by devolving a MATLAB algorithm that perform instant interpolation and extrapolation to generate design maps for minimum-creep-strain-rate, stress-rupture, creep deformation, and damage.

Future Work

Future work should focus on the integration of probabilistic methods in the development of the design maps. Maps that take into consideration the prior service history. The current design maps are applicable for brand new parts. The maps are not appropriate for an existing part in power plant where the operating condition during service change (i.e. when a plant is switched between base-load, load-following, and/or peak-load operations). In addition, the approach can be expanded for non-isothermal and -isostress conditions (i.e creep-fatigue").

Chapter 7: Multiaxiality Representative Functions

7.1 INTRODUCTION

It has been experimentally observed that the state of stress greatly influences the creep damage evolution and rupture of alloys [96]. When superalloys are subject to creep conditions, in the vicinity of the flaw/design discontinuities, a multi-axial time-dependent stress-redistribution greatly influences the inelastic deformation and damage field, enhancing the notch effect [97]. This relationship can lead to notch strengthening or weakening of a material in the vicinity of a stress concentration. A multiaxial state of stress can be produce in the laboratory by applying a tensile load to a notched bar [98]. Towards an accurate assess of creep behavior in actual components it is necessary to incorporate multiaxiality into constitutive equations. There are many approaches available in the literature to accommodate multiaxial ductility and rupture [98-100]. The ASME B&PV III, French RCC-MR, and British R5 recommends different phenomenological approaches to notched creep. To predict the rupture time, a common practice is to replace the applied stress with a representative stress that is a function of principal stress, hydrostatic stress, and von mises stress, σ_1, σ_m, and σ_{VM} respectively. Similarly, to predict the multiaxial ductility, the multiaxial final strain is defined as a function of uniaxial final strain and these stresses [99]. However, a clear guideline is missing in selection of representative stress to accommodate multiaxiality in constitutive relationships.

In this chapter, multiaxial stress functions adopted by ASME B&PV III, French RCC-MR and additional five popular functions are compared using rupture surface criterion. Flexibility to predict complex rupture surface, ability to avoid divide by zero error and imaginary number error under zero stress, $(0,0,0)$ and/or equi-tensil-compressive stress, $(\sigma,-\sigma,0)$ conditions are

analyzed for each functions to determine the most suitable function that is applicable for complete description of multiaxial stress states. Relationships between the multiaxiality functions are derived with special and limiting conditions for each function discussed in details. The incompressibility criteria of the functions are analyzed to develop constraints for material parameters to avoid creep under compression. Finally, a guideline to the selection of the appropriate representative stress function and the associated incompressibility condition is presented.

Multiaxial representative functions can be broadly classified in three groups as multiaxial rupture, multiaxial ductility, and skeletal point stress and strain functions. Several mathematical functions are available and each functions are proved as the most suitable for at least one material over a specific temperature condition. However, not a single function is universally applicable to all material at every temperature condition. Most suitable function can be determined from the available functions, or by exploiting functional relationship between existing functions, or by developing a new function. Example of exploiting functional relationships between creep models is reported elsewhere [101]. Some widely used multiaxial rupture, multiaxial ductility are stated below. Scope and limitation of skeletal point approach is discussed.

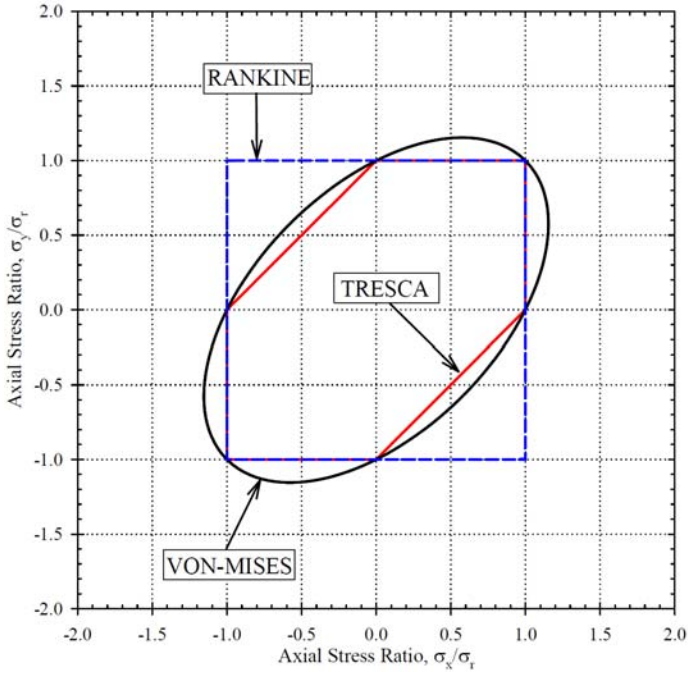

Figure 7.1 – Classic representative stress rupture surfaces

7.2 MULTIAXIAL REPRESENTATIVE FUNCTIONS

7.2.1 Multiaxial Creep Rupture

Under multiaxial stress condition, rupture time depends on temperature, T and representative stress σ_{rep} as defined in

$$t_r = F(\sigma_{rep}, T) \tag{105}$$

There are many representative stress form available in the literature. The classic representative stress function is the Rankine, Tresca, and Von-mises rupture criterion as depicted in Figure . The classic models do not include any material parameter such that the rupture criteria can be evaluated directly from the principal stresses. Rankine assumes linear elastic phenomena and stated that brittle failure will occur if the absolute maximum principal stress exceeds a specific value. The Rankine criterion does not consider the other components of the stress tensor. Tresca stated that

ductile failure occurs if the maximum shear stress exceeds a specific value. The Rankine and Tresca rupture surface are identical for same sign principal stresses as shown in Figure . The von-mises is known as distortion energy criterion that develops a rupture surface similar to Tresca. Tresca is approximately 15% conservative than von-mises but less accurate in ductile failure prediction. A major limitation of the classic approaches is at equi-biaxial tension, $\sigma_x / \sigma_y = 1$ the rupture stress is non-conservative and identical to the uniaxial case as shown in Figure 7.1.

Later, many complex representative stress functions offering flexibility and capable of more accurate prediction are proposed by exploiting the assumptions of the classic models [**102**]. In 1958 Sodbyrev proposed a representative stress function that combines the effect of the maximum principal stress, σ_1 and von-mises stress, σ_{vm} as follows

$$\sigma_{rep} = \alpha\sigma_1 + (1-\alpha)\sigma_{vm}, \quad 0 \le \alpha \le 1 \tag{106}$$

where α is a material parameter constrained as $0 \le \alpha \le 1$ controlling the bias between σ_1, and σ_{vm} [103]. A function that combines the effect of hydrostatic stress, σ_m and von-Mises stress is available as

$$\sigma_{rep} = 3\beta\sigma_m + (1-\beta)\sigma_{vm}, \quad 0 \le \beta < 1 \tag{107}$$

where β is a material parameter controlling the stress bias [99]. In 1972, Hayhurst proposed a function [Eq. (108)] that is adopted by RCC-MR where [Eq. (106) and (107)] are special cases [96].

$$\sigma_{rep} = \alpha\sigma_1 + 3\beta\sigma_m + (1-\alpha-\beta)\sigma_{vm} \tag{108}$$

The material parameter α and β are constrained as $0 \le \alpha + \beta \le 1$. The Hayhurst representative stress [Eq. (108)] is reduced to [Eq. (107) and (113)] for $\alpha = 0$ and $\beta = 0$ respectively. It can be observed that the material parameter constraints $0 \le \alpha \le 1$, $0 \le \beta < 1$, and $0 \le \alpha + \beta \le 1$ of [Eq.

(106)-(108)] ensure that the sum of the stress coefficients is always unity. Some other widely used representative stress form are

$$\sigma_{rep} = \left(\frac{\sigma_1}{\sigma_{VM}} \right)^{\gamma/\nu} \sigma_{VM}, \quad 0 \le \gamma \le \nu \tag{109}$$

$$\sigma_{rep} = \left(\frac{3\sigma_m}{\sigma_{VM}} \right)^{\gamma/\nu} \sigma_{VM}, \quad 0 \le \gamma < \nu \tag{110}$$

where γ, and ν are the material parameter controlling the multiaxial bias on the von-mises stress [104-106]. A similar representative stress equation can be formulated combining [Eq. (109) and (110)] as follows

$$\sigma_{rep} = \left(\frac{\sigma_1}{\sigma_{VM}} \right)^{\gamma/\nu} \left(\frac{3\sigma_m}{\sigma_{VM}} \right)^{\mu/\nu} \sigma_{VM}, \quad 0 \le \gamma + \mu < \nu \tag{111}$$

The [Eq. (111)] is reduced to [Eq. (109) and (110)] for $\mu = 0$ and $\gamma = 0$ respectively. It should be noted that the constrains $0 \le \gamma \le \nu$, and $0 \le \gamma + \mu < \nu$ of [Eq. (109)-(111)] ensure that the order of the representative stress is always unity. For example, [Eq. (111)] can be written as follows

$$\sigma_{rep} = (\sigma_1)^{\gamma/\nu} (3\sigma_m)^{\mu/\nu} \sigma_{VM}{}^{1-\gamma/\nu-\mu/\nu} \tag{112}$$

where the sum of the power terms is always unity thus the order of both side of the [Eq. (112)] is balanced. In 1985, Huddleston proposed a more complex representative stress function that is adopted by ASME III

$$\sigma_{rep} = \frac{3}{2} S_1 \left(\frac{2\sigma_{VM}}{3S_1} \right)^a \exp\left[b \cdot \left(\frac{J_1}{S_s} - 1 \right) \right] \tag{113}$$

where J_1 is the first deviatoric stress $(J_1 = \sigma_1 + \sigma_2 + \sigma_3)$, S_1 is the first invariant of the stress tensor $(S_1 = \sigma_1 - J_1/3)$, and S_s is defined as $S_s = \sqrt{\sigma_1^{\,2} + \sigma_2^{\,2} + \sigma_3^{\,2}}$, and *a* and *b* are the adjusting coefficient [107, and 108].

7.2.2 Multiaxial Ductility

The classic multiaxial ductility function is the maximum principal strain yield criterion proposed by St. Venant assuming linear elastic phenomena and stated that rupture will occur if the absolute principal strain exceeds a specific value. St. Venant theory is the simplest as material parameter calibration is not required. Later several multiaxial ductility models are proposed that are flexible and more accurate [98-100]. In 1969, Rice and Treacy proposed a multiaxial ductility equation for spherical void growth during plastic deformation using a Sin-hyperbolic function

$$\varepsilon_{f_{VM}} / \varepsilon_{f_u} = 0.521 / \sinh(3\sigma_m / 2\sigma_{VM}) \tag{114}$$

where, $\varepsilon_{f_{vm}}$ and ε_{f_u} are the von-Mises rupture strain of notched bar and uniaxial bar respectively [109]. For cylindrical void growth during plastic deformation, the ductility equation takes the following exponential form

$$\varepsilon_{f_{VM}} / \varepsilon_{f_u} = \exp(0.5 - 3\sigma_m / 2\sigma_{VM}) \tag{115}$$

In 1975, Manjoine introduced, a similar relationship multiaxial ductility equation of exponent form [Eq. (116)] and revised it for steel as a ratio of von-mises and hydrostatic stress [Eq. (117)] [110, and 111]

$$\varepsilon_{f_{vm}} / \varepsilon_{f_u} = 2^{(1-3\sigma_m/\sigma_{VM})} \tag{116}$$

$$\varepsilon_{f_{vm}} / \varepsilon_{f_u} = \frac{\sigma_{vm}}{3\sigma_m} \tag{117}$$

Later in 1980, Cock and Ashby has proposed the following relationship assuming Norton power-law $\dot{\varepsilon}_{\min} = A\sigma^n$ creep deformation and grain boundary void growth

$$\frac{\varepsilon_{f_{VM}}}{\varepsilon_{f_u}} = \sinh\left[\frac{2(n-0.5)}{3(n+05)}\right] / \sinh\left[\frac{2(n-0.5)}{(n+05)}\left(\frac{\sigma_m}{\sigma_{VM}}\right)\right] \tag{118}$$

where n is the Norton power law constants [112]. In 1994, Spindler has proposed a ductile exhaustion method assuming that ductility is a function of creep strain rate which is adopted by British R5 procedure

$$\varepsilon_{f_n} / \varepsilon_{f_u} = \exp\left[\mathrm{p}\left(1 - \frac{\sigma_1}{\sigma_{VM}} \right) + q\left(0.5 - \frac{3\sigma_m}{2\sigma_{VM}} \right) \right] \tag{119}$$

where p and q are material parameters [100, 113]. It is suggested that $p = 2.38$ and $q = 1.04$ when rupture strain is a function of creep strain. And $p = 0.15$ and $q = 1.25$ when rupture strain is independent of creep strain rate. It should be noted that when $p = 0.0$ and $q = 1.0$, the [Eq. (119)] becomes identical to cylindrical void growth [Eq. (115)]. When $p = 0.0$ and $q = 2\ln(2)$ the [Eq. (119)] becomes identical to Manjoine [Eq. (116)]. A mixed mechanism model is proposed by Hales [114]. According to Hales, for diffusion controlled cavity growth and for constrained cavity growth [Eq. (120)] and [Eq. (121)] should be used respectively

$$\varepsilon_{f_{VM}} / \varepsilon_{f_u} = \left(\frac{\sigma_{VM}}{\sigma_1} \right)^{m+1} \tag{120}$$

$$\varepsilon_{f_{VM}} / \varepsilon_{f_u} = \frac{2\sigma_1}{3S_1} \left(\frac{\sigma_{VM}}{\sigma_1} \right)^{m+1} \tag{121}$$

7.2.3 Skeletal Point Stress

Another common practice is to use a skeletal point stress to determine the multiaxial stress criterion. It is assumed that upon loading a skeletal point exists inside the material where the stress remain unchanged in magnitude and position with time [99, 115-117]. The skeletal stress is independent of the creep properties of materials. A process to determine the skeletal point stress components, $\sigma_{vm}^*, \sigma_1^*, \sigma_m^*$ can be found in the literature [99]. Application of skeletal point stress for

multiaxiality at the tertiary creep stage is described by Othman [117]. Hyde and colleagues attempt to use the skeletal stress to determine the bias between von mises stress and maximum principal stress for multiaxial representative stress equation [118]. Comparing the representative stress, σ_{rep} with the skeletal stress components, $\sigma_{vm}^{*}, \sigma_{1}^{*}, \sigma_{m}^{*}$ the representative stress equation is determined. If the representative stress, σ_{rep} lies in between σ_{vm}^{*}, and σ_{1}^{*} then the representative function is a bias between von mises stress, and maximum principal stress (σ_1, and σ_m respectively). Similarly, if the representative stress, σ_{rep} lies in between σ_{1}^{*} and σ_{m}^{*} then the representative stress function is a bias between maximum principal stress, and hydrostatic stress (σ_1, and σ_m respectively) [99, 119]. A similar, skeletal point strain approach is available in literature [99]. However, considerable finite element analysis is required to determine the skeletal stress components accurately [99]. Goodall and colleagues reported that the direct use of skeletal point stress components, $\sigma_{vm}^{*}, \sigma_{1}^{*}, \sigma_{m}^{*}$ to correlate multiaxial creep data with uniaxial leads to faulty prediction and a representative stress equation should be used [98]. Spindler, proved that in practice no skeletal stress exists inside the material that does not changes with time [119]. Spindler concluded that using a skeletal stress will provide an underestimated of creep damage and it cannot be used to study multiaxiality. Hayhurst and colleagues made efforts in describing the limitations and breakdown situations of skeletal stress technique for multiaxiality [116]. In this study the skeletal technique is not considered.

7.2.4 Incompressibility

It is assumed that the creep is an incompressible process such that deformation and damage should not be accumulate under compression. Constrains can be applied on representative stress function during numerical analysis to avoid tensile deformation under compressive load. The von-mises stress equation is defined as a function of principal stresses as follows

$$\sigma_{vm} = \frac{1}{\sqrt{2}}\sqrt{(\sigma_1 - \sigma_2)^2 + (\sigma_2 - \sigma_3)^2 + (\sigma_3 - \sigma_1)^2} \tag{122}$$

where $\sigma_1, \sigma_2,$ and σ_3 are the first, second and third principal stress respectively. It is evident from [Eq. (122)] that the von-mises stress is always positive regardless of the positive/negative

Table 30 – Hayhurst representative stress function under compression conditions

Load σ_x, σ_y, σ_z	Principal stress σ_1, σ_2, σ_3	Developed σ_{VM} [Eq. (122)]	Required constrain for $\sigma_{rep} \le 0$					
			[Eq. (106)]	[Eq. (108)]	[Eq. (106)]	[Eq. (107)]	[Eq. (109)]	[Eq. (110)]
$-\sigma$, 0.0, 0.0	0.0, 0.0, $-\sigma$	σ	$\alpha \ge 1$	$2\beta \le 1$	$\alpha + 2\beta \ge 1$	$\sigma_{rep} = 0$	Imaginary number	Imaginary number
$-\sigma$, $-\sigma$, 0.0	0.0, $-\sigma$, $-\sigma$	σ	$\alpha \ge 1$	$3\beta \le 1$	$\alpha + 3\beta \ge 1$	$\sigma_{rep} = 0$	Imaginary number	Imaginary number
$-\sigma$, $-\sigma$, $-\sigma$	$-\sigma$, $-\sigma$, $-\sigma$	0	$\alpha \ge 0$	$3\beta \le 1$	$\alpha + 3\beta \ge 1$	Imaginary number	Imaginary number	Imaginary number

sign of the principal stresses. Thus a positive representative stress may develop under compression condition leading to unrealistic tensile deformation during numerical simulation. Proper constrain is required for the material parameters used in [Eq. (108)-(111)] such that the representative stress in non-positive, $\sigma_{rep} \le 0$ under compression. Towards developing such constrain for Hayhurst function [Eq. (108)], a three dimensional element inside the material under uniaxial, equi-biaxial, and equi-triaxial compression condition is considered for analysis.

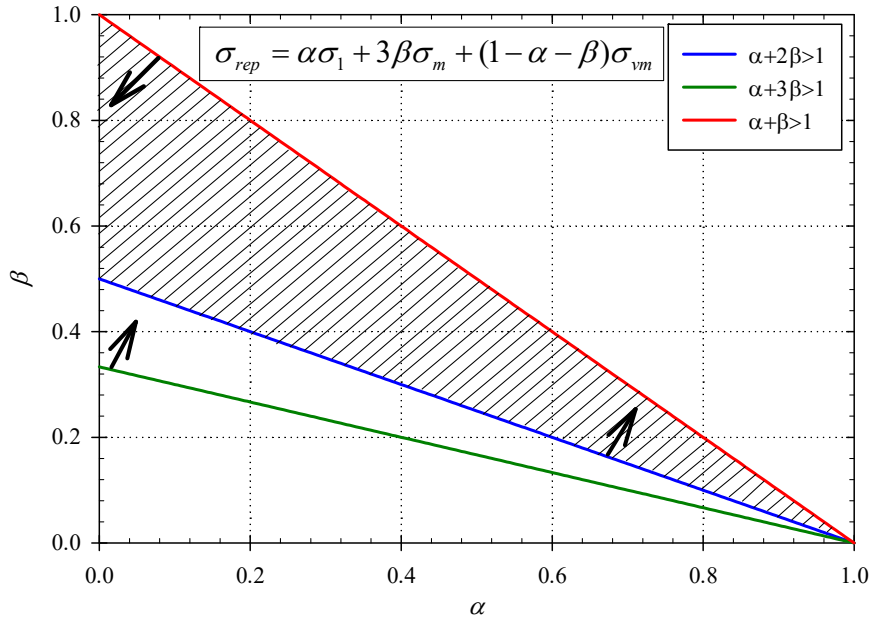

Figure 7.2 – Material parameter combination region that enforce incompressible creep for Hayhurst function

Under uniaxial compression $(\sigma_x = \sigma_z = 0, \sigma_y = -\sigma)$, the developed principal and von-mises stresses are $(\sigma_1 = \sigma_2 = 0, \sigma_3 = -\sigma, \sigma_{vm} = \sigma)$. Under this condition the representative stress should not be positive, $\sigma_{rep} \le 0$. Applying this conditions to [Eq. (108)], required constrain for Hayhurst representative stress can be obtained as follows

$$0 \ge 3\beta \cdot (-\sigma / 3) + (1-\alpha-\beta) \cdot \sigma \tag{123}$$

$$\alpha + 2\beta \ge 1 \tag{124}$$

This suggests that for material parameter combinations satisfying constraint $\alpha + 2\beta \ge 1$ will not exhibit tensile representative stress under compression. Equi-biaxial and equi-triaxial compressive stress condition is applied and the corresponding constrains are listed in Table 30. These constrained are plotted to visualize the critical constrains and to identify valid (α, β) combination field. In the Figure 7.2, the red line enclose the upper limit of (α, β) combination with

α and β axis's as defined in [Eq. (108)], $0 \le \alpha + \beta \le 1$. The green and blue lines represents the $\alpha + 3\beta \ge 1$ and $\alpha + 2\beta \ge 1$ constrains listed in Table 30. It is evident from Figure 7.2 that the $\alpha + 2\beta \ge 1$ constrain is critical and enclose the (α, β) combination that satisfies all constrains. Thus during numerical analysis, tensile creep deformation under compressive load can be avoided by imposing $\alpha + 2\beta \ge 1$ constrain. Similar analysis is performed.

7.3 REPRESENTATIVE RUPTURE SURFACE

The rupture surfaces of the Sodbyrev [Eq. (106)], [Eq. (107)], and Hayhurst [Eq. (108)] function at different material parameter conditions are depicted in Figure 7.3. Five material parameters are chosen for each functions to facilitate critical, and comparative analysis between the representative functions. It is observed that the Sodbyrev rupture surface [Eq. (106)] become identical to Rankine rupture surface for uniaxial and biaxial tension at $\alpha = 1.0$ but does not coincide when compressive stress is larger than tensile stress as depicted in Figure 7.3a. This is because Rankine consider the absolute maximum principal stress as rupture criteria while Sodbyrev consider tensile maximum principal stress as rupture criteria. For example, at $(-\sigma, -\sigma, 0)$ equi-biaxial compression, Rankine assumes σ as rupture stress while Sodbyrev assumes zero as rupture stress. Sodbyrev function become identical to von-mises rupture surface at $\alpha = 0.0$ as shown in Figure 7.3a. Thus the Sodbyrev rupture surfaces for $0 \le \alpha \le 1$ evolves from similar Rankine to von-mises rupture surface for different α values as shown in Figure 7.3a. It should be noted that at equi-biaxial tension the rupture stress of [Eq. (106)] is equal to uniaxial case that is unrealistic.

The representative stress function [Eq. (107)] develops a hydrostatic rupture surface at $\beta = 1.0$ and becomes identical to von-mises rupture surface at $\beta = 0.0$. This suggest that the rupture surface of [Eq. (107)] for $0 \le \beta \le 1$ evolves from hydrostatic to von-mises rupture surface for

different β values as shown in Figure b. Comparing the rupture surface of [Eq. (106) and (107)] it is observed that the [Eq. (106)] cannot converge to pure hydrostatic rupture surface and [Eq. (107)] cannot converge to pure principal rupture surface.

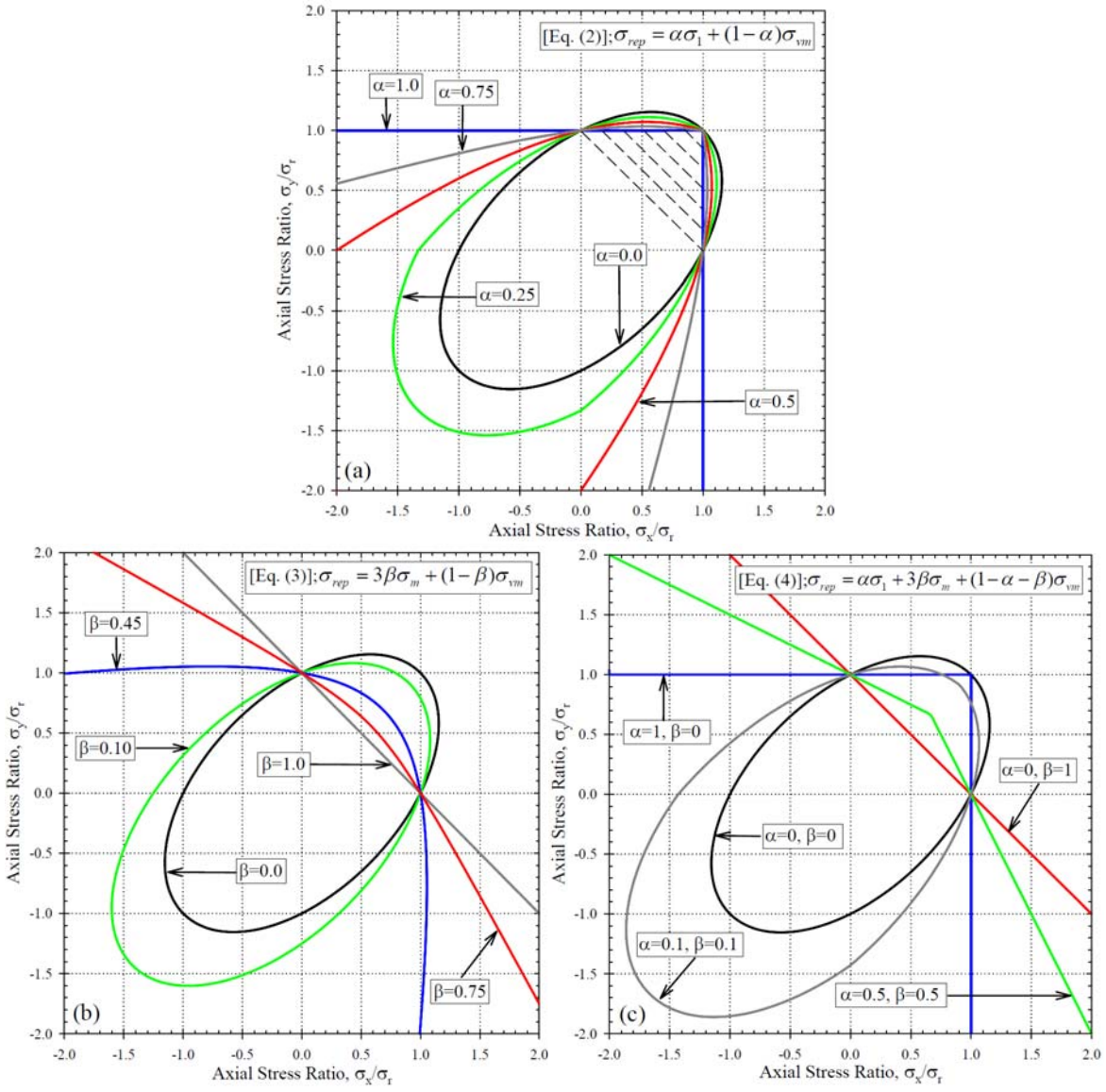

Figure 7.3 – Rupture surfaces of (a) [Eq. (106)], (b) [Eq. (107)], and (c) [Eq. (108)] at five different material parameter conditions

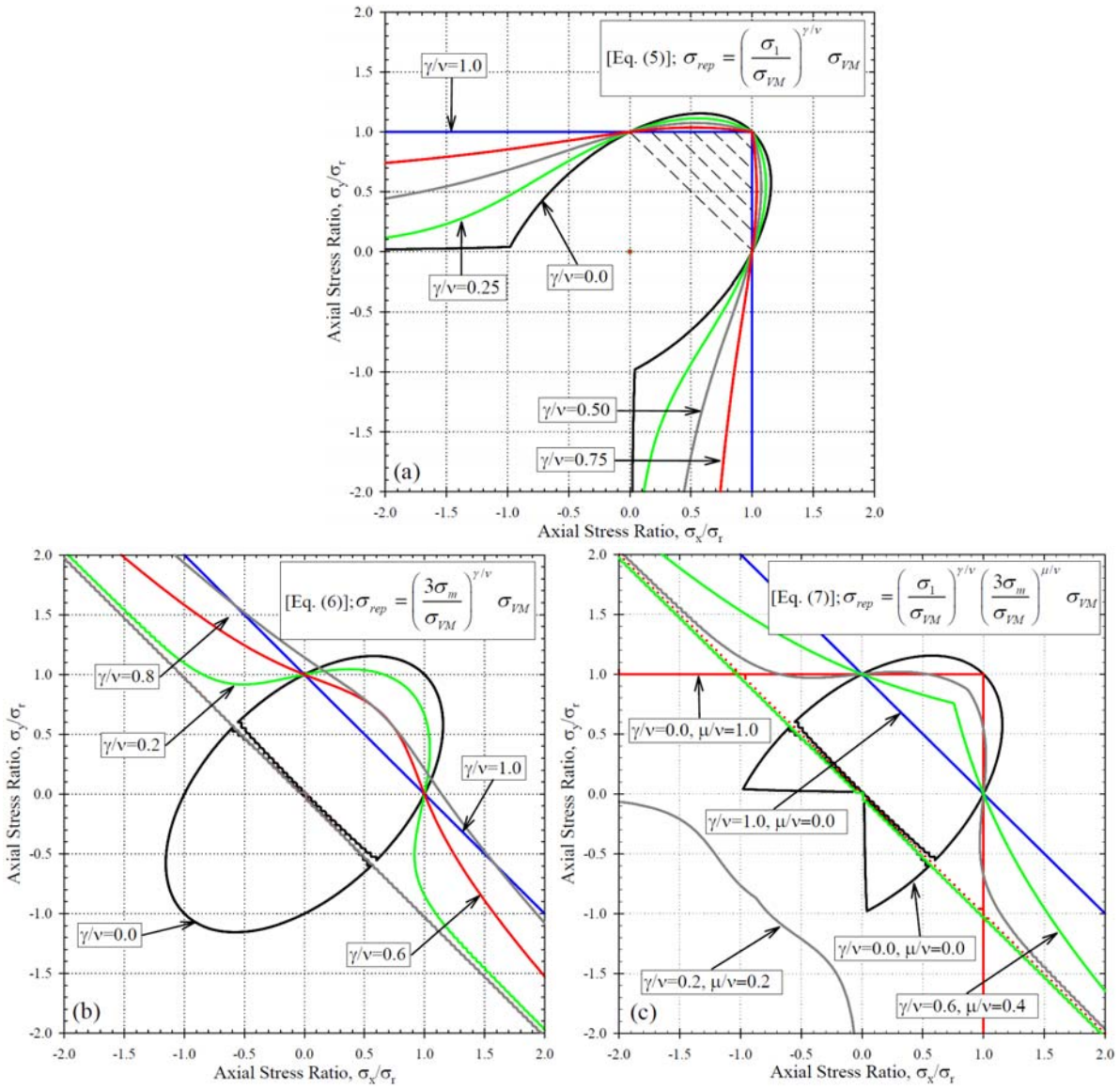

Figure 7.4 – Rupture surfaces of (a) [Eq. (109)], (b) [Eq. (110)], and (c) [Eq. (111)] at five different material parameter conditions

The [Eq. (106)] cannot predict a rupture criteria in the region marked by the short-dash lines in Figure 7.3a. Thus the [Eq. (107)] is more flexible than the [Eq. (106)]. It should be noted that at equi-biaxial tension the rupture stress of [Eq. (106)] is always equal to uniaxial case while the rupture stress of [Eq. (107)] is lower than the uniaxial case thus provide more realistic prediction over [Eq. (106)]. The effect of hydrostatic stress facilitates this improved behavior. The Hayhurst

function [Eq. (108)] incorporates the combined effect of principal, hydrostatic, and the von-mises stresses that offer more flexibility than [Eq. (106) and (107)] and overcome their individual limitations as shown in Figure 7.3c. Thus the Hayhurst is the most prominent function of the three functions.

The rupture surface of the [Eq. (109), (110), and (111)] at five different material parameter conditions are depicted in Figure 7.4. The rupture surface of [Eq. (109)] at $\gamma/\nu = 1.0$ become identical to the rupture surface of [Eq. (106)] at $\alpha = 1.0$. However, for the other value $0 \le \gamma/\nu < 1.0$ the rupture surfaces does not coincide. For example, the rupture surface of [Eq. (109)] at $\gamma/\nu = 0.0$ become identical to von-mises except biaxial compression region as observed in Figure a. This is because for biaxial compression, the maximum tensile principal stress become zero leading to zero representative stress for [Eq. (109)]. This is a significant difference between [Eq. (106) and (109)] rupture surfaces. Both equation [Eq. (106) and (109)] uses the combined effect of maximum principal stress and the von-mises stress but [Eq. (109)] produce zero representative stress for biaxial compression suppressing creep damage under biaxial compression as shown in Figure 7.4a for different values of γ/ν. This is an advantage of [Eq. (109)] over [Eq. (106)]; however, the [Eq. (109)] becomes infinite at (0, 0) stress condition as observed in Figure a (dot mark at the origin point) that may lead to numerical instability during simulation. The [Eq. (109)] exhibit similar limitation of [Eq. (106)] at equi-biaxial tension. The [Eq. (109)] rupture surface cannot predict a rupture criteria in the region marked by the short-dash lines in Figure 7.4a.

The rupture surface of [Eq. (110)] at $\gamma/\nu = 0.0$ is identical to von-mises except for same magnitude but opposite sign stress conditions as depicted in Figure 7.4b. For example at a stress condition $(\sigma, -\sigma)$ the hydrostatic stress become zero leading to discontinuous von-mises rupture surface. For compressive hydrostatic stress at $0 < \gamma/\nu < 1$ the [Eq. (110)] develops imaginary

number that may lead to numerical instability during simulation as shown in Figure 7.4b marked by diagonal lines. A solution to avoid imaginary values may be to use absolute hydrostatic stress to avoid negative value. Such approach will lead to mirror rupture surface with respect to the diagonal. The rupture surface at $\gamma/\nu = 1.0$ become identical to hydrostatic rupture surface of [Eq. (107)] at $\beta = 1.0$. The [Eq. (110)] consider the effect of hydrostatic stress thus the rupture at equi-biaxial tension is lower than the uniaxial case providing advantages over [Eq. (109)].

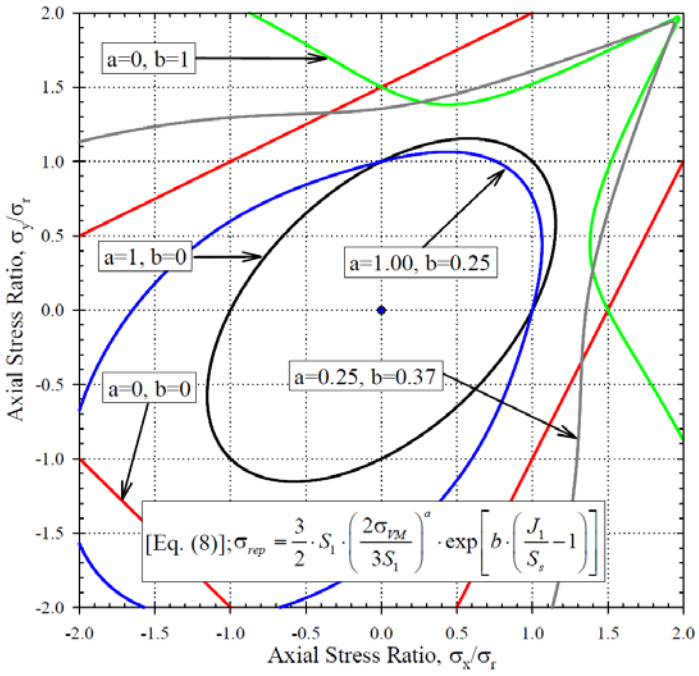

Figure 7.5 – Rupture surfaces of Huddleston function at five different material parameter conditions

The rupture surface of [Eq. (111)] exhibit a combination of [Eq. (107) and (109)] that offer flexibility but become more sensitive to stress state and martial parameter as depicted in Figure 7.4c. Thus [Eq. (111)] is superior to [Eq. (109)] and [Eq. (110)] only for biaxial tension. The Huddleston function [Eq. (113)] rupture surface at five different material parameter combination is depicted in Figure 7.5. The function become identical to von-mises at $a = 1, b = 0$ but cannot

converge to principal and hydrostatic rupture surface as these stresses are not used explicitly within the funciton. At $a = 0, b = 0$ a unique first deviatoric rupture stress rupture surface is observed. Similarly, the uses of first invariant of stress of tensor, S_1 and root sum square of the principal stresses, S_s provide unique flexibility to Huddleston over other functions.

Comparing the rupture surfaces of [Eq. (106)-(111)] it is evident that complete description of multiaxial stress analysis can be performed only with the functions that incorporates the combined effect of the principal, hydrostatic and von-mises stresses explicitly and/or implicitly. The Hayhurst and the Huddleston functions are the most potential for multiaxial rupture analysis. The Huddleston function offer more flexibility over the Hayhurst function but become unstable at (0,0,0) stress condition. The Hayhurst function does not use a stress ratio thus is stable for complete multiaxial stress states.

7.4 GUIDELINE TO REPRESENTATIVE STRESS FUNCTION SELECTION

It is observed that post-classic functions are based on von-mises stress criterion that is used explicitly within the function such that von-mises rupture surface is a special case. Exploiting the above discussions a guideline is proposed

Stress function: The multiaxial rupture under creep depends on the component geometry and material properties that may lead to strengthening or weakening behavior. Hayhurst and Huddleston both function can be used to predict complete description of multiaxial stress states. The Hayhurst function is simpler compared to Huddleston function thus the Hayhurst function may be chosen first for regression analysis. If the Hayhurst function exhibits a poor fit then the complex Huddlelstone function may be used. Another option is to develop a new mathematical function. Some example complex function that is applied recently is available.

Incompressibility: Constraints can be applied to the representative stress function to avoid creep deformation under compression as discussed in incompressibility section.

Numerical stability: Depending on the stress state a function can become infinite or imaginary leading to numerical instability. Special care should be taken before application of new developed functions. Hayhurst function is stable for complete multiaxial stress states while the Huddleston become infinite at zero triaxial stress.

Experiment condition: Hayhurst states that to determine the material parameter uniaxial, pure shear, and equi-biaxial tension test must be performed [96]. Later Spindler stated that equi-biaxial tension tests data can be used to distinguish the bias between hydrostatic and principal stress [100]. Regression analysis can be performed easily using Equi-biaxial test data such that data fitting can be visualized in rupture surface plot as discussed in representative rupture surface section.

Material parameter: Huddleston and Spindler states that the material parameter can be calibrated by regression analysis [100, and 108]. Dominant damage mechanism during creep may be used to determine bias between the individual stresses in the representative function. It is suggested in the code of practice of European Structural Integrity Society (ESIS) that the von-mises stress dominate the deformation, while the hydrostatic and principal stress dominate the void growth and intergranular damage respectively [99]. The identification of damage mechanism requires additional failure analysis that may not be always possible. However, the knowledge of fracture mechanism may be of little use as it does not give the calibrated value of material coefficients; regression analysis is required.

7.5 SUMMARY

In this chapter, the classic and most widely used multiaxial representative functions are discussed. Representative stress functions are exploited to understand the advantages and limitations of the

function. Rupture surface at five different material parameter conditions are analyzed. It is observed that

- the classic functions and the functions that does not incorporate the effect of hydrostatic stress provide an unrealistic prediction under equi-biaxial tension;
- the functions incorporating the combined effect of the principal, hydrostatic, and von-mises stresses are the only functions that can predict complete description of multiaxial stress conditions;
- material parameter constraints can be developed to avoid creep deformation under compression.

Chapter 8: Conclusion and Future Work

8.1 CONCLUSION

An adaptive creep modeling approach using metamodeling is developed. The metamodeling approach is demonstrated for classic time-temperature parameter model and creep deformation models.

8.1.1 Metamodeling for classic time-temperature parametric model:

Metamodeling is applied to twelve time-temperature parameter (TTP) model to develop a metamodel that simplifies the constant determination process. A guideline for easy application of the metamodel is provided. A systematic MATLAB code is developed that facilities easy application of the guidelines. (1) calculate the parameter and determine the most suitable stress-parameter function; (2) calibrate material constants; (3) report the normalized mean square error (NMSE) of each model; and (4) recommend the most physically realistic TTP model for given experimental data. Model calibration to large data set became easier.

8.1.2 Metamodeling for creep deformation model:

Metamodeling is employed to derive functional relationships between the Omega, Theta, and Sinh creep deformation, damage, and rupture models. The model transformation identities Theta-Omega, Omega-Sinh, and Sinh-Theta can be used to convert one model's constants to the constant of another. These identities when mathematically manipulated reveal six viable combinational models. It is determined that the combinational models produce acceptable predictions of creep deformation and rupture data, can be more conservative than the classic models, and the normalized mean square error can be on par with the classic models.

8.1.3 Disparate data problem and the development of design maps:

It is proved that integrating disparate creep data into the calibration of creep model can lead to more reliable extrapolation. A detailed procedure for calibrating CDM models using disparate data. The reliability of extrapolation is demonstrated using post-audit validation of the calibrated model. Extrapolation of creep deformation at four rupture points developing a reliability band from 0 to 100% agree with experimental data up to 10^5 hrs. A variety of creep design maps are illustrated and demonstrate that the interpolation and extrapolation ability of CDM models can be compared graphically using the creep design maps. A MATLAB algorithm that perform instant interpolation and extrapolation to generate design maps for minimum-creep-strain-rate, stress-rupture, creep deformation, and damage.

8.1.4 Representative rupture surface:

The classic and most widely used multiaxial representative functions are discussed. Representative stress functions are exploited to understand the advantages and limitations of the function. Rupture surface at five different material parameter conditions are analyzed. It is observed that the functions incorporating the combined effect of the principal, hydrostatic, and von-mises stresses are the only functions that can predict complete description of multiaxial stress conditions.

8.2 FUTURE WORK

Below are the listed topics of future work related to the improvement of metamodeling approach:

Integration of probabilistic methods in the development of Design Maps:

Future work should focus on the integration of probabilistic methods in the development of the design maps. Maps that take into consideration the prior service history. The current design

maps are applicable for brand new parts. The maps are not appropriate for an existing part in power plant where the operating condition during service change (i.e. when a plant is switched between base-load, load-following, and/or peak-load operations). In addition, the approach can be expanded for non-isothermal and -isostress conditions (i.e creep-fatigue").

Multiaxial model for metamodel

Another potential scope is to expand the metamodeling for multiaxial stress condition. Combining the findings in metamodeling sections 4.0 and 5.0 with the Multiaxial representative function section 7.0; a multiaxial model can be developed that can facilitate analysis of complex geometry components.

3D Finite Element Simulation

3D finite element implementation and simulation of the combinational models to analyze convergence, notch-sensitivity, and damage localization of the new models.

References

[1] Homji, C. B. M. and Gabriles, G. (1998). Gas Turbine Blade Failures-Causes, Avoidance, Aad Troubleshooting. 27th Turbomachinery Symposium. pp. 129.

[2] Dundas, R. E. (1982). The Use of Performance Monitoring to Prevent Compressor and Turbine Failures. ASME Gas Turbine Congress, Paper Number: 882-GT -66.

[3] Bloch, H. P. (1998). Improving machinery reliability (Vol. 1). Gulf Professional Publishing.

[4] Ren W., and Luttrell C., (2006). Gen IV Materials Handbook Beta Release for Structural and Functional Evaluation. US Department of Energy, Report No. ORNL/GEN4/LTR-06–027.

[5] Materials Creep Database of NIMS – National Institutes for Materials Science, Japan. http://smds.nims.go.jp/creep/index_en.html

[6] Berkeley Research Company, 600 Addison Street, Berkeley, California, 94710.

[7] Naeem, M. T., Rezamahdi, N., and Jazayeri, S. (2009). Failure analysis of gas turbine blades. Engineering Technology Opens the Door to a World of Opportunity, 29.

[8] Ejaz, N., Qureshi, I. N., and Rizvi, S. A. (2011). Creep failure of low pressure turbine blade of an aircraft engine. Engineering Failure Analysis, 18(6), 1407-1414.

[9] Salam, I., Tauqir, A., and Khan, A. Q. (2002). Creep-fatigue failure of an aero engine turbine blades. Engineering Failure Analysis, 9(3), 335-347.

[10] F.H. Norton, The Creep of Steels at I-[ig/z Temperatz¢res, McGraw-HilI, New York, i929.

[11] C. M. Stewart, and A. P. Gordon, (2011). Strain and Damage-Based Analytical Methods to Determine the Kachanov-Rabotnov Tertiary Creep Damage Constants, International Journal of Damage Mechanics, 21(8) 1186-1201. doi: 10.1177/1056789511430519

[12] Prager, M., (1995), "Development of the MPC omega method for life assessment in the creep range," Transactions-American Society of Mechanical Engineers Journal of Pressure Vessel Technology, 117, pp. 95-95.

[13] Manu, C. C., Birk, A. M., and Kim, I. Y., (2009), "Uniaxial high-temperature creep property predictions made by CDM and MPC omega techniques for ASME SA 455 steel," Engineering Failure Analysis, 16(4), pp. 1303-1313.

[14] Evans, R. W., Parker, J. D., & Wilshire, B., (1992), "The θ model concept—A model-based approach to design and life extension of engineering plant," International Journal of Pressure vessels and piping, 50(1), pp. 147-160.

[15] Hollomon, JH, and Jaffe, LD, (1945), "Time-Temperature Relations in Tempering Steel," Transaction of AIME, Iron and Steel Division, 162, pp. 223-249.

[16] Conway, JB., (1969), Stress Rupture Parameters: Origin, Calculation, and Use, Gordon and Breach.

[17] Manson, S. S., and Haferd, A. M., (1953), "A Linear Time Temperature Relation for Extrapolation of Creep and Stress Rupture Data," National Advisory Committee for Aeronautics.

[18] A. Cauvin, R. B. Testa, Damage mechanics: basic variables in continuum theories, International Journal of Solids and Structures, 36 (1999) 747-761. http://dx.doi.org/10.1016/S0020-7683(98)00044-4

[19] J. J. Marigo, (1985). Modeling of Brittle and Fatigue Damage for Elastic Material by Growth of Micro-voids, Engineering Fracture Mechanics, 21, 861-874. https://doi.org/10.1016/0013-7944(85)90093-1

[20] U. Lindborg, (1968), Creep cracks and the concept of damage, Journal of the Mechanics and Physics of Solids, 16.5, pp 323-328. https://doi.org/10.1016/0022-5096(68)90019-7

[21] E. A. Ibijola, (2002) On some fundamental concepts of continuum damage mechanics, Computer methods in applied mechanics and engineering, 191.13 pp. 1505-1520. http://dx.doi.org/10.1016/S0045-7825(99)90187-1

[22] J. Lemaitre, (1985) A continuous damage mechanics model for ductile fracture, Journal of Engineering Materials and Technology, 107.1 pp. 83-89. doi:10.1115/1.3225775

[23] J. L. Chaboche, (1978) Description thermodynamique et phenomenologique de la visco-plasticite cyclique avec endommagement, Theses Dissertation, University of Paris 6.

[24] J. P. Cordebois, F. Sideroff, (1982) Endommagement anisotrope delasticite et plasticite, Journal Mech. Theor. Appl. Special issue.

[25] P. Raghavan, S. Ghosh, A continuum damage mechanics model for unidirectional composites undergoing interfacial debonding, Mechanics of materials, 37.9 (2005) 955-979. http://dx.doi.org/10.1016/j.mechmat.2004.10.003

[26] R. Hill, Elastic properties of reinforced solids: some theoretical principles, Journal of Mechanics, Physics and Solids. 11, (1963) 357-372. https://doi.org/10.1016/0022-5096(63)90036-X

[27] Z. Hashin, Analysis of composite materials, Journal of Applied Mechanics, 50 (1983) 481-505. doi:10.1115/1.3167081

[28] L. M. Kachanov, The Theory of Creep, National Lending Library for Science and Technology, Boston Spa, England, Chaps. IX, X, 1967.

[29] Y. N.Rabotnov, Creep Problems in Structural Members, Amsterdam, Weinheim, North Holland, WILEY-VCH Verlag GmbH and Co. KGaA, 1969.

[30] R. K. Penny, M. A. Weber, Robust Methods of Life Assessment during Creep, Int. Journal of Pressure Vessel and Piping, 50 (1992) 109-131. https://doi.org/10.1016/0308-0161(92)90033-C

[31] R. K. Penny, The use of damage concept in component life assessment, Int. Journal of Pressure Vessel and Piping, 66 (1996) 263-280. https://doi.org/10.1016/0308-0161(95)00101-8

[32] H. C. Furtado, I. L. May, L. H. Almeida, R. Peace, Extrapolation of shorter time creep rupture data using the damage mechanics approach of Penny, In ASME/JSME Pressure Vessels and Piping Conference, (2004) 11-17. doi:10.1115/PVP2004-2253

[33] I. Le May, H. C. Furtado, Creep damage assessment and remaining life evaluation, International Journal of Fracture, 97 (1999) 125-135. doi:10.1023/A:1018396017834

[34] W. Qi, and A. Bertram, Damage modeling of the single crystal superalloy SRR99 under monotonous creep, Computational materials science, 13(1) (1998) 132-141. http://doi.org/10.1016/S0927-0256(98)00053-6

[35] Liu, Yan, S. Murakami, Damage Localization of Conventional Creep Damage Models and Proposition of a New Model for Creep Damage Analysis, JSME International Journal Series A, 41.1 (1998) 57-65. http://doi.org/10.1299/jsmea.41.57

[36] C. J. Hyde, T.H. Hyde, W. Sun, A. A. Becker, Damage mechanics based predictions of creep crack growth in 316 stainless steel, Engineering Fracture Mechanics, 77 (2010) 2385-2402. http://doi.org/10.1016/j.engfracmech.2010.06.011

[37] J. F. Wen, S. T. Tu, X. L. Gao, J. N. Reddy, Simulations of creep crack growth in 316 stainless steel using a novel creep-damage model, Engineering Fracture Mechanics, 98 (2013) 169-184. http://doi.org/10.1016/j.engfracmech.2012.12.014

[38] M. S. Haque, C. M. Stewart, Finite-Element Analysis of Waspaloy Using Sinh Creep-Damage Constitutive Model Under Triaxial Stress State, Journal of Pressure Vessel Technology, 138(3) (2016) 031408. doi: 10.1115/1.4032704

[39] M. S. Haque, C. M. Stewart, The Stress-Sensitivity, Mesh-Dependence, and Convergence of Continuum Damage Mechanics Models for Creep, Journal of Pressure Vessel Technology, doi: 10.1115/1.4036142.

[40] M. S. Haque, C. M. Stewart, A Novel Sin-Hyperbolic Creep Damage Model to Overcome the Mesh Dependency of Classic Local Approach Kachanov-Rabotnov Model, In ASME 2015 International Mechanical Engineering Congress and Exposition, (2015) V009T12A023-V009T12A023. doi:10.1115/IMECE2015-50427

[41] C. M. Stewart, A. P. Gordon, A Hybrid Constitutive Model for Creep, Fatigue, And Creep-Fatigue Damage, Ph.D. Dissertation, University of Central Florida, Orlando, Fl, 2013.

[42] J. J. Skrzypek, A. Ganczarski, Modeling of material damage and failure of structures: Theory and applications, Berlin Heidelberg, Springer-Verlag, 1999.

[43] M. S. Haque, C. M. Stewart, Comparison of a new Sinh-hyperbolic creep damage constitutive model with the classic Kachanov-Rabotnov model using theoretical and numerical analysis, TMS, 144th Annual Meeting and Exhibition, Florida, USA, (2015) 15-19. doi: 10.1007/978-3-319-48127-2_114

[44] H. Basoalto, S. K. Sondhi, B. F. Dyson, M. Mclean, A generic microstructure-explicit model of creep in nickel-base superalloys," Superalloys, TMS, (2004), 897-906.

[45] S. Murakami, Y. Liu, M. Mizuno, Computational methods for creep fracture analysis by damage mechanics, Comput. Methods Applied Mechanics Engineering, 183 (2000), 15-33. http://doi.org/10.1016/S0045-7825(99)00209-1

[46] Y. Liu, S. Murakami, Y., Kanagawa, Mesh-dependence and stress singularity in finite element analysis of creep crack growth by continuum damage mechanics approach, European Journal Mech. A/Solids, 13 (1994), 395–417.

[47] Z. P. Bazant, G. Cabot Pijaudie, Nonlocal continuum damage, localization instability and convergence, J. Appl. Mech. Trans. ASME, 55 (1988), 287-294. doi:10.1115/1.3173674

[48] P. Ladeveze, A damage computational method for composite structures, Computers and Structures, 44.1 (1992) 79-87. https://doi.org/10.1016/0045-7949(92)90226-P

[49] P. G. McVetty, Creep of Metals at Elevated Temperatures – Hyperbolic-Sine Relation Between Stress and Creep Rate, Transactions of the ASME, 65(7) (1943) 761-767.

[50] AK Steel, 304/304L Stainless Steel Specification Sheet. West Chester, OH.

[51] Kim, S.J., Kong, Y.S., Roh, Y.J., Kim, W.G., 2008. Statistical properties of creep rupture data distribution for STS304 stainless steels. Mater. Sci. Eng. A 483-484, 529–532. doi:10.1016/j.msea.2006.12.153

[52] Boyer, H. E., 1988, Atlas of Creep and Stress-Rupture Curves, ASM International, pp. 11.30-11.51

[53] Simmons, F. W., and Van Echo, J. A., 1965, "Report on the Elevated Temperature Properties of Stainless Steels", DS 5-S1, American Society for Testing and Materials, Philadelphia, PA.

[54] Simmons, W. F., and Cross, H. C., 1952, "Report on the Elevated-Temperature Properties of Stainless Steels", STP 124, American Society for Testing and Materials, Philadelphia, PA.

[55] Heger, J. J., and Smith, G. V., "Elevated Temperature Properties as Influenced by Nitrogen Additions to Types 304 and 316 Austenitic Stainless Steels", STP 552, American Society for Testing and Materials, Philadelphia, PA.

[56] National Institute of Material Science, Creep Datasheet Database, http://smds.nims.go.jp/MSDS/en/sheet/Creep.html, Accessed August 1, 2016

[57] Hill, M. R., 1976, "Mechanical Properties Test Data for Structural Materials Quarterly Progress Report for Period Ending October 31, 1976", ORNL-5237, Oak Ridge National Laboratory, Oak Ridge, TN.

[58] Šeruga, D., and Nagode, M., 2011, "Unification of the most commonly used time–temperature creep parameters," Materials Science and Engineering: A, 528(6), pp. 2804-2811.

[59] Haque, M. S., and Stewart, C. M., 2016, "Exploiting Functional Relationships Between MPC Omega, Theta, and Sinh-Hyperbolic Continuum Damage Mechanics Model," In ASME Pressure Vessels and Piping Conference, Vancouver, British Columbia, pp. 1-11.

[60] Ramirez, C., Haque, M. S., & Stewart, C. M. (2017, July). Guidelines to the Assessment of Creep Rupture Reliability for 316SS Using the Larson-Miller Time-Temperature Parameter Model. In ASME 2017 Pressure Vessels and Piping Conference (pp. V06AT06A068-V06AT06A068). American Society of Mechanical Engineers.

[61] Haque, M. S., and Stewart, C. M., 2016, "Modeling the Creep Deformation, Damage, and Rupture of Hastelloy X Using MPC Omega, Theta, and Sin-Hyperbolic Models," In ASME Pressure Vessels and Piping Conference, Vancouver, British Columbia, pp. 1-10.

[62] F.R. Larson, J. Miller, 1952, Transaction of ASME, 74, pp. 765.

[63] S.S. Manson, and W.F. Brown, 1953, Proceedings of ASTM, 53, pp. 683–719.

[64] R.L. Orr, O.D. Sherby, and J.E. Dorn, 1954, Transaction of ASM, 46, pp. 113–118.

[65] Manson, S. S., Succop, G., and Brown Jr, W. F., 1959, "The Application of Time-Temperature Parameters to Accelerated Creep-Rupture Testing," Transaction of ASM, 51, pp. 911-934.

[66] Graham, K. F. A. Walles, 1955, “Relationships between long and short time creep and tensile properties of a commercial alloy,” Journal: Iron and Steel Institute, 179, pp. 105.

[67] Chitty and D. Duval, 1963, “The creep-Rupture Properties of Tubes for High-Temperature Steam Power Plant,” Joint International Conference on Creep, Book 3, Paper no. 2, pp. 1-4.

[68] Goldhoff, Robert M., and G. J. Hahn, 1968, "Correlation And Extrapolation Of Creep-Rupture Data Of Several Sheets of steel And Superalloys Using Time- Temperature Parameters".

69] Goldhoff, R. M., 1974, “Towards the standardization of time-temperature parameter usage in elevated temperature data analysis,” Journal of Testing and Evaluation, 2(5), pp. 387-424.

[70] Wilson, D. J., Marrone, R. E., & Freeman, J. W. (1968). Larson-Miller and Manson-Haferd parameter extrapolation of rupture data for type 304 (18Cr-8Ni), grade 22 (2-1/4Cr-1Mo) and grade 11 (1-1/4Cr-1/2Mo-3/4Si) steels.

[71] Manson, S. S., and Ensign, C. R., 1979, “A quarter-century of progress in the development of correlation and extrapolation methods for creep rupture data,” Journal of Engineering Materials and Technology, 101(4), pp. 317-325.

[72] Eno, D. R., Young, G. A., and Sham, T. L., 2008, “A unified view of engineering creep parameters,” In ASME Pressure Vessels and Piping Conference, Chicago, Illinois, pp. 777-792.

73] Holdsworth, S. R., and Davies, R. B., 1999, “A recent advance in the assessment of creep rupture data,” Nuclear Engineering and design, 190(3), pp. 287-296.

[74] Goldhoff, R. M. (1974). Towards the standardization of time-temperature parameter usage in elevated temperature data analysis. Journal of Testing and Evaluation, 2(5), 387-424.

[75] Wilson, D. J., Marrone, R. E., & Freeman, J. W. (1968). Larson-Miller and Manson-Haferd parameter extrapolation of rupture data for type 304 (18Cr-8Ni), grade 22 (2-1/4Cr-1Mo) and grade 11 (1-1/4Cr-1/2Mo-3/4Si) steels.

[76] Davies, R. B., Hales, R., Harman, J. C., and Holdsworth, S. R., 1999, “Statistical modeling of creep rupture data,” Journal of engineering materials and technology, 121(3), pp. 264-271.

[77] Holmström, S., & Auerkari, P. (2008). Effect of short-term data on predicted creep rupture life–pivoting effect and optimized censoring. Materials at High Temperatures, 25(3), 103-109.

[78] Holdsworth, S. R., and Davies, R. B., 1999, “A recent advance in the assessment of creep rupture data,” Nuclear Engineering and design, 190(3), pp. 287-296.

[79] Šeruga, D., & Nagode, M. (2015). A method for long-term creep–rupture strength prediction based on a small sample of experimental results, smoothed bootstrapping and time-temperature parameters. Materials & Design, 67, 180-187.

[80] ECCC Recommendations. Creep data validation and assessment procedures. In: Holdsworth, S.R. et al., editors, vol. 5. ECCC Publication; 2001 [Data assessment].

[81] Bolton, J. (2013). A visual perspective of creep rupture extrapolation. Materials at High Temperatures, 30(2), 87-98.

[82] M. Prager, The Omega Method–An Engineering Approach to Life Assessment, ASME J. Press. Vessel Technol. 122 (2000) 273–280. doi:10.1115/1.556184.

[83] C.C. Manu, A.M. Birk, I.Y. Kim, Uniaxial high-temperature creep property predictions made by CDM and MPC omega techniques for ASME SA 455 steel, Eng. Fail. Anal. 16 (2009) 1303–1313. doi:10.1016/j.engfailanal.2008.08.005.

[84] T.L. Anderson, D.A. Osage, API 579: A comprehensive fitness-for-service guide, Int. J. Press. Vessel. Pip. 77 (2001) 953–963. doi:10.1016/S0308-0161(01)00018-7.

[85] M.S. Haque, C.M. Stewart, Comparison of a New Sin-Hyperbolic Creep Damage Constitutive Model with the Classic Kachanov-Rabotnov Model Using Theoretical and Numerical Analysis, in: TMS2015 Suppl. Proc., John Wiley & Sons, Inc., Orlando, FL, 2015: pp. 937–945. doi:10.1002/9781119093466.ch114.

[86] T. Izaki, T. Kobayashi, J. Kusumoto, A. Kanaya, A creep life assessment method for boiler pipes using small punch creep test, Int. J. Press. Vessel. Pip. 86 (2009) 637–642. doi:10.1016/j.ijpvp.2009.04.005.

[87] M. Evans, A comparative assessment of creep property predictions for a 1CrMoV rotor steel using the CRISPEN, CDM, Omega and Theta projection techniques, J. Mater. Sci. 39 (2004) 2053–2071. doi:10.1023/B:JMSC.0000017768.59276.3f.

[88] W.-G. Kim, S.-N. Yin, Y.-W. Kim, J.-H. Chang, Creep characterization of a Ni-based Hastelloy-X alloy by using theta projection method, Eng. Fract. Mech. 75 (2008) 4985–4995. doi: j.engfracmech.2008.06.017.

[89] Haque, M. S., An improved sin-hyperbolic constitutive model for creep deformation and damage, The University of Texas at El Paso, 2015. http://search.proquest.com/docview/1699053616?accountid=7121.

[90] A. Baldan, E. Tascioglu, Assessment of θ-projection concept and fracture cavitation, J. Mater. Sci. 43 (2008) 4592–4606. doi:10.1007/s10853-008-2666-2.

[91] S.Y. Lee, Y.L. Lu, P.K. Liaw, H. Choo, S.A. Thompson, J.W. Blust, P.F. Browning, A.K. Bhattacharya, J.M. Aurrecoechea, D.L. Klarstrom, High-temperature tensile-hold crack-growth behavior of HASTELLOY® X alloy compared to HAYNES® 188 and HAYNES® 230® alloys, Mech. Time-Dependent Mater. 12 (2008) 31–44. doi:10.1007/s11043-008-9049-6.

[92] R.W. Evans, J.D. Parker, B. Wilshire, The θ projection concept—A model-based approach to design and life extension of engineering plant, Int. J. Press. Vessel. Pip. 50 (1992) 147–160. doi: 10.1016/0308-0161(92)90035-E.

[93] P. McVetty, Creep of metals at elevated temperatures: The hyperbolic sine relation between stress and creep rate, ASME Trans. 65 (1943) 761–769.

[94] T.H. Hyde, W. Sun, A. Tang, Determination of material constants in creep continuum damage constitutive equations, Strain. 34 (1998) 83–90. doi:10.1111/j.1475-1305.1998.tb01089.x.

[95] Yao, H. T., Xuan, F. Z., Wang, Z., and Tu, S. T., 2007, "A review of creep analysis and design under multi-axial stress states," *Nuclear Engineering and Design*, 237(**18**), pp. 1969-1986.

[96] Hayhurst, D. R., 1972, "Creep Rupture Under Multi-Axial States of Stress," *Journal of the Mechanics and Physics of Solids*, 20(**6**), pp. 381-390.

[97] Giannopoulos, I. P., and Burgoyne, C. J., 2011, "Prediction of the Long-Term Behaviour of High Modulus Fibres using the Stepped Isostress Method (SSM)," *Journal of Material Science*, 46(24), pp. 7660-7671.

[98] Goodall, I. W., and Skelton, R. P., 2004, "The importance of multiaxial stress in creep deformation and rupture," *Fatigue & Fracture of Engineering Materials & Structures*, 27(4), pp. 267-272.

[99] Webster, G. A., Holdsworth, S. R., Loveday, M. S., Nikbin, K., Perrin, I. J., Purper, H., and Spindler, M. W., 2004, "A code of practice for conducting notched bar creep tests and for interpreting the data," *Fatigue & Fracture of Engineering Materials & Structures*, 27(**4**), pp. 319-342.

[100] Spindler, M. W., 2004, "The multiaxial creep ductility of austenitic stainless steels," Fatigue & Fracture of Engineering Materials & Structures, 27(**4**), pp. 273-281.

[101] Haque, M. S., Ramirez, C., and Stewart, C. M., 2017, "A Novel Metamodeling Approach for Time-Temperature Parameter Models," ASME 2017 Pressure Vessel and Piping Conference. American Society of Mechanical Engineers [PVP2017-65297].

[102] Haque, M. S., & Stewart, C. M. (2017, July). Selection of Representative Stress Function Under Multiaxial Stress State Condition for Creep. In ASME 2017 Pressure Vessels and Piping Conference (pp. V06AT06A065-V06AT06A065). American Society of Mechanical Engineers.

[103] Sdobyrev, V. P., 1958, Long-term strength of EI-437B alloy in the multi-axial stress state," *Izv. Akad. Nauk SSSR* 4, pp. 92-97.

[104] Lemaitre, J. and Chaboche, J. L., 1990, "Mechanics of Solid Materials," Cambridge University Press, Cambridge.

[105] Dyson, B. F. and McLean, D., 1977, "Creep of Nimonic 80A in torsion and tension," *Material Science*, 11, pp. 37–45.

[106] Cane, B. J., 1979, "Creep cavitation and rupture in 21/4 CrMo steel under uniaxial and multiaxial stresses," In: Proceedings of the International Conference on Mechanical Behaviour of Materials (Edited by K. J. Miller & R. F. Smith), 2, Pergamon Press, Oxford, pp. 173–182.

[107] ASME, 2015, ASME Boiler and Pressure Vessel Code, Section III, Division 1, Subsection NH – Class 1, Components in Elevated Temperature Service.

[108] Huddleston, R. L., 1985, "An improved multiaxial creep-rupture strength criterion. Trans. ASME," *J. Press. Vessel Technolgy,* 107, pp. 412–429.

[109] Rice, J. R., & Tracey, D. M., 1969, "On the ductile enlargement of voids in triaxial stress fields," *Journal of the Mechanics and Physics of Solids*, 17(3), pp. 201-217.

[110] Manjoine, M. J., 1975. "Ductility indices at elevated temperature," ASME *J. Engng. Mater. Technol.,* April, pp. 156–161.

[111] Manjoine, M. J., 1982, "Creep-rupture behavior of weldments," Weld. J. , February, 50s–57s, research supplement.

[112] Cocks, A.C.F. and Ashby, M. F., 1980, "Intergranular fracture during power-law creep under multiaxial stress," *Material Science*, 14, pp. 395–402.

[113] Ainsworth, R.A. Ed., 2003, "R5: An Assessment Procedure for the High Temperature Response of Structures," Issue 3, British Energy Generation Ltd., Barnwood.

[114] Hales, R., 1994, "The role of cavity growth mechanisms in determining creep rupture under multi-axial stresses," *Fatigue Fract. Eng. Mater. Struct*. 17, pp. 579-591.

[115] Kraus, Creep Analysis, John Wiley, New York, 1980.

[116] Hayhurst, D. R., Dyson, B. F., & Lin, J., 1994, "Breakdown of the skeletal stress technique for lifetime prediction of notched tension bars due to creep crack growth," *Engineering fracture mechanics*, 49(5), pp. 711-726.

[117] Othman, A. M., Hayhurst, D. R., & Dyson, B. F., 1993, "Skeletal point stresses in circumferentially notched tension bars undergoing tertiary creep modelled with physically based constitutive equations," In Proceedings of the Royal Society of London A: *Mathematical, Physical and Engineering Sciences*, Vol. 441, No. 1912, pp. 343-358.

[118] Hyde, T. H., Xia, L., & Becker, A. A., 1996, "Prediction of creep failure in aeroengine materials under multi-axial stress states," *International journal of mechanical sciences*, 38(4), 385-403.

[119] Spindler, M. W., Hales, R. and Skelton, R. P., 2001, The multiaxial creep ductility of an ex-service Type 316H stainless steel," In: Proceedings of the 9th Conference on *Creep & Fracture of Engineering Materials & Structures* (Edited by J. D. Parker); IOM London, UK, pp. 679–688.

[120] W. Ren, and C. Luttrell, Gen IV Materials Handbook Beta Release for Structural and Functional Evaluation. US Department of Energy, 2006, Report No. ORNL/GEN4/LTR-06–027.

[121] Materials Creep Database of NIMS – National Institutes for Materials Science, Japan. http://smds.nims.go.jp/creep/index_en.html

[122] D. A. Woodford, Test methods for accelerated development, design and life assessment of high-temperature materials, Materials and Design, 14(4), 1993, 231-242.

[123] R. L. Klueh, J. P. Shingledecker, R. W. Swindeman, and D. T. Hoelzer, Oxide dispersion-strengthened steels: A comparison of some commercial and experimental alloys, Journal of Nuclear Materials, 2005, 341(2), 103-114.

[124] H. E. McCoy, and R. D. Waddel, 1975, "Mechanical Properties of Several Products from a Single Heat Of Type 304 Stainless Steel," Journal of Engineering Materials and Technology, 97(4), pp 343-350.

[125] G. A. Webster, and R. A. Ainsworth, High temperature component life assessment, Springer Science and Business Media, 2013.

[126] Narasimhachary, S. B., and Saxena, A., 2013, "Crack growth behavior of 9Cr− 1Mo (P91) steel under creep-fatigue conditions," International Journal of Fatigue, 56, pp. 106-113.

[127] ASTM Standard A335/A335M-10b, 2015, Standard specification for seamless ferritic alloy–steel pipe for high-temperature service, ASTM International, West Conshohocken, PA, USA.

[128] Kim, W. G., Yin, S. N., Ryu, W. S., Chang, J. H., and Kim, S. J., 2008, "Tension And Creep Design Stresses Of The Hastelloy-X Alloy For High-Temperature Gas-Cooled Reactors," Materials Science and Engineering: A, 483, pp. 495- 497.

[129] R. Sandström, Extrapolation of creep strain data for pure copper, Journal of testing and evaluation, 27(1) (1999) 31-35. https://doi.org/10.1520/JTE12037J

[130] W. M. Cummings, and R. H. King, Extrapolation of Creep Strain and Rupture Properties of 1/2 per Cent Cr, 1/2 per Cent Mo, 1/4 per Cent V Pipe Steel, Proceedings of the Institution of Mechanical Engineers, 185(1), (1970) 285-299.
https://doi.org/10.1243/PIME_PROC_1970_185_036_02

[131] M. K. Booker, C. R. Brinkman, and V. K. Sikka, Correlation and extrapolation of creep ductility data for four elevated temperature structural materials (No. ORNL-TM--4992) (1975) Oak Ridge National Lab., Tenn.(USA).

[132] Method of Extrapolation Used in the Analysis of Creep Rupture Data, Parts 1 to 6: Derivation of Long Term Stress-Rupture Properties, Annex to International Standard ISO 6303, 1981.

[133] R. Sandström, R. A procedure for extended extrapolation of creep rupture data, Journal of testing and evaluation, 31(1) (2003) 58-64.

[134] R. Sandström, and L. Lindé, Precision in the extrapolation of creep rupture data. Journal of testing and evaluation, 27(3) (1999) 203-210. https://doi.org/10.1520/JTE12063J

[135] S. Holdsworth, The European Creep Collaborative Committee (ECCC) approach to creep data assessment, Journal of Pressure Vessel Technology, 130(2) (2008) 024001.

[136] D. R. Hayhurst, D. A. Lavender, N. G. Worley, A. Salim, An assessment of the θ-projection method for the representation and extrapolation of creep data for a 1% Cr, 12% Mo, 14% V steel tested at 565° C, International journal of pressure vessels and piping, 20(4), (1985) 289-317.

[137] K. Maruyama, and H. Oikawa, An extrapolation procedure of creep data for St Determination: with special reference to Cr-Mo-V steel, Journal of pressure vessel technology, 109(1) (1987) 142-146.

[138] S. R. Brown, R. W. Evans, and B. Wilshire, A comparison of extrapolation techniques for long-term creep strain and creep life prediction based on equations designed to represent creep curve shape. International Journal of Pressure Vessels and Piping, 24(3), (1986), 251-268.

[139] Z. Abdallah, K. Perkins, and S. Williams, Advances in the Wilshire extrapolation technique—Full creep curve representation for the aerospace alloy Titanium 834, Materials Science and Engineering: A, 550, (2012), 176-182.

[140] J. Lemaitre, J. How to use damage mechanics. Nuclear engineering and design, 1984, 80(2), 233-245.

[141] J. L. Chaboche, Continuum damage mechanics: Part II—Damage growth, crack initiation, and crack growth. Journal of applied mechanics, 1988, 55(1), 65-72.

[142] S. MURAKAMI, S., Progress of continuum damage mechanics. JSME international journal, 1987, 30(263), 701-710.

[143] H. T. Yao, F. Z. Xuan, Z. Wang, and S. T. Tu, A review of creep analysis and design under multi-axial stress states. Nuclear Engineering and Design, 2007, 237(18), 1969-1986.

[144] D. R. Hayhurst, The use of continuum damage mechanics in creep analysis for design. The Journal of Strain Analysis for Engineering Design, 1994, 29(3), 233-241.

[145] C. M. Stewart, A. P. Gordon, Y. W. Ma, Y. W., R. W. Neu, An anisotropic tertiary creep damage constitutive model for anisotropic materials. International Journal of Pressure Vessels and Piping, 2011, 88(8), 356-364.

[146] S. Murakami, and Y. Liu, Mesh-dependence in local approach to creep fracture, International Journal of Damage Mechanics, 4.3 (1995): 230-250.
http://journals.sagepub.com/doi/abs/10.1177/105678959500400303

[147] C. M. Stewart, and A. P. Gordon, 2012, Constitutive Modeling of Multistage Creep Damage in Isotropic and Transversely Isotropic Alloys with Elastic Damage. Journal of Pressure Vessel Technology, 134(4), 041401.

[148] T. H. Hyde, W. Sun, and J. A. Williams, Creep analysis of pressurized circumferential pipe weldments—a review. The Journal of Strain Analysis for Engineering Design, 2003, 38(1), 1-27.

[149] K. Fujiyama, Risk based engineering for design, material selection and maintenance of power plants. Materials at High Temperatures, 2011, 28(3), 225-233.

[150] C. M. Stewart, and A. P. Gordon, Modeling the Temperature Dependence of Tertiary Creep Damage of a Ni-Based Alloy. Journal of Pressure Vessel Technology, 131(5), (2009), 051406.

[151] P. G. McVetty, Creep of Metals at Elevated Temperatures – Hyperbolic-Sine Relation Between Stress and Creep Rate, Transactions of the ASME, 65(7) (1943) 761-767.

[152] S. Murakami, Y. Liu, M. Mizuno, Computational methods for creep fracture analysis by damage mechanics, Comput. Methods Applied Mechanics Engineering, 183 (2000), 15-33. http://doi.org/10.1016/S0045-7825(99)00209-1

[153] Booker, M. K., 1978, "Use of Generalized Regression Models for the Analysis of Stress Rupture Data," United States Department of Energy by Union Carbide Corporation, Contract W7405-eng-26, CONF-780609-5, Oak Ridge, Tn.

[154] Gold, M., Leyda, W. E., and Zeisloft, R. H., 1975, "The Effect of Varying Degrees of Cold Work on the Stress-Rupture Properties of Type 304 Stainless Steel," Journal of Engineering Materials and Technology, 97(4), pp. 305-312.

[155] Sritharan, T., and Jones, H., 1980, "The Creep of Type 304 Stainless Steel at Low Stresses", Acta Metallurgica, 28(12), pp. 1633-1639.

[156] Kim, H.K., Mohamed, F. A., Earthman, J. C., 1991, "High-Temperature Rupture of Microstructurally Unstable 304 Stainless Steel Under Uniaxial and Triaxial Stress States," Metallurgical Transactions A, 22A, pp.2629-2636.

[157] Wilson, D. J., 1971, "Extrapolation of Rupture Data for Type 304 (18Cr-10Ni), Grade 22 (2-1/4Cr-1Mo) and Grade 11(1-1/4Cr-1/2Mo-3/4Si) Steels," Progress Report to: The Metal Properties Council, Report 34006-2P, New York, NY.

[158] Bynum, J. E., Ellis, F. V., Roberts, B. W., and Canonico, D. A., 1992, "High Temperature Creep of Type 304 Stainless Steel," Stress Classification, Robust Methods, and Elevated Temperature Design; presented at the 1992 Pressure Vessels and Piping Conference, New Orleans, La, pp. 67-83.

[159] E. Hosseini, S. R. Holdsworth, and E. Mazza, Stress regime-dependent creep constitutive model considerations in finite element continuum damage mechanics, International Journal of Damage Mechanics, 22.8 (2013): 1186-1205. doi: 10.1177/1056789513479810

[160] F. C. Monkman, and N. J. Grant, Proceedings of ASTM, 1956, vol. 56, pp. 593-620.

[161] R. W. Evans, J. D. Parker, and B. Wilshire, 1992 "The θ projection concept—A model-based approach to design and life extension of engineering plant," International Journal of Pressure vessels and piping, 50(1-3), 147-160.

[162] L. Yang, and A. Fatemi, 1998 "Cumulative fatigue damage mechanisms and quantifying parameters: a literature review. Journal of testing and evaluation, " 26(2), 89-100.

[163] Haque, M. S., Arrieta, E., Mireles, J., Carrasco, C., Stewart, C. M., & Wicker, R. B. (2016, November). Mechanical Behavior and Microstructure of Electron Beam Melted Ti-6Al-4V Using Digital Image Correlation. In ASME 2016 International Mechanical Engineering Congress and Exposition (pp. V009T12A059-V009T12A059). American Society of Mechanical Engineers.

[164] Arrieta, E., Haque, M. S., Mireles, J., Stewart, C. M., Carrasco, C. and Wicker, R. B., 2018, Mechanical Behavior of Differnetly Oriented EBM Ti-6AL-4V Components Using Digital Image Correlation, ASME Journal of Engineering Materials and Technology.

Appendix

A1: Development of Creep Design Maps

Sine-Hyperbolic model:

```
clear variables
close all
clc
tmax=850; tmin=550;
temp=linspace(tmin,tmax,(tmax-tmin+1));
temp1=temp.';
smin=0; smax=400;
stress=linspace(smin,smax,(smax-smin+1));
stress1=stress.';
xcord=zeros((tmax-tmin+1)*(smax-smin+1),1);
ycord=zeros((tmax-tmin+1)*(smax-smin+1),1);

%% Making the X and Y co-ordinate values
c2=1;
for n4=1:(tmax-tmin+1)
   c1=temp1(n4,1);
   for n5=1:(smax-smin+1)
      xcord(c2,1)=c1;
      ycord(c2,1)=n5;
      c2=c2+1;
   end
end
```

```
%% Finding all the constants for Sinh
B=zeros((tmax-tmin+1),1);    Ss=zeros((tmax-tmin+1),1);
M=zeros((tmax-tmin+1),1); St=zeros((tmax-tmin+1),1); Chi=zeros((tmax-tmin+1),1);
lambda=zeros((tmax-tmin+1)*(smax-smin+1),1);
emin=zeros((tmax-tmin+1)*(smax-smin+1),1);
tr=zeros((tmax-tmin+1)*(smax-smin+1),1);
c=1;

%Finding standard deviation
STD=5869.44; fctr=3;
TRmax=zeros((tmax-tmin+1)*(smax-smin+1),1);
TRmin=zeros((tmax-tmin+1)*(smax-smin+1),1);

for n=1:(tmax-tmin+1)
   B=10.^(-5000000000000*temp1.^(-4.231));
   Ss=3.84.*exp(0.0019*temp1);
   M=10.^((1)*(4.02*log(temp1)-30.375));
   St=4295*exp(-0.00609*temp1);
   Chi=39293*temp1.^-1.4;
    for n1=1:(smax-smin+1)
      emin(c,:)=B(n,1)*sinh(stress1(n1,:)/Ss(n,1));
      tr(c,:)=1/(M(n,1)*(sinh(stress1(n1,:)/St(n,1))^Chi(n,1)));
      TRmax(c,:)=(1/(M(n,1)*(sinh(stress1(n1,:)/St(n,1))^Chi(n,1))))*5;
      TRmin(c,:)=(1/(M(n,1)*(sinh(stress1(n1,:)/St(n,1))^Chi(n,1))))*.17;
      lambda(c,:)=4.5;
      %lambda(c,:)=0.0044*tr(c,:)+2.9;
```

```
      c=c+1;
    end
end
%% Sinh modeling
x=1000;
time=linspace(1,x,x)'; dmg=zeros(x,1);
damage=zeros((tmax-tmin+1)*(smax-smin+1),1); %strt=zeros(x,1);
strain=zeros((tmax-tmin+1)*(smax-smin+1),1);

strnTime=zeros(x,1);
for n2=1:(tmax-tmin+1)*(smax-smin+1)
   trs=tr(n2,1);
   emn=emin(n2,1); lambda1=lambda(n2,1); strt=zeros(x,1);

   for n3=1:x
      if x>time(n3,1); % it was trs>x;
%dmg(n3,1)=-1*(1/4)*log(1-(1-exp(-4))*(time(n3,1)/trs)); % original

dmg(n3,1)=-1*(1/3)*log(1-(1-exp(-3))*(time(n3,1)/x));  % if the rupture is greater than the tr
strt(n3,1)=emn*exp(lambda1*dmg(n3,1).^1.5);
strnTime(n3,1)=sum(strt);
      else dmg(n3,1)=1;
         strt(n3,1)=emn*exp(lambda1*dmg(n3,1).^1.5); % this is for
         strnTime(n3,1)=sum(strt);
       end
   end
    damage(n2,1)=dmg(x,1);
```

```
    strain(n2,1)=sum(strt);
end
 disp(' :) Calculation complete :)')

%% Similarly the creep design maps for the Kachanov-Rabotnov model was developed
```

A2: MULTIAXIAL REPRESENTATIVE FUNCTIONS

Multiaxial representative functions

Investigator	Material	Loading Condition (°C)	Weight factor
$\sigma_{rep} = \sigma_1 + 3\beta\sigma_m + (1-\alpha-\beta)\sigma_{VM}$			
Chellapandi, 2006	Steam Generator Tube, 9Cr-1Mo	659.85	$\alpha = 0.000, \beta = 0.133$
Hayhurst, 1984	Aluminum alloy	210	$\alpha = 0.000, \beta = 0.000$
	Copper	250	$\alpha = 0.700, \beta = 0.000$
	AISI 316 SS	550	$\alpha = 0.750, \beta = 0.000$
Hyde, 1996	Nickel Based alloy	700	$\alpha = 0.150, \beta = 0.000$
	Titanium alloy	650	$\alpha = 0.000, \beta = 0.000$
Hyde, 2005	P91 weldmet (A-69-FP91)	625	$\alpha = 0.500, \beta = 0.000$
Hyde, 2014	P91	650	$\alpha = 0.313, \beta = 0.000$
	316 SS	600	$\alpha = 0.487, \beta = 0.000$
Becker, 2002	Titanium alloy	650	$\alpha = 0.000, \beta = 0.000$
	0.5Cr0.5Mo0.25V (Service aged)	640	$\alpha = 0.300, \beta = 0.000$
	0.5Cr0.5Mo0.25V (Parent Metal)	640	$\alpha = 0.300, \beta = 0.000$
	0.5Cr0.5Mo0.25V (Heat Affected Zone)	640	$\alpha = 0.490, \beta = 0.000$
	0.5Cr0.5Mo0.25V (weld metal)	640	$\alpha = 0.260, \beta = 0.000$
Haque and Stewart, 2015	Waspaloy (Bridgeman Notched Specimen)	700	$\alpha = 0.248, \beta = 0.000$

$\sigma_{rep} = (\sigma_1 / \sigma_{VM})^{\gamma/\nu} \sigma_{VM}$			
Al Abed, 1999	2.25Cr1Mo	600	$\gamma = 0$
	Ferritic bolting steel (1CrMoVTiB)	550	$0 < \gamma < \nu$
	2.25Cr1Mo (Simulated HAZ material)	600	$\gamma \sim \nu$
$\varepsilon_{f_n} / \varepsilon_{f_u} = \exp\left[\mathrm{p}\left(1 - \frac{\sigma_1}{\sigma_{VM}} \right) + q\left(0.5 - \frac{3\sigma_m}{2\sigma_{VM}} \right) \right]$			
Spindler, 1994	304 SS	593	$p = 2.380, q = 1.040$
	316 SS	600	$p = 0.150, q = 1.250$
$\varepsilon_{f_n} / \varepsilon_{f_u} = \sinh\left[\frac{2(n-0.5)}{3(n+0.5)} \right] / \sinh\left[\frac{2(n-0.5)}{(n+0.5)} \cdot \left(\frac{\sigma_m}{\sigma_{VM}} \right) \right]$			
Ha, 2004	12CrWCoB	650	$n = 17.5$

Vita

My name is Mohammad Shafinul Haque. I have earned my Bachelor's degree in mechanical engineering (BSc in ME, 4-year degree) from Khulna University of Engineering and Technology (KUET), Khulna, Bangladesh. I have earned my Master's degree in Mechanical Engineering from the University of Texas El Paso, Texas. I have completed my degree requirement for Doctor of philosophy (PhD) degree in mechanical engineering here at University of Texas El Paso (UTEP). This dissertation is submitted as a requirement of the degree including my research works throughout my graduate level study under the supervision of Dr. Calvin M Stewart.

I have been working on national energy and research development program funded by Department of Energy (DOE). My research specialization is in mechanics of materials that include but not limited to constitutive modeling, numerical analysis, finite element method, failure analysis etc. As a direct result of his research, I have appeared in eight peer-reviewed conference proceedings, published/submitted four journal papers, performed nine technical presentations and posters. Throughout my tenure at UTEP, I have acted as a research mentor for four undergraduate students at the UTEP MERG research group.

Mr. Haque has an excellent academic standing (GPA 4.0) in his graduate-level study. His academic excellence is recognized by the awards such as Dodson Research Grant 2015, UTEP Graduate School Travel Grant 2015, Frank B. Cotton Scholarship 2016, ASME Honorable Mention Paper award, 2017 to name a few.

Contact Information:

Mohammad Shafinul Haque, email: mhaque@miners.utep.edu, cell: (915) 731-3449